Acid water – rock – cement interaction and multicomponent reactive transport modeling

Jordi Cama

Department of Geosciences, Institute of Environmental Assessment and Water Research (IDAEA-CSIC), Barcelona 08034, Catalonia, Spain

jordi.cama@idaea.csic.es

Josep M. Soler

Department of Geosciences, Institute of Environmental Assessment and Water Research (IDAEA-CSIC), Barcelona 08034, Catalonia, Spain

josep.soler@idaea.csic.es

Carles Ayora

Department of Geosciences, Institute of Environmental Assessment and Water Research (IDAEA-CSIC), Barcelona 08034, Catalonia, Spain

caigeo@idaea.csic.es

INTRODUCTION

This chapter addresses the use of multicomponent reactive transport modeling (MCRTM) in an attempt to understand and quantify the interaction between acid water and rocks or Portland cement (mortar, concrete) during and after the injection of CO_2 in deep aquifers (geological CO_2 storage) and in the treatment of acid mine drainage (AMD). Anthropogenic acidification of water occurs in the two cases (Gunter et al., 1993; Nordstrom and Alpers, 1999).

In the first case, CO_2-rich water is acidic and out of equilibrium with the reservoir and seal rocks of a geological CO_2 storage system, leading to mineral reactions (e.g. calcite dissolution and gypsum precipitation) and potential changes in porosity and permeability. These adverse effects could even be more profound in the contact between acid waters and Portland cement, because of the high pH conditions in cement (pH > 12). Water acidity is due to the CO_2 enrichment of the formation waters, i.e. production of H_2CO_3

$$CO_2(gas) \rightleftharpoons CO_2(aq) \quad (1)$$

$$CO_2(aq) + H_2O \rightleftharpoons H_2CO_3(aq) \quad (2)$$

$$H_2CO_3(aq) \rightleftharpoons H^+ + HCO_3^- \quad (3)$$

$$HCO_3^- \rightleftharpoons H^+ + CO_3^{2-} \quad (4)$$

In the second case, acid mine drainage (AMD) is a result of proton release during the oxidative dissolution of pyrite (FeS_2) and the precipitation of other Fe-bearing sulfides, sulfosalts and oxyhydroxides. The dissolution of pyrite by oxygen can be expressed as

$$FeS_2 + 3.5O_2(aq) + H_2O \rightleftharpoons Fe^{2+} + 2SO_4^{2-} + 2H^+ \quad (5)$$

SO_4^{2-}, Fe(II) and protons are released to solution, and Fe(II) is oxidized to Fe(III)

$$Fe^{2+} + 0.25\ O_{2(aq)} + H^+ \rightleftharpoons Fe^{3+} + 0.5\ H_2O \quad (6)$$

Fe(III) may precipitate as schwertmannite (Bigham et al., 1996)

$$8Fe^{3+} + SO_4^{2-} + 14H_2O \rightleftharpoons Fe_8O_8(OH)_6(SO_4) + 22H^+ \quad (7)$$

releasing more protons, or as a Fe(III)-hydroxide (ferrihydrite), also releasing protons

$$Fe^{3+} + 3\ H_2O \rightleftharpoons Fe(OH)_3 + 3\ H^+ \quad (8)$$

But at pH lower than 3, Fe(III) remains mainly in solution and acts as another oxidizing agent for pyrite according to

$$FeS_2 + 14\ Fe^{3+} + 8\ H_2O \rightleftharpoons 15\ Fe^{2+} + SO_4^{2-} + 16\ H^+ \quad (9)$$

In CO_2-rich waters, acidic conditions can be maintained during long periods owing to the buffering effect of a weak acid (H_2CO_3) during the mineral reactions, whereas acidity in a strong acid (H_2SO_4 in AMD) is rapidly neutralized when protons are consumed by reaction with the solid phases.

Geological storage of CO_2

In the last decade, laboratory flow-through experiments under the conditions of the injection sites have been performed to study the interaction of the CO_2-rich waters with reservoir and seal rocks (Noiriel et al., 2007; Luquot and Gouze, 2009; Luquot and Noiriel et al., 2013, 2015; Luquot et al., 2014; Noiriel, 2015; Smith et al., 2013a, 2017; Beckingham et al., 2016; Menke et al., 2016; Rohmer et al., 2016; Loring et al., 2019 and references therein). These authors highlight the effect of mineral dissolution and precipitation reactions on porous/fractured media, flow, permeability and porosity. In several studies, the geochemical variation in the experimental runs has been interpreted using multicomponent reactive transport modeling (MCRTM) (Carroll et al., 2011, 2013; Canal et al., 2012; Hao et al., 2013; Luhmann et al., 2014, 2017; Tutolo et al., 2015a; Luquot et al., 2016; Beckingham et al., 2017; Smith et al., 2017; Dai et al., 2019). The resulting discussions on the effectiveness of the derived kinetic parameters (dissolution rate constant, mineral reactive surface area) and porosity-permeability relationships and their application to the reservoir scale reinforce the need to use MCRTM.

Our research on water-rock -interaction in geological carbon sequestration has yielded some experimental and MCRTM results concerning the demonstration test site for CO_2 storage at Hontomín (SW Spain) (García-Rios et al., 2014, 2015, 2017; Dávila et al., 2016a, 2016b, 2017; Thaysen et al., 2017). At this site, reservoir and seal formations are mainly constituted by sedimentary rocks (limestone, sandstone and argillaceous limestones (referred to as marls)) with a high content of calcite (67-90 wt%) and some dolomite (≈ 10 wt%). We addressed the quantitative interpretation of the effect of mineral dissolution and precipitation reactions on rock porosity and fracture permeability. Given that reservoir and cap (seal) rock permeability ($k = 10^{-19}$ - 10^{-18} m^2; Alcalde et al., 2013; Mbia et al., 2014) can be several orders of magnitude smaller than fracture permeability, fluids will flow preferentially through fractures or microcracks, where chemical alteration induced by the CO_2-rich fluids can bring about changes in physical and chemical properties. Since carbonate rocks are common in reservoir and seal formations of potential CO_2-storage sites worldwide (e.g. Midale carbonate unit in Weyburn, Emberley et al., 2004: Kharaka et al., 2013; sedimentary basins, Benson and Cole, 2008; Dover 33 reef in the Michigan Basin, Welch et al., 2019), research can help us to better understand the basic reaction mechanisms. Portland cement is placed between the borehole steel casing and the surrounding rock at CO_2 injection sites to prevent gas or fluid leakage. During and after CO_2 injection, the resulting CO_2-rich acid water may deteriorate the cement and favor undesired leaking (Walsh et al. 2014; Iyer et al., 2017). Quantification of geochemical processes at the laboratory scale through MCRTM is therefore necessary to understand their occurrence under the reservoir/seal and wellbore conditions.

Acid mine drainage treatment

Our research aimed at improving passive treatments to remediate the AMD-contaminated streams and rivers in the Iberian Pyrite Belt (IPB) in south-western Spain. MCRTM has been used for more than 20 years to investigate sulfide oxidation rates and the subsequent metal release from mine wastes causing pollution in aquifers downstream (Wunderly et al., 1996; Mayer et al., 2002; Salmon and Malstrom, 2004; Brookfield et al., 2006; Malstrom et al., 2008; Pedretti et al., 2017). These models coupled unsaturated flow and chemical reactions involving a number of poorly constrained parameters. As a result, MCRTM has led to qualitative predictions of water compositions and of the relative importance of the multiple processes involved (Xu et al., 2000; Mayer et al., 2002; Acero et al., 2007, 2009). More common is the use of MCRTM in simulating the behavior of remediation actions, such as passive treatment systems, permeable reactive barriers and covers to inhibit sulfide oxidation (Amos et al., 2004; Mayer et al., 2006; Perez-Lopez et al., 2007, 2009; Pabst et al., 2017, 2018). One of the most common passive treatment systems is the anoxic limestone drain (ALD), or systems derived from it (e.g. disperse alkaline substrate (DAS) tanks). These systems are characterized by a mixture of a fine-grained alkaline source such as limestone and an inert matrix with high porosity such as wood shavings (Rötting et al., 2008b). The efficiency of these treatments and the quality of the outflowing water clearly depend on the competition between the rates of water flow and chemical reactions. Therefore, accurate parameterization of the models is crucial to the design of an efficient remediation system.

Of the different parameters describing MCRTM, the mineral reactive surface area is the most difficult to determine. A number of reasons such as the heterogeneous flow paths, rugosity of the solid surfaces, precipitation of neo-formed minerals and the formation of diffusion boundary layers have been proposed to account for the difficulty of upscaling laboratory to field reaction rates (White and Brantley, 2003; Steefel et al., 2015a). A considerable effort has recently been devoted to understanding the reactive surface area from the microscale point of view (Noiriel et al., 2009; Gouze and Louquot, 2011; Li et al., 2015; Beckingham et al., 2016, 2017). Below we describe a practical methodology to obtain the parameters for reactive transport modeling, especially the experimental determination of the reactive surface area, and its application to the design of a field scale remediation system (Ayora et al., 2013).

Outline

We show how MCRTM is used to simulate the interaction between the acid water and the solid phases controlling the variations in the aqueous chemistry and mineralogical changes in different sets of our laboratory experiments related to geological storage of CO_2 and AMD treatment systems. We discuss the reactivities of the different minerals and the model fitting procedure together with the corresponding adjusted parameters (bulk surface areas, diffusion coefficients in stagnant domains).

In the first section, we present the main characteristics of the laboratory experimental setups and the AMD- treatment plant employed in our studies. The second section presents a brief description of the equations and parameters in the reactive transport codes used (CrunchFlow, Steefel et al. (2015a) and RETRASO, Saaltink et al. (2004)). The following section addresses the quantitative interpretation of the experimental results from rock-fragment-filled columns and fractured-core -percolation experiments subjected to injection of CO_2-rich waters. The fourth section deals with the MCRTM that is used to reproduce the results in AMD-Portland cement columns and cores, and in AMD-DAS columns in order to improve field-scale AMD treatment plants. Finally, conclusions and future perspectives concerning the use of MCRTM for the

implementation of CO_2 geological storage and AMD passive treatment are given.

LABORATORY EXPERIMENTS AND FULL SCALE SYSTEM

Laboratory-scale experiments

Several sets of column and percolation experiments were conducted to study the anthropogenic acid water–rock/cement interaction at atmospheric P_{CO2} or at elevated P_{CO2} pressures (AMD systems or CO_2 storage, respectively).

Experimental setup. In the different set-ups an injected solution with a desired chemical composition interacted with the solid sample contained in a column (Fig. 1). This approach allowed us to monitor the variation of the aqueous chemistry caused by the ongoing geochemical reactions. The input solution was continuously injected from bottom to top of the samples at a constant flow rate by a peristaltic pump in experiments under atmospheric P_{CO2} conditions and by a dual-piston pump under elevated P_{CO2} conditions (Fig. 1a). In the experiments performed under atmospheric pressure, P_{Total} was 1 bar and pCO_2 was $10^{-3.5}$ bar; under elevated total pressures (P_{Total} = 10 or 150 bar), P_{CO2} was equal to P_{Total} when P_{Total} was 10 bar (subcritical P_{CO2} conditions) and P_{CO2} ranged between 34 and 130 bar when P_{Total} was 150 bar (supercritical P_{CO2} conditions).

In a first set of experiments, columns were filled with micrometer- or millimeter-size fragments of the same rock or with alternating layers of rock and Portland cement (Fig. 1b). The approximate porosities (volume of voids between grains) ranged from 45% to 65%. In a second set of experiments, solid samples consisted of cylindrical cores of 9 mm in diameter and 18 mm in length containing an artificially created fracture (Fig. 1c). In a third set of experiments, artificially fractured cores of 2.5 cm in diameter and 5 cm in length were composed of half a Portland cement cylinder and half a rock cylinder (Fig. 1c). Experiments that belong to the second and third sets are referred to as percolation experiments. Another type of columns with larger dimensions and with sampling points at different depths was built to measure the hydraulic conductivity of a porous substrate (dispersed alkaline substrate, DAS) by means of constant head tests (Fig. 1d). The head loss can be accurately measured by connecting piezometric standpipes along the column.

Solid samples and aqueous solutions. The reservoir rocks used in our experiments are mainly composed of calcite and dolomite (limestone), and calcite, quartz and microcline (clast-poor sandstone) with a 2-7% matrix porosity. The minerals of the cap rocks (marly limestone, black shale and marl) are calcite, quartz, illite, albite, clinochlore, gypsum, anhydrite and pyrite with a matrix porosity of ca. 7% (Table 1). The mineralogical composition of the hydrated Portland cement (sulfate resistant, CEM I 42.5R/SR) is summarized in Table 1, in which C-S-H (calcium silicate hydrate) and portlandite are the main phases.

For the CO_2 experiments, CO_2-rich solutions were prepared to be compositionally similar to the native saline solution from the Hontomín site (García-Rios et al., 2014; Dávila et al., 2017). Once the solutions were equilibrated with the corresponding P_{CO2} the input pH was ≈ 3.5 (Table 2). Moreover, to investigate the effect of SO_2 impurities in the CO_2 injection stream on the interaction between CO_2-rich solutions and carbonate rocks, sulfuric acid was added in amounts corresponding to 0.4% SO_2 in the flue gas (Thaysen et al., 2017), anticipating full oxidation of SO_2 to H_2SO_4 (Table 2), with a resulting input pH of ≈ 2. For the AMD columns with only rock, solutions were prepared at pH ≈ 2-3 (H_2SO_4) with Fe(II) and Al (Table 2). For the ones with alternating layers of rock and cement fragments, solutions were prepared at pH ≈ 2 (H_2SO_4) containing Al, Ca, Mg and Fe as major ions and Cd, As, Cu, Zn and Ni as minor components (Table 2). The DAS columns were fed with natural AMD (pH of 2.3 to 3.5) and inflow net

acidity of 1350 to 2300 mg L^{-1} as $CaCO_3$.

Full scale system

In situ passive remediation technologies are suitable for remediating the drainages of abandoned mines (Fig. 1e). A pilot plant of DAS-calcite technology was operated at Mina Monte Romero (Macías et al., 2012), and a full scale AMD treatment was constructed at Mina Esperanza (Caraballo et al., 2011; Fig. 2). The reactive tank (120 m^2 of surface and 4-m deep) was filled with a 2.5-m layer of limestone-DAS (50% porosity). Water flow through the reactive material was gravity fed from top to bottom (Fig. 1e), emerging finally from the top of a water collecting well.

MULTICOMPONENT REACTIVE TRANSPORT MODELING (MCRTM)

MCRTM at the continuum scale is at an advanced position in terms of its treatment of chemical processes (Steefel et al., 2005). Continuum formulations for reactive transport models and numerical simulations of reactive processes in porous media incorporate rate expressions, which once formulated with reliable kinetic parameters, are capable of accurately describing the mineral dissolution and precipitation reactions (Black et al., 2015; Marty et al., 2015; Molins, 2015; Beckingham et al., 2017).

Brief description of MCRTM

The observed mineralogical alterations and changes in solution compositions in the experiments presented in this chapter were modeled using the CrunchFlow or RETRASO reactive transport codes. These codes solve numerically the mass balance of solutes expressed as

$$\frac{\partial(\phi C_i)}{\partial t} = \nabla \cdot (\mathbf{D} \nabla C_i) - \nabla (\mathbf{q} C_i) + R_i \quad (i = 1, 2, 3, \ldots, n) \tag{10}$$

where ϕ is porosity, C_i is the concentration of component i (mol m^{-3}), $\mathbf{q}$ is the Darcy velocity ($m^3 m^{-2} s^{-1}$), R_i is the total reaction rate affecting component i (mol m^{-3} rock s^{-1}) and $\mathbf{D}$ is the combined dispersion-diffusion coefficient ($m^2 s^{-1}$). The total reaction rate R_i is given by

$$R_i = -\sum_m \nu_{im} R_m \tag{11}$$

where R_m is the rate of precipitation ($R_m>0$) or dissolution ($R_m<0$) of mineral m in mol m^{-3} rock s^{-1}, and ν_{im} is the number of the moles of i in mineral m.

The reaction rate laws used in the calculations are expressed as

$$R_m = A_m \sum_{terms} k_{m,T} a_{H+}^{n_{H+}} f(\Delta G_r) \tag{12}$$

where A_m is the mineral surface area in m^2 m^{-3} rock, $k_{m,T}$ is the reaction rate constant at the temperature of interest in mol m^{-2} s^{-1}, $a_{H+}^{n_{H+}}$ is the term describing the effect of pH on the rate, ΔG_r is the Gibbs energy of the reaction, and $f(\Delta G_r)$ is the functional dependence of the dissolution rate on the deviation from equilibrium

$$f(\Delta G_r) = \left(\left(\frac{IAP}{K_{eq}} \right)^{m_2} - 1 \right)^{m_1} \tag{13}$$

where IAP is the ionic activity product of the solution with respect to the mineral, K_{eq} is the equilibrium constant for the dissolution reaction (ionic activity product at equilibrium) and m_1 and m_2 allow for nonlinear dependencies on the affinity term. The rate constant at temperature T ($k_{m,T}$) is calculated from

$$k_{m,T} = k_{m,25} \exp\left(\frac{Ea}{R}\left(\frac{1}{T_{25}} - \frac{1}{T}\right)\right) \tag{14}$$

where $k_{m,25}$ is the rate constant at 25 ^{o}C, E_a is the apparent activation energy of the overall reaction (J mol^{-1}) and R is the gas constant (J mol^{-1} K^{-1}). Change in mineral surface area (A_m in $m^2_{mineral}$ $m^{-3}_{bulk\ rock}$) due to dissolution is given by

$$A_m = A^{initial}\left(\frac{\phi_m}{\phi_{m(i)}}\right)^{\frac{2}{3}}\left(\frac{\phi}{\phi_{(i)}}\right)^{\frac{2}{3}} \tag{15}$$

Change due to precipitation is given by

$$A_m = A^{initial}\left(\frac{\phi}{\phi_{(i)}}\right)^{\frac{2}{3}} \tag{16}$$

where $\phi_{m(i)}$ is the initial volume fraction of the mineral *m* and $\phi_{(i)}$ is the initial porosity of the medium. The term $(\phi/\phi_{(i)})^{2/3}$ results from the expression of the dependence of mineral surface area (m^2 m^{-3}_{rock}) on volume fraction for any given grain geometry (e.g. spheres or cubes). This formulation ensures that as the volume fraction of a mineral goes to 0, so does its surface area. Moreover, for both dissolving and precipitating minerals, the term $(\phi/\phi_{(i)})^{2/3}$ demands that the surface area of a mineral in contact with fluid goes to 0 when the porosity of the medium reaches 0. This formulation is employed for primary minerals (*i.e.*, minerals with initial volume fractions > 0). For secondary minerals which precipitate, the value of the initial bulk surface area specified is used as long as precipitation occurs. If this phase later dissolves, the above formulation is employed but with an arbitrary initial volume fraction of 0.01.

If specific surface areas are used instead of bulk surface areas, the evolution of the mineral volume fraction causes the bulk surface area (A_m) to evolve with time according to the following equation

$$A_m = \frac{\phi_m A_{specific}\ MW_m}{V_m} \tag{17}$$

where MW_m refers to the molecular weight of the phase, V_m is the molar volume of the solid phase and $A_{specific}$ is the specific surface area.

Numerical discretization

1-D simulations were performed in column experiments only filled with rock fragments because the small porosity of the rock matrix (≈ 2%) would not contribute to the whole rock reactivity. The very small porosity translates into negligible diffusion fluxes into or out of the rock fragments compared with the reactivity of the outer surfaces. Conversely, in the column

experiments where hydrated Portland cement was present, 2-D models were used to determine the effect of fluid diffusion through cement and its contribution to system reactivity. 2D models were also used for the experiments involving fractured cores.

One-dimensional numerical domains. In the rock-fragment columns, the size of the numerical elements may be the same along the whole 1D domain, but in some cases a finer resolution is needed close to the inlet (Fig. 3a), where the reactivity is highest. The solution is injected in element 1 and collected from the last element.

Two-dimensional numerical domains. To simulate the column experiments with both cement and rock fragments, a number of considerations had to be taken into account. The system was divided into two parts (Trapote et al., 2016): an immobile zone (cement or rock fragments where solute transport takes place only by diffusion) and a mobile zone (pore space between the grains where water circulates; Fig. 3b). The numerical domain (2D model with symmetry around the axis of the cylinder) was designed with two concentric cylindrical zones: an internal zone with mortar or rock (only diffusion), and an external zone filled only with circulating water (Fig. 3b). The radius of the internal zone was equal to the radii of the rock/cement fragments. The thickness of the mobile zone was calculated according to the open pore volume between grains in the experiment. And a model column length was calculated to conserve the same total volume (fragments + water) as in the experiment. A model flow velocity (advection along the external mobile zone) was finally calculated according to the experimental mean residence time of the circulating water in the experiment.

In fractured cores with exclusively rock, only half of the core was considered given the symmetry in the experimental setup (Fig. 3c). In addition, rectangular coordinates were used. The dimensions of the 2D domain were R_y, the length of the core (L) in the y direction, and R_x in the x direction. R_x was computed by considering that half of the cylindrical core section was equivalent to a rectangle with the same area with sides d (core diameter) and R_x (Fig. 3c). The domain was composed of two parts: (1) high permeability zone (fracture, large porosity) and (2) rock matrix (small porosity). The fracture zone (zone 1) was on the left of the rectangular domain, parallel to the flow direction (y axis), and had a thickness equal to half of the experimental fracture aperture (*i.e.*, the first element along the x direction). An appropriate number of elements in the x and y directions was selected in each simulation (see detailed spatial discretization in Garcia-Rios et al., 2017). The model considered advection and dispersion only along the fracture. Solute transport in the rock matrix was only by diffusion.

Parameterization

Mineral dissolution and precipitation reactions: equilibrium constants. Modeling used equilibrium constants, stoichiometric coefficients and parameters for activity coefficient calculation from the EQ3/6 database included in the codes (Wolery et al., 1990), with the exception of the equilibrium constant for gypsum at 60 ºC which was as measured by Garcia-Rios et al. (2014). The log K_{eq} values for the C-S-H and C-A-S-H gels were obtained from the solid solution model in Kulik and Kersten (2001) and Myers et al. (2015), respectively. The log K_{eq} value and the molar volume for Si-hydrogarnet ($C_3(A,F)S_{0.84}H_{4.32}$) were calculated assuming an ideal solid solution between $C_3AS_{0.84}H_{4.32}$ and $C_3FS_{0.84}H_{4.32}$ using the data from Dilnesa et al. (2011, 2012, 2014). The log K_{eq} values for portlandite, hydrotalcite-OH, ettringite were obtained from Hummel et al. (2002) and cemdata07 database (Matschei et al., 2007; Lothenbach et al., 2008; Schmidt et al., 2008), respectively. The dissolution and precipitation reactions considered in the simulations under all the conditions studied are given in Table 3.

Mineral dissolution and precipitation rates: forms of the rate laws. The values of the rate constants, a_H^+ terms and m_1 and m_2 exponents in the affinity term of the reaction rate law are normally taken from experimental studies that were compiled in Palandri and Kharaka (2004) and from Domènech et al. (2002), Hamer et al., 2003; Bansdtra et al. (2008), Bibi et al. (2011) and Hellmann et al. (2010) (Table 4). Nevertheless, experiments performed recently to study the kinetics of mineral dissolution/precipitation reactions that are significant for the acid-water-rock interaction have provided new rate laws (calcite: Xu et al., 2012; chlorite: Smith et al., 2013b; Black and Haese, 2014; Zhang et al., 2015; smectite: Cappelli et al., 2018). Xu et al. (2012) proposed a calcite dissolution rate that improves the rate-ΔG_r dependence under close-to-equilibrium conditions ($-12 \leq \Delta G_r \leq 1.7$ kJ/mol) with respect to the simplest TST-based rate law ($m_1 = m_2 = 1$ in Equation (13)). Cappelli et al. (2018) showed the importance of calculating specific values for the m and n parameters of the $f(\Delta G_r)$ term (Eq. 12) in the rate laws in order to better account for the dissolution kinetics of clay minerals. The rate constant for portlandite was $10^{-5.4}$ mol m^{-2} s^{-1} as reported in Bullard et al. (2010). The C-S-H solid solution was discretized into different stoichiometries, ranging from Ca/Si = 1.67 to Ca/Si = 0.83 (Table 3). The dissolution rate constants of the discretized C-S-H gel were obtained by Trapote-Barreira et al. (2014). For the rest of the phases present in the mortar (ettringite, monocarboaluminate, Si-hydrogarnet and hydrotalcite-OH) the rate constants were sufficiently high to allow fast kinetics (local equilibrium).

Mineral reactive surface area. In the continuum models, which make use of the REV (Representative Elementary Volume) approach, the mineral reactive surface area is a bulk parameter. When the specific (BET) surface area of the initial solid can be measured (e.g. micro-meter size grains), a resulting total surface area can be calculated. However, when determination of the BET surface area is not possible (e.g. millimeter-, centimeter-size fragments or rock cores), a geometric reactive surface area, calculated by assuming for instance spherical fragments, can provide an estimated value of the reactive surface area. However, model fits to experimental data (i.e. concentrations of elements at the outlet and pH) use the reactive surface areas as an adjustable parameter given a specific mineral reaction rate law. As explained below, relatively small reactive surface areas are required for fast-reacting minerals (e.g. calcite). For secondary phases, fast rates (implemented through the use of large surface areas) result in the assumption of local equilibrium (Table 5).

Flow and transport parameters. The Darcy velocity, q, was computed according to the volumetric flow rates and the appropriate cross-section areas of the columns ($q = 7 \times 10^{-7}$ to 4.5×10^{-6} m^3 m^{-2} s^{-1}) and the fracture apertures in the percolation experiments ($q = 7 \times 10^{-4}$ to 3×10^{-1} m^3 m^{-2} s^{-1}). Mineral reaction rates in stagnant domains (e.g. impermeable rock matrix next to a fracture, unfractured Portland cement) are strongly limited by diffusional solute transport. Effective diffusion coefficients (D_e) can be calculated from empirical relations between D_e and porosity such as Archie's Law, but these D_e values usually have to be adjusted according to measured results. The models also consider a dependency of D_e on the changing porosity such as (Archie's law)

$$D_e = \phi^n D_o \qquad (18)$$

where D_o is a reference diffusion coefficient and n is the cementation exponent (2-2.5) used in the simulations (Domenico and Schwartz, 1990; Revil and Cathles, 1999). The longitudinal dispersivity (α_L) used in the simulations was of the order of 10% of the length of the columns.

In the fractured cores, the initial porosity of the fracture zone was defined to be 100% whereas initial porosity of the rock matrix and cement zones was 5- 6% for limestone, sandstone

and marl and 11% for cement. Flow field was updated according to porosity, ϕ, and permeability, k, changes. The code solved Darcy's law (neglecting the buoyancy term)

$$q = -\frac{k}{\mu}\nabla P \quad (19)$$

where μ is the dynamic viscosity and P is pressure. Permeability was updated at each time step according to

$$k = k_0\left(\frac{\phi}{\phi_0}\right)^3 \quad (20)$$

MCRTM IN CO_2-RICH WATERS

Column experiments: reservoir and cap rocks

Columns filled with rock fragments provided a porous medium to quantify the geochemical processes (García-Rios et al., 2014; Dávila et al., 2017; Thaysen et al., 2017). Variation of total pressure, P_{CO2}, temperature and rock mineralogy improved our understanding of the effects of these parameters on the coupled dissolution/precipitation reactions and on porosity, pore structure and permeability of reservoir and cap rocks.

Experimental results showed an increase in pH, an excess of Ca ($\Delta C_{Ca} > 0$) and a deficit in S ($\Delta C_S < 0$) (Fig. 4a,b,c). The experiments with sandstone and marl rocks showed an additional increase in Si and Fe (ΔC_{Si} and $\Delta C_{Fe} > 0$) (Fig. 4d,e). It was observed that the output pH decreased with increasing P_{CO2} from atmospheric to supercritical CO_2 conditions (pH ≈ 7-8 and 4-6, respectively).

1D simulations. For the simulations, the rate laws including the values of the rate constants were taken from literature (Table 4). 1D simulations showed that dissolution of calcite in limestone, sandstone and marl and dolomite in dolostone led to the increase in pH and to the excess of Ca. To match the measured [Ca] concentrations the values of calcite and dolomite reactive surface area were reduced one to two orders of magnitude with respect to the calculated geometric ones (Table 5). The resulting small range of values was attributable to both rock heterogeneity and rock structure (silicate content, grain size etc.; Noiriel et al., 2009) and provided a good fit to all experimental results, corroborating this modeling approach.

The increase in ΔSi was associated with dissolution of albite and microcline. To reproduce the measured [Si] concentrations, the reactive surface areas of the Si-bearing minerals were larger than the geometric values (Table 5). An explanation for the diminished values of the reactive surface areas of calcite and dolomite (i.e. small reactivities) can be given by the solute transport control of the rates due to diffusion, at pore scale, from or to the carbonate mineral surfaces at low pH (e.g., Sjöberg and Rickard, 1984). However, the increase in the reactive surface area values of the aluminosilicates is attributed to different size, shape and surface roughness of these minerals (Deng et al., 2018). The value of quartz reactive surface area was nearly the same in all calculations because of the negligible quartz dissolution at this pH range (4-6).

To fit the S deficit, which was mainly controlled by gypsum precipitation (Fig. 5), the reactive surface area of gypsum was smaller at elevated pressure than at atmospheric pressure (Table 5). As for the other secondary minerals (e.g. kaolinite, mesolite, stilbite, scolecite, boehmite, gibbsite, diaspore and alunite), their initial reactive surface areas were assumed to be sufficiently high to allow fast precipitation, i.e. local equilibrium conditions (Table 5).

It is worth highlighting that to test the non-linear effect of P on CO_2 solubility and mineral equilibria (through the molar volume of solutes) reported by Appelo et al. (2014), simulations using the CrunchFlow and PhreeqC (v.3; Parkhurst and Appelo, 2013) codes were compared. Under supercritical conditions, using the same reactive surface area value for calcite dissolution, gypsum did not precipitate in the PhreeqC (v.3) simulation since these calculations considered the rise in the solubility of gypsum to be due to the increased pressure. Therefore, at $pCO_2 > 20$ bar, model calculations should consider the P effect on equilibrium constants to yield more reliable predictions.

Geochemical processes and porosity evolution. Simulations showed that calcite dissolution was greater than that of dolomite, albite, illite, and clinochlore, and the precipitation of gypsum was also much larger than that of any other secondary mineral (kaolinite, mesolite, stilbite, boehmite, gibbsite, diaspore, alunite, muscovite and goethite). The volume of precipitated gypsum was always smaller than the larger volume of dissolved calcite, yielding in all cases a porosity increase. The volume of dissolved limestone was larger than that of dolostone owing to the faster calcite dissolution kinetics. Likewise, a rise in P_{CO2} results in a drop in pH, which substantially increases the calcite dissolution rate with respect to that of dolomite (Pokrovsky et al., 2005, 2009).

As for the temperature effect, under all pCO_2 conditions, low temperature favored calcite dissolution rate although the calcite dissolution rate constants increase with temperature (up to 100 ºC; Pokrovsky et al., 2009). This inverse tendency is attributed to the fact that calcite undersaturation was increased by lowering the temperature. In addition, a rise in CO_2 solubility with decreasing temperature (Duan and Sun, 2003) also contributes to a faster dissolution rate with decreasing temperature. The volume of precipitated gypsum was barely influenced by temperature variations. Simulations showed that an increase in temperature did not affect the trend of porosity variation along the columns (Fig. 6a) but reduced porosity creation (Fig. 6b).

When raising P_{CO2}, the calcite dissolution rate increased along the columns because of the direct pH effect on the calcite dissolution rate (buffering effect of dissolved CO_2 on pH). Model results show that under high pCO_2 conditions pH remains acidic (ca. 5 due to the carbonic acid buffer capacity) and the brine is permanently undersaturated with respect to calcite, dolomite, clinochlore, albite and illite, yielding a higher increase in porosity all over the rock-brine contact. As a result, a rise in P_{CO2} changed the pattern of porosity variation along the column, increasing the distance affected by dissolution (Fig. 6c).

Co-injection of SO_2. Oxidation near the well bore promotes formation of sulfuric acid, leading to additional brine acidification (Knauss et al., 2005; Xu et al., 2007). Thaysen et al. (2017) showed that relative to pure CO_2 experiments, the co-injection of 0.4% SO_2 as H_2SO_4 lowered the pH of the injected brine by ca. 1.5 pH units with respect to the pH of ca. 3.6 of H_2SO_4-free brine. The lower brine pH elevated the dissolution of calcite relative to pure CO_2 conditions, which in turn triggered more gypsum precipitation.

In contrast to the CO_2-experiments, in which one value for the reactive surface area of calcite was enough to match the experimental data, for the 1-D modeling of the CO_2+H_2SO_4 experiments, stepwise reductions of the calcite reactive surface area over time (e.g. from 250 to 32 $m^2_{mineral}$ $m^{-3}_{bulk\ rock}$ (limestone) or from 15 to 7 $m^2_{mineral}$ $m^{-3}_{bulk\ rock}$ (sandstone); Table 5) were used to simulate an effect of gypsum coating of the calcite surfaces (partial passivation). Daval et al. (2009) and Harrison et al. (2015) showed the effect that surface coating may exert on dissolving phases (Si-rich and Ca-rich layers on wollastonite surface and carbonation on brucite, respectively). To account for the passivation effect the former authors used a shrinking particle model and the latter ones proposed an empirical function that related the reactive surface area to

the extent of brucite conversion. In the current study, the stepwise reduction of calcite area was used to implement the corresponding reduction in the reactivity of calcite. The three studies highlight the relevance of including a surface passivation effect on mineral dissolution in MCRTM.

Simulations showed that the marl rock showed higher reactivity over limestone and sandstone and had the highest gypsum precipitation rate relative to the rate of dissolving calcite. Nevertheless, there were no indications of gypsum coating on calcite grains in the marl experiments. This suggested a different growth mechanism of gypsum in marl versus sandstone and limestone rocks, e.g. a predominance of needle growth versus surface coating, which may be attributed to the high silicate content in the marl rock.

Column experiments: reservoir/cap rocks and Portland cement

Brine circulated through columns filled with alternating layers of fragments of rocks (limestone, sandstone and marl) and hydrated Portland cement at P_{CO2} of 10 bar (experimental set-up (Fig. 1b) and model implementation (Fig. 3b)). These experiments provided a porous medium in which advective transport (inter-grain porosity of ca. 50%) and diffusive transport (cement porosity of ca. 15%) occurred. These elevated P_{CO2} conditions are suitable for determining the extent of the reactions involved in the interaction between CO_2-acidic brines and carbonate rock/cement, which is crucial for the assessment of wellbore integrity (Carroll et al., 2011).

2D simulations. To match the experimental concentrations of the output solutions the reactive surface area values of calcite (rock) and C-S-H-1667, ettringite and hydrogarnet (cement) were reduced with respect to the geometric values. In contrast, the hydrotalcite reactive surface area was increased. Large values for possible secondary phases (e.g. gypsum, dolomite, muscovite, kaolinite, stilbite, C-S-H with variable Ca/Si ratio, aragonite, alunite and mesolite) allowed local equilibrium. Diffusion through cement fragments was calculated using an initial $D_e = 1\times 10^{-11}$ m^2 s^{-1}.

Calculations showed that dissolution of portlandite caused an initially elevated pH of ca. 12. After portlandite exhaustion, calcite dissolution buffered the solution pH. The release of Ca and the injected sulfate content were sufficient to allow gypsum precipitation in the rock and cement layers (Fig. 7a). In the cement layers, ettringite and hydrogarnet dissolved partially whereas hydrotalcite and portlandite dissolved totally. Calculated precipitation of aragonite in the two cement layers agreed with the observed formation of aragonite rims on calcite grains (Fig. 7b). In the three cement-rock columns, the volume of dissolved phases exceeded the volume of precipitated ones, yielding increases in porosity. Simulated variation of the resulting porosity displayed different patterns among the experiments (Fig. 8a). Porosity was higher near the inlet in the limestone than in sandstone and marl due to more dissolution of calcite in the former experiment (Fig. 8b). Larger calcite dissolution in the second rock layer in the sandstone and marl experiments enhanced porosity in this region. A marked porosity increase in the cement layers was due to dissolution of portlandite and ettringite, where the volume of precipitated aragonite was relatively smaller.

Therefore, it is deduced that in the carbonate rock-cement contact under elevated P_{CO2}, calcite dissolution in the rock and portlandite and ettringite dissolution in the Portland cement were the reactions that controlled the changes in mineralogy. Gypsum and aragonite precipitates were the main secondary minerals involved in the porosity evolution.

Percolation experiments: reservoir and cap rocks

García-Rios et al. (2015, 2017) and Dávila et al. (2016a, 2016b) focused on the effects that solution composition and flow rate exert on the hydrodynamic and geochemical evolution of artificially fractured cores. Limestone, sandstone and marl samples (Table 1) reacted under supercritical CO_2 conditions. 2D reactive transport modeling was performed to quantify the dissolution and precipitation processes which induced a number of dissolution patterns: face dissolution (only dissolution at the inlet and no further alteration along the fracture), wormhole (preferential flow path) formation or uniform dissolution along the fracture.

Experimental results showed that the output [Ca] and [Si] concentrations were always higher than the input ones, indicating dissolution of calcite, microcline (sandstone) and clinochlore and albite (marl). A S deficit was caused by gypsum precipitation. The volume of dissolved calcite was always larger than that of precipitated gypsum. As regards fracture changes, it was observed that in the limestone experiments (Fig. 9a), a preferential path (wormhole) started in regions with high initial permeability (i.e., fracture surface heterogeneities), and formed single wormholes could divert and develop branching near the outlet. Fracture surface became rough at slow flow rate. Gypsum precipitated preferentially where calcite surface roughness increased (Fig. 9b). In the sandstone experiments, calcite dissolution left non-dissolved grains of quartz and microcline along the fractures (Fig. 9c), leading to increases in non-uniform aperture. In the marl experiments (Fig. 9d,e), dissolution of calcite contributed to the formation of a highly porous reacted zone with a width up to 300 μm, made up of non-dissolving quartz, illite and pyrite, partially dissolved silicate grains and precipitated gypsum.

2D simulations. The match between the experimental aqueous chemistry and the model variation was obtained by adjusting the values of the mineral reactive surface areas and the initial effective diffusion coefficients. In the three fractured cores, advection was the dominant mass transport process in the fracture, and the solute transport in the rock matrix was attributed only to diffusion.

In the limestone fractured core, where face dissolution formed, the output [Ca] and [S] concentrations and the resulting porosity with distance normal to fracture (Fig. 10a) were reproduced by reducing the calcite reactive surface area (Table 5) and considering $D_e = 5.6 \times 10^{-13}$ m^2 s^{-1} and $n = 2.5$ (Eq. 18) for diffusion through the rock matrix.

Figure 10b compares the calculated porosity variation with distance normal to fracture and the one measured by SEM in the sandstone fracture, where uniform dissolution developed. Although the distance normal to fracture affected by dissolution next to the inlet was slightly shorter in the model, the calculated porosity variation was consistent with the experimental dissolution pattern. To reproduce the experimental data, a larger D_e value (1.9×10^{-11} m^2 s^{-1}) and $n = 2$ (Eq. 18) a reduced calcite reactive surface area value (Table 5) were considered. The calculated value of geometric surface area was reduced owing to the transport-controlled dissolution rate of calcite at pH < 5.

In the marl simulations, the calcite reactive surface area value was also diminished relative to the geometric value (Table 5). To match the measured [Fe] concentration, the reactive surface area of clinochlore was six orders of magnitude larger than the geometric surface area, which was not unreasonable for a clay mineral (e.g., 4.4×10^8 $m^2_{mineral}$ m^{-3}_{rock} for the clayey caprock at Sleipner; Gaus et al., 2005). A good match for [Si] was achieved by using reactive surface area values of albite and clinochlore that were two to five orders of magnitude larger than the

geometric values (Table 5). Dissolution of quartz and illite was negligible. Precipitation of gypsum was reproduced using a value of reactive surface area smaller than the values used for precipitation of clay minerals (smectite and kaolinite), zeolites (mesolite, stilbite, scolecite and gismondine) and aluminum oxyhydroxide (boehmite), which were sufficiently high to allow fast precipitation (local equilibrium).

In the experiment with fast Darcy velocity, $D_e = 6 \times 10^{-12}$ m^2 s^{-1}, which was greater by a factor of 20 than the value used in slow velocity ($D_e = 1 - 3 \times 10^{-13}$ m^2 s^{-1}). This increase was probably due to a fast flow rate that would result in less transport control, which was reproduced in the model using a large initial D_e. However, in the experiments with high flow rate, a poor match was obtained where a wormhole dissolution pattern formed. The rectangular geometry of the model domain could not reasonably account for the evolution of the cylindrical geometry related to wormholing. Discrepancies between the calculated and measured concentrations were therefore to be expected.

MCRTM: limitations and alternative approaches

Using MCRTM to successfully simulate the experimental results presented above, we encountered a number of problems that should be resolved to improve future modeling.

The transport control of the rates due to diffusion from or to carbonate mineral surfaces at low pH, which is not included explicitly in this type of model, obliged us to diminish the reactive surface areas (i.e., reduction in calcite reactivity) with respect to the estimated geometric value. The range of diminished values in the calcite surface area varied several orders of magnitude to simulate column experiments with a homogeneously distributed pore space and cores with finely characterized short fractures. The variation in calcite reactive surface area was dependent on the fluid residence time. In contrast, reactive surface areas of the Si-bearing minerals were enlarged because of surface roughness. Beckingham et al. (2016) produced Image Perimeter specific surface areas for quartz and Mg- and Al-silicate minerals to quantify the physical surface area in contact with the reacting fluid (pH = 3.2). Therefore, MCRTM of the experimental results from pristine or fractured cores with a heterogeneous pore space or fractures displaying local heterogeneities (surface roughness, high permeable zones) demands a suitable fit of the effective (reactive) mineral surface area.

A stepwise reduction of the calcite reactive surface area was implemented to simulate calcite passivation by gypsum coatings. Since these codes assign average property values (e.g. porosities, surface areas, diffusion coefficients, etc.) to each numerical element (REV approach) and do not consider an explicit representation of mineral grains and their surfaces (pore scale representation), an added limitation due to diffusion to and from the mineral surfaces to the bulk solution was not included. Thus, calcite passivation was only reproduced by reducing calcite reactivity by decreasing the reactive surface area of calcite.

Modeling the coupled mechanisms of transport and reaction in fractures when localized dissolution (wormhole) occurred is complex. In our case, the rectangular geometry of the model domain could not reasonably account for the evolution of the cylindrical geometry due to wormholing. A new model accounting for the wormhole formation is warranted to interpret the experimental results under fast flow. It is therefore necessary to use numerical approaches which consider local heterogeneities (e.g. Szymczak and Ladd, 2011; Soler-Sagarra et al., 2016).

We used 2D reactive transport modeling to simulate fractured cores that underwent face and uniform dissolution. In the marl fracture, when porous layers formed by the non-dissolved minerals remaining behind the dissolution reaction front, non-reactive minerals formed a porous layer which prevented the solution from easily accessing the reactive minerals of the matrix

(calcite). This diffusion-controlled phenomenon resulted in a decrease in calcite dissolution. Deng et al. (2016) performed 2.5 D reactive transport modeling to study fracture alteration in a dolostone core (87 wt% dolomite and 10 wt% calcite), taking into account the permeability heterogeneity in the fracture plane and thickness variation of an altered layer. Effective mineral reaction rates as a function of the effective diffusion coefficient were considered as an alternative solution to better understand fracture alteration under different flow regimes (Deng and Spycher, 2019, this volume). In their calculations, the D_e value (10^{-10} m^2 s^{-1}) was about two orders of magnitude greater than the ones fitted in our simulations for calcite-rich carbonate rocks. Additionally, a cubic law developed for fractures to calculate fracture permeability was used instead of the Kozeny-Carman relationship (Eq. 20).

It should be pointed out that as shown by Elkhoury et al. (2013), dissolution patterns in fractures resemble those in porous media where dissolution features evolve from face dissolution to wormhole formation when increasing the flow rate (Golfier et al. 2002; Kang et al., 2014). The main difference lies in the fact that the presence of fractures focuses the wormholes along the fractures. However, under high flow rates, preferential flow paths grow uniformly, compared with the formation of ramified wormholes in porous media. In our research with carbonate rocks, the fragments-filled columns and the fractured cores represent highly porous and fractured subsurface media, respectively. Carroll et al. (2013), Smith et al. (2013a), Hao et al. (2013) and Smith et al. (2017) used mostly intact cores with pore-scale heterogeneities to quantify the reactivity of carbonate rocks with a variable mineralogy content (vuggy limestone, marly dolostone and dolostone) under supercritical P_{CO2} conditions. The outcomes achieved in these studies are very informative for comparison and should be regarded in further modeling. First, it was shown that in limestones wormholes initiated and developed in areas of greater porosity and permeability contrast, following preexisting preferential paths. Taking into account that a fracture is a preferential path, our fractured limestone cores developed wormholes in a similar way subject to high flow rates. Second, two median values for the exponent n in the permeability-porosity relationship (Eq. 20) were derived: n = 7 for vuggy limestone with heterogeneously distributed pore space and n = 3 (as the one used in our simulations) for marly dolostone regardless of pore space distribution. 2D simulations of our fractured cores using n = 3 together with solute diffusion through the porous rock matrix captured reasonably well the fracture evolution observed when face dissolution and uniform dissolution prevailed. It was perhaps in the wormholing simulations when the difficulties encountered could have been overcome by using a full 3D model together with a higher n value. In their 3D simulations the rate constants for calcite and dolomite were variably diminished up to two orders of magnitude with respect to those reported in the literature (Palandri and Kharaka, 2004). This finding is in line with our reduction of the estimated geometric surface area by about two orders of magnitude to account for the diffusion-controlled rate of calcite.

MCRTM IN AMD-WATERS

Interaction between AMD and Portland cement/sedimentary rock

Mitigation and regional control of AMD require the construction of concrete-based structures, such as aeration cascades, tanks to hold the materials of the passive treatment systems (Figs. 1e and 2), and dams to control the level of the rivers. The durability of these concrete-based structures depends very much on the processes arising from the interaction between the concrete and the AMD water. Given that these highly polluted waters have very low pH ($0 < pH < 4$) and high concentrations of sulfate, iron, aluminum and metal(loid)s, the dissolution of the

cement phases (e.g. calcium silicate hydrate (C-S-H) and portlandite), precipitation of secondary minerals (gypsum, goethite, schwertmannite, ettringite, etc.) and adsorption of metal(loid)s will be the dominant reactions that determine the fate of the concrete-based structures.

Column experiments. We are studying the effect of these reactions on the mineralogy of cement and rock and to evaluate the consequences for concrete durability. To this end, column experiments with two alternating layers of milimetric-size fragments of sandstone and Portland cement were carried out (Table 1 and Fig. 1b). The columns were filled with two alternating layers of rock and cement with an approximate intergrain porosity of 65% (Fig. 1b). An input solution of pH = 2 (H_2SO_4) containing Al, Ca, Mg and Fe(II) as major ions and arsenate and divalent cations (Zn, Cd and Ni) as minor components was injected at a constant flow rate from the bottom upwards (Table 2).

During the experiments, pH rapidly increased to ≈ 12.5, after which it decreased, remaining at ≈ 6 until the conclusion of the experiments (Fig. 11a). The output Ca concentration exceeded the input one in contrast to that of S, which always showed a deficit. The evolution of the concentrations of the divalent cations (Fe(II), Zn, Cd and Ni) showed almost total depletion of metals at the high pH and partial elimination as pH decreased (Fig. 11b-e). This behavior was attributed to the formation of metal hydroxides at high pH. In contrast, arsenate depletion occurred throughout the experiments (not shown), suggesting adsorption onto Fe-hydroxides (e.g. goethite).

1D simulations of the column experiments corroborated that precipitation of gypsum and aragonite occurred at the expense of total and partial dissolution of portlandite and calcite, respectively. Formation of basaluminite was also calculated (Fig. 11f). These mineralogical changes yielded a marked increase in porosity at the inlet of the columns and a significant decrease in porosity in the first sandstone layer (Fig. 11g). SEM-EDS observations and XRD analyses corroborated the absence of portlandite in the cement matrix and the presence of newly formed gypsum and aragonite. Note that basaluminite identification by XRD is highly difficult given the poor crystallinity of this Al oxyhydroxisulfate (Lozano et al., 2018).

Concrete cores. The AMD-treatment plant at the Esperanza mine in the Iberian Pyrite Belt (Huelva, south Spain) is used as a case study of interaction between AMD and concrete. To this end, concrete cores (2 - 6 cm long and 2.5 cm in diameter) were sampled at the 3-year-old Esperanza II Mine AMD treatment plant. SEM-EDS inspection of thin sections along the concrete core samples showed that alteration mainly occurred at the concrete-AMD interface (top 2-3 mm) (Fig. 12), revealing precipitation of Fe-rich phases on top of the concrete and little concrete alteration, which was not observed further into the cores.

Figure 13 shows the results of a preliminary 1D simulation in which an AMD water of pH 2.7 and rich in sulfate, Al and Fe (II) is in contact with concrete, which is the situation at the ME2 point at Mina Esperanza (Fig. 2). AMD flows continuously along the channel, with a rather constant composition with time (pH = 2.7, [Ca] = 3.0 mM, [Mg] = 5.7 mM, [Si] = 1.5 mM, [Al] = 3.9 mM, [SO_4] = 27 mM, [Fe_{TOT}] = 9.7 mM), and this water interacts with the concrete at the floor of the channel. In the simulations, the AMD water composition is fixed in the first 2 nodes of the domain (channel), but schwertmannite is allowed to precipitate, as observed in the channel at Mina Esperanza. Solute transport along the concrete is only by diffusion using an initial De value of 1.59 $m^2\ s^{-1}$.

Schwertmannite precipitation kinetics in the channel was adjusted so that precipitation occurred progressively with time, as observed. In the concrete, the acidic water causes the dissolution of portlandite, but the high sulfate and Al content of AMD promotes the intense precipitation of ettringite, which quickly clogs porosity right next to the interface. The clogging

of porosity severely limits concrete alteration (Fig. 13a). Other reactions are some decalcification of C-S-H (dissolution of primary C-S-H and precipitation of C-S-H with lower Ca/Si), precipitation of small amounts of hydrotalcite, calcite, brucite and ferrihydrite, and dissolution of primary monocarboaluminate. The model results showed a very thin alteration zone right at the concrete-AMD interface (Fig. 13b), suggesting that alteration under the aggressive AMD conditions is very limited.

Interaction between AMD and limestone

AMD that flows through the limestone sand used in the treatment systems (e.g. anoxic limestone drain (ALD) or disperse alkaline substrate (DAS) tanks), dissolves calcite, raising pH and alkalinity, yielding trivalent metal retention as Me-oxyhydroxide precipitates (Me = Al and Fe(III)). The efficiency of these passive systems is however limited because secondary mineral precipitation (e.g. gypsum) causes the passivation (armoring) of the limestone grains and clogging of the pores, reducing limestone reactivity and acid neutralization (Caraballo et al., 2009a; 2011; Soler et al., 2009).

To gain further insight into the loss of calcite reactivity due to grain coating or clogging of porosity, Offedu et al. (2015) performed column experiments using limestone (fragment size = 1-2 mm and inter-grain porosity = 49%; Fig. 1b) and synthetic acid solutions (pH of 2-3, H_2SO_4; Table 2) containing Fe(III) and Al with concentrations that fell in the range found in AMD (Nordstrom et al., 2000). X-ray microtomography (mCT) measurements showed how the gypsum coating-calcite passivation (Booth et al., 1997; Offedu et al., 2014) and precipitation of metal oxyhydroxides influenced the porosity changes in the columns (Fig. 14). The dissolution of calcite (limestone) released Ca, which combined with the SO_4 in solution, caused precipitation of gypsum on the calcite surfaces. As a result of passivation, output pH dropped to values close to the input value, metal retention stopped and SO_4 concentrations came close to the initial value (or even higher if gypsum dissolved). Calcite dissolution also caused an increase in pH from 2 to ≈ 6-7 (proton consumption), resulting in supersaturation of the solutions with respect to Fe- or Al-oxyhydroxides. Precipitation of metal-oxyhydroxides between the grains (Fig. 14) caused clogging. The overall process is represented by the following reactions

$$CaCO_3 + 2H^+ \rightleftharpoons Ca^{2+} + H_2CO_3 \quad (21)$$

$$Ca^{2+} + SO_4^{2-} + 2H_2O \rightleftharpoons CaSO4 \cdot 2H_2O(s) \quad (22)$$

$$Fe^{3+} + 3H_2O \rightleftharpoons FeOOH(s) + 3H^+ \quad (23)$$

Microtomography examinations were performed at different times (Fig. 14): the four mCT images show the same section close to the column inlet. Initially (d0) only calcite grains were present (light gray), separated from each other by pore space (dark areas). After 4 days (d4), some of the calcite grains were coated by a thin gypsum layer (dark gray) and a whitish phase (goethite as identified by μXRD) filled the pore space. After 8 and 12 days (d8 and d12), the gypsum coatings grew and goethite content increased, yielding column passivation. The contribution of gypsum and goethite precipitates to porosity decrease calculated by mCT image segmentation was ca. 15% (goethite) and ca. 5% (gypsum) from the inlet to the middle of the column.

1D simulations. 1D modeling was performed to simulate the processes occurring in the columns. Since passivation was controlled by gypsum coating on calcite surfaces, calcite reactivity diminished as a result of the loss of calcite reactive surface area. Given that the calcite passivation was not implemented in the CrunchFlow code, as in the CO_2-H_2SO_4 modeling

described above, the calcite reactive surface area was decreased stepwise (Table 5; Fig. 15). The reactive surface areas of goethite and gypsum were assumed to be constant during the experiment (Table 5). This was a model simplification since absolute areas should increase with precipitation. But even with this underestimation of gypsum and goethite reactivity it was necessary to reduce the calcite surface area to match the experimental results. This simple model (stepwise reduction of calcite surface area) showed that the experimental results are consistent with a reduction of calcite reactivity induced by the precipitation of gypsum (passivation mechanism).

Interaction between AMD and DAS: column experiments

The performance of an AMD remediation treatment depends on the relationship between the AMD flux and the dissolution rate of the reagent. Prior to building a field-scale system, this relationship must be quantitatively investigated through column experiments and MCRTM. In the columns, the flux is imposed by scaling both the field discharge and the expected surface of the treatment plant. The adequate dissolution rate of the reagent (e.g. calcite), however, can be obtained by selecting the grain size and the reagent-wood shavings ratio. Owing to the non-linear relationship between flux and chemical reactions, MCRTM is necessary to obtain an optimum criterion for the reagent dissolution rate (Eq. 12).

The dissolution rate constant for calcite was obtained from earlier studies (Arvidson et al., 2003; Table 4). However, given the discrepancies of the orders of magnitude between experimentally and field derived mineral rates (White and Brantley, 2003), the adjustment of the reagent reactive surface area value is critical for the modeling, as shown above. This is because gas sorption BET methods or geometric approximations are not useful to estimate the amount of solid surface area in contact with flowing water. Column experiments were built to derive a realistic estimation of the reactive surface area. The columns were filled with a mixture of 1-3 mm calcite fragments and wood shavings with a 1:1 weight ratio. Hydraulic conductivity profiles of the substrates were determined by connecting piezometric standpipes to every pressure measuring port (Fig. 1d). Head-loss between the different ports was then measured at high flow rates by reading the piezometric head difference between adjacent pipes (Rötting et al., 2008a). The water flow was imposed throughout the head difference between the inflow and outflow water head, and the main parameters controlling solute transport, porosity and dispersivity were determined by injecting water with a conservative solute and analyzing the breakthrough curve. Once the flux and transport properties are known, the sampling points at different depths of the columns provide solution chemistry data to be reproduced with MCRTM using A_m (Eq. 12) as the only fitting parameter (e.g. column in Fig. 16). 1D simulations matched the experimental results by diminishing the calcite reactive surface area to 180 $m^2_{mineral}\ m^{-3}_{bulk\ rock}$ (Table 5).

Calcite dissolution is the main mineral controlling the evolution of the AMD hydrochemistry along the treatment. However, there are some other mineral phases governing the specific processes responsible for Al and Fe removal within the limestone-DAS reactive material. As evidenced in Figure 16a-e, the pH increases in two steps that occur when all the Fe and Al have been removed from the water. Mineral precipitation takes place in two different fronts (Fig. 16f). In the column, from bottom to top the first front corresponds to the precipitation of hydrobasaluminite (bas) and is formed at the expense of the alkalinity produced by calcite dissolution

$$4Al^{3+} + SO_4^{2-} + 5CaCO_3 + 41H_2O \rightleftharpoons 5Ca^{2+} + 5CO_2(aq) + Al_4SO_4(OH)_{10}\cdot 36H_2O \qquad (24)$$

Upstream from the Al front, schwertmannite forms at the expense of the alkalinity produced by

dissolution of calcite

$$8Fe^{3+} + SO_4^{2-} + 11CaCO_3 + 8H_2O \rightleftharpoons 11Ca^{2+} + 11CO_2(aq) + Fe_8O_8SO4(OH)_6 \cdot 5H_2O \quad (25)$$

However, when calcite reagent is exhausted, schwertmannite also forms at the expense of the alkalinity released by basaluminite dissolution

$$8Fe^{3+} + 2.2Al_4SO_4(OH)_{10} \cdot 36H_2O \rightleftharpoons 8.8Al^{3+} + 1.2SO_4^{2-} + Fe_8O_8SO_4(OH)_6 \cdot 5H_2O + 82.2H_2O \quad (26)$$

The consumption of hydrobasaluminite at the schwertmannite front is also evidenced by the increase in Al concentration far above the inflow concentration (Fig. 16c). This increase in Al concentration is also clearly observed in field-scale treatments (Rötting et al., 2008b; Caraballo et al., 2009a, 2011) and is an additional contribution to downstream hydrobasaluminite formation. This localized precipitation of hydrobasaluminite is a major threat to hydraulic conductivity, as discussed below. In fact, hydrobasaluminite can contain up to 36 water molecules, and it shows a characteristic jelly aspect. Its molar volume is very difficult to measure. An estimate of 482 cm^3 mol^{-1} is obtained from the specific gravity of basaluminite, (2.12 g cm^{-3}), adding the weight of up to 31 water molecules. Accordingly, the reaction of basaluminite formation leads to an increase in the volume of the solid phases and almost reduces porosity and hydraulic conductivity to zero.

Moreover, calcite dissolution will increase Ca concentration in the water (Fig. 16d), and AMD from the Iberian pyrite belt (IPB) often contains thousands of milligram per liter of sulfate. Therefore, gypsum may also precipitate within the reactive substrate and contributes to passivation of calcite surface fragments and/or clogging the pore space.

Interaction between AMD and DAS: field-scale passive remediation treatment

Design of field-scale treatment: role of reactive surface area. Once the reactive transport model is calibrated using the column results, it can be used to simulate different scenarios of a field-scale treatment. The main parameters to vary are the flux of AMD (m^3 m^{-2} s^{-1}), the AMD chemical composition, the proportion of reactive and inert material, and the thickness of the reactive filling. The performance of a hypothetical treatment of a limestone-DAS system (2 m thick x 250 m^2 of surface and initial porosity of 0.45) to treat AMD from Mina Esperanza (pH = 2.8, [Fe(III)] = 749 mg L^{-1}, [Al] = 167 mg L^{-1} and $[SO_4^{2-}]$= 2720 mg L^{-1}) flowing at 1 L s^{-1} was calculated for two cases with different limestone-wood shavings ratios (Fig. 17). The results showed that in both cases (limestone-wood shavings weight ratios of 2:1 and 1:1) the output water with a pH of 6 retained all Fe and Al (not represented) after 2 years of functioning. Decrease in porosity was located at two depths. The first one was caused by precipitation of high amounts of schwertmannite near the surface. It is not difficult to mechanically remove the surface material during the operation of the treatment system. However, the higher reduction in porosity was due to precipitation of hydrobasaluminite (pH ≈ 4). The a-priori more efficient 2:1 ratio case led to a reduction in porosity, causing clogging. A sensitivity study with the model showed that a lower limestone proportion (limestone-wood shavings ratio of 1:1) slowed the calcite dissolution rate, expanded the reaction front, and caused less concentrated hydrobasaluminite precipitation and less porosity reduction. Therefore, the 1:1 ratio option is more suited to this case. Lower limestone-wood shavings ratios (e.g. 1:2) that mostly prevent porosity reduction are unable to neutralize the water acidity (not represented).

Field-scale treatment: blind MCRTM prediction. The average chemical composition of water at different stages of the treatment after 32 months of functioning is represented in Figure

18. Water oxidation along the aeration cascades and at the first decantation lagoon (Fig. 2) is evidenced by the decrease in Fe(II) and the increase in Fe(III), which will be subsequently precipitated as schwertmannite. pH shows a very small decrease due to water hydrolysis by Fe(III). Arsenic is retained by schwertmannite with a decrease from 300 to 70 μg L^{-1}. The concentrations of the remaining elements do not undergo systematic variations.

The most important changes in the chemistry of water occur inside the first DAS-calcite tank (between sampling points 2 and 3; Fig. 18). pH increases up to 6 and acidity drops to 200 mg L^{-1} $CaCO_3$. Total iron decreases from 600 to 200 mg L^{-1} (due to faster oxidation at higher pH and schwertmannite precipitation), and the remaining aqueous Fe is all Fe(II). The remaining elements, Al, As and Zn (and the other elements that are not represented) are depleted close to or below detection levels. As is adsorbed by schwertmannite (Fukushi et al., 2003), Cu (cation) is probably precipitated as cuprite, and REEs are adsorbed on hydrobasaluminite or co-precipitated in fluorite (Ayora et al., 2016). The other divalent metals are probably precipitated as hydrated complex carbonates (Pérez-Lopez et al., 2011). The role of the second DAS-calcite pond is minor. pH rises to 6.5 and the remaining divalent metals are totally removed from water, only Fe remains in solution in concentrations below 100 mg L^{-1}. Fe(II) was in part oxidized to Fe(III) and precipitated as ferrihydrite (see the different color of the two DAS-calcite tanks in Figure 2). Along the treatment system, sulfate decreases from 3000 to 2000 mg L^{-1} due to precipitation of schwertmannite, hydrobasaluminite and gypsum, but the calcite-DAS is unable to deplete SO_4 below gypsum solubility.

From the MCRTM point of view, the most interesting issue is to check the validity of the predicted functioning of the AMD-treatment plant from the results calculated in the column experiments. Since the Mina Esperanza II system is currently in operation, no evolution on the final outflow composition and no signals of treatment exhaustion are observed. Therefore, the dismantled DAS-calcite tank of Mina Esperanza I (Fig. 2) is suitable to make comparisons between the design predictions and observations.

In the first year, the hydrochemical behavior was fairly steady. Only a slow decrease in water pH from 6 to 5.1 occurred during the last months (Fig. 19a). Systematically analyzed total Fe at the output of the system showed ca. 40% of Fe removal (Fig. 19b), which is similar to the Fe(III) concentration in the inflow (Caraballo et al., 2011a). Aluminum was completely removed during the first year, and only when the pH of the water outflow was close to 5 was a small decrease in the aluminum removal observed (Fig. 19c). 1D simulations reproduced the chemical composition of the outflow water using the reactive surface area value fitted in the column modeling (Table 5). Two cases with the extreme solution composition during the functioning of the calcite-DAS tank were used in the calculations (pH = 2.35 and 2.96; $[Fe_{TOT}]$ = 755 and 1100 mg L^{-1} (40% Fe(III)) and [Al] = 128 and 167 mg L^{-1}; Caraballo et al., 2011). Figure 19 shows that the pH and the measured output Fe and Al concentrations were within the predicted values. Hence, the model successfully predicted the outflow water chemistry for 18 months of the Mina Esperanza I treatment. Discrepancies were observed between the predicted and observed Fe values because Fe(II) was not efficiently removed with only one DAS-reactive system.

As regards the solid phases precipitated within the reactive material, XRD patterns revealed the presence of schwertmannite and goethite as the only detected Fe mineral phase at 0-20 cm depth. No mineral phase was detected in samples at 20-35 and 35-50 cm depth, whereas gypsum and calcite were the only phases detected from 50 to 250 cm depth (Caraballo et al., 2011). Sequential extractions of these samples specifically designed to identify this type of Fe-Al-SO_4-solids (Caraballo et al., 2009b) reproduced the XRD results. Thus, the presence of schwertmannite was detected by the amount of Fe recovered in the third step of the sequential extraction, while the Fe analyzed in the fourth step was attributed to goethite dissolution (Fig.

20a). Although not identified by XRD due to its amorphous nature, the presence of hydrobasaluminite was evidenced by Al recovered in the third step of samples between 50 and 210 cm. The retention of an important sulfur concentration in steps 2 and 3 was attributed to adsorbed and structural sulfate in schwertmannite. The absence of recovered Ca in the second step confirmed the complete calcite dissolution along the Fe-precipitation zone. From 50 to 250 cm, the presence of Ca and S in the first step of sequential extraction and Ca in the second step confirmed the existence of gypsum and calcite, respectively. In spite of the inherent difficulties in comparing real and predicted amounts of precipitates on a quantitative basis, Figure 20b shows a good agreement between the model and the mineralogy and phase distribution observed for 18 months of operation. Therefore, the reactive transport model successfully predicted the treated water chemistry and mineral distribution.

CONCLUSIONS AND REMARKS ON FUTURE WORK

Conclusions

MCRTM is a useful tool to elucidate the reactivity of minerals intervening in geochemical processes. Advances in pore-scale modeling towards precise interpretation of the geochemical processes are promising (Molins, 2019, this volume). Still, MCRTM is able to quantitatively describe the processes dominating the anthropogenic acid water-rock/cement interaction.

Column experiments using crushed carbonate rocks (porous medium) and 1D simulations that reproduced the experimental aqueous chemistry proved useful in gaining fresh insight into the effects exerted by mineralogy, temperature, P_{CO2} and sulfate content on the reactivity of reservoir and cap carbonate rocks. The feasibility for predicting changes in porosity was also confirmed. Percolation experiments were used to measure the outflow aqueous chemistry in fractured cores. 2D simulations of the carbonate rocks that developed different types of dissolution patterns were performed to estimate transport and reaction kinetic parameters. It was inferred that by reducing the calcite reactive surface area and by increasing that of the aluminosilicates with respect to the geometric estimates, MCRTM reproduced the geochemical processes in these laboratory media (centimeter scale).

Thus, for the assessment of CO_2 injection and long-term storage in fractured reservoir and cap carbonate rocks at field scale (meter-kilometer scale), predictions can be reliable, (1) when using diminished values of the calcite reactive surface area to take into account the transport-controlled dissolution of calcite together with elevated values of aluminosilicate reactive surface areas and (2) when considering the effect of the residence time on the kinetic mineral rate laws (Wen and Li, 2017, 2018) given the much shorter residence times in the experiments (from seconds to hours) compared with those (years) in rock formations during CO_2 injection (Bachu et al., 1994). Moreover, MCRTM yields reliable predictions of long-term behavior in reservoir and cap rock fractures under the P_{CO2} and temperature of injection and storage sites by providing a field parameterization (dimensions (aperture and length) and morphology of fractures, reactive (accessible) mineral surface areas and fluid flow regime). Without this information, a sensitivity analysis of the variability of these parameters should be performed.

1D and 2D simulations of the columns with rock/cement filling shed light on the effect of CO_2-rich and AMD-rich-water acidity on carbonate rocks and Portland cement. The dominant processes ((i) calcite passivation by gypsum coating and Fe-rich-phase-clogging, (ii) extensive Portland cement alteration by dissolution of portlandite and precipitation of gypsum and aragonite at elevated P_{CO2}, (iii) precipitation of Fe oxyhidroxides and Al sulfates and (iv) depletion of AMD contaminant metals) indicate the complexity of the acid water - rock/cement interaction. Moreover, MCRTM suggests that secondary mineral precipitation at the AMD-

concrete interface prevents the alteration of cement-based materials used in treatment-plant infrastructures.

Limestone disperse-alkaline-substrate (DAS) column experiments are suitable for building a 1D MCRTM with fully determined parameters. The flux is imposed and porosity and dispersivity (transport parameters) are determined by controlled conservative tracer experiments. The chemical composition of the porewater sampled through the column allows us to calibrate the reactive surface area of the porous medium. Thus, a well parameterized dissolution rate law of calcite, which controls the treatment system, guarantees a fully determined MCRTM. If the material in the column is the same as that for the real case, a realistic prediction of the system performance is possible. This is crucial for designing a field-scale treatment to ensure the optimum consumption of the reagent (e.g. calcite) and to avoid clogging by precipitates. However, in AMD remediation systems, the porous medium is tailored according to a precise characterization of its properties in the laboratory. This optimum situation can hardly be extrapolated to complex subsurface porous media.

Remarks on future work

At field scale, hydrogeologists have considerable experience in determining flow properties of aquifers by means of pumping/injection hydraulic tests. Transport properties are also conventionally determined by means of tracer tests using conservative solutes but with more difficulty. Given our knowledge of the kinetics of water-mineral reactions obtained from laboratory experiments, a successful MCRTM would require a prior characterization of the mineral reactive (accessible) surface area under field conditions. As shown by De Gaspari et al. (2014) and Snaebjörnsdóttir et al. (2017), controlled tracer tests using reactive solutes after conventional hydraulic tests constitute a promising way to make applications of MCRTM that are more realistic for natural systems.

At laboratory scale, performance of new experiments and simulations that closely mimic field conditions (rock/cement mineralogy, fluid composition, heterogeneous pore-space distribution in rocks and fractured media), pressure, temperature and flow variability) will lead to MCRTM improvements. Successful predictive simulations of site-specific cases (Balashov et al., 2013; Zheng et al., 2013; Tutolo et al., 2015b; Wolf et al., 2016; Kampman et al., 2017; Gíslason et al., 2019; Xiao et al., 2019) would require (1) constraining kinetic and flow parameters that control the geochemical processes (2) a review of equilibrium and kinetic parameters (Black et al., 2015; Luttge et al., 2019), (3) the incorporation of experimentally tested power law-based porosity-permeability expressions in porous and fractured media (Gouze and Luquot, 2011; Luhmann et al., 2014; Deng et al., 2016; Smith et al., 2017), (4) estimates of accessible mineral surface area (Beckingham et al., 2016, 2017; Deng et al., 2018) and (5) implementation of stress and chemo-mechanical and thermo-mechanical effects (Carroll et al., 2016; Vilarrasa et al., 2019).

Merging these complementary approaches will improve multiscale MCRTM.

ACKNOWLEDGEMENTS

This work has been financed by the CGL2016-78783-C2-R and CGL2017-82331-R projects (Spanish Ministry of Economy and Competitiveness), with contribution of FEDER funds, and the 2017SGR 1733 Catalan Government project. We would like to thank Jordi Bellés, Natàlia Moreno, Rafael Bartolí and Mercè Cabanas (IDAEA), Eva Pelegrí and Maite Romero (SCT-Barcelona University) and José Antonio Jiménez (CENIM) for analytical assistance. We are

indebted to Francisco Macías (Huelva University) for field sampling assistance. We also wish to thank two anonymous reviewers whose constructive comments have greatly improved the manuscript.

REFERENCES

Acero P, Ayora C, Carrera J (2007) Coupled thermal, hydraulic and geochemical evolution of pyritic tailings in unsaturated column experiments. Geochim Cosmochim Acta71: 5325-5338

Acero P, Ayora C, Carrera J, Saaltink MW, Olivella S (2009) Multiphase flow and reactive transport model in vadose tailings. Appl Geochem 24:1238-1250

Alcalde J, Martí D, Calahorrano A, Marzán I, Ayarza P, Carbonell R, Juhlin C, Pérez-Estaún A (2013) Active seismic characterization experiments of the Hontomín research facility for geological storage of CO_2, Spain. Int J Greenh Gas Control 19:785-795

Amos RT, Mayer KU, Blowes DW, Ptacek CJ (2004) Reactive transport modeling of column experiments for the remediation of acid mine drainage. Env Sci Tech 38:3131-3138

Appelo CAJ, Parkhurst, DL, Post, VEA (2014) Equations for calculating hydrogeochemical reactions of minerals and gases such as CO_2 at high pressures and temperatures. Geochim Cosmochim Acta 125:49-67

Arvidson RS, Ertan IE, Amonette JE, Luttge A (2003) Variation in calcite dissolution rates: A fundamental problem? Geochim Cosmochim Acta 67:1623-1634

Ayora C, Caraballo MA, Macias F, Rötting T, Carrera J, Nieto JM (2013) Acid mine drainage in the Iberian Pyrite Belt: 2. Lessons learned from recent passive remediation experiences. Environ Sci Pollut Res 20:7837-7853

Ayora C, Macías F, Torres E, Lozano A, Carrero S, Nieto JM, Perez-Lopez R, Fernandez-Martínez A, Castillo-Michel H (2016) Recovery of Rare Earth Elements and Yttrium from Passive-Remediation Systems of Acid Mine Drainage. Environ Sci Technol 50: 8255-8262

Bachu S, Gunter WD, Perkins EH (1994) Aquifer disposal of CO_2: hydrodynamic and mineral trapping. Energy Convers Mgmt 35:269-279

Balashov VN, Guthrie GD, Hakala JA, Lopano CL, Rinstidt JD, Brantley SL (2013) Predictive modeling of CO_2 sequestration in deep saline sandstone reservoirs: Impacts of geochemical kinetics. Appl Geochem 30:41-56

Bandstra JZ, Buss HL, Campen RK, Liermann LJ, Moore J, Hausrath EM, Navarre-Sitchler, AK, Jang J-H, Brantley SL(2008) Appendix: Compilation of Mineral Dissolution Rates. Kinetics of Water Rock Interactions. Brantley SL, Kubicki JD, White AF (eds) Springer, p 737-823

Beckingham LE, Steefel CI, Swift AM, Voltolini M, Yang L, Anovitz LM, Sheets JM, Cole DR, Kneafsey TJ, Mitnick EH, Zhang S, Landrot G, Ajo-Franklin JB, DePaolo DJ, Mito S, and Xue Z (2017) Evaluation of accessible mineral surface areas for improved prediction of mineral reaction rates in porous media. Geochim Cosmochim Acta 205:31-49

Beckingham LE, Mitnick EH, Steefel CI, Zhang S, Voltolini M, Swift AM, Yang L, Cole DR, Sheets JM, Ajo-Franklin JB, DePaolo DJ, Mito S, Xue Z (2016) Evaluation of mineral reactive surface area estimates for prediction of reactivity of a multi-mineral sediment. Geochim Cosmochim Acta 188:310-329

Benson SM, Cole DR (2008) CO_2 sequestration in deep sedimentary formations. Elements 4:325–331

Bibi I, Singh B, Silvester E (2011) Dissolution of illite in saline–acidic solutions at 25°C. Geochim Cosmochim Acta 75:3237-3249

Bigham JM, Schwertmann U, Traina SJ, Winland RL, Wolf M (1996) Schwermannite and the chemical modelling of iron in acid sulphate waters. Geochim Cosmochim Acta 60:2111-2121

Black JR, Haese, RR (2014) Chlorite dissolution rates under CO2 saturated conditions at 50 to 120 °C and 120 to 200 bar CO_2. Geochim Cosmochim Acta 125:225-240

Black JR, Carroll SA, Haese RR (2015) Rates of mineral dissolution under CO_2 storage conditions. Chem Geol 399:134-144

Booth J, Compton RG, Prout K, Payne RM (1997) Gypsum overgrowths passivate calcite to acid attack. J Colloid Interf Sci 192:207-214

Brookfield AE, Blowes DW, Mayer KU (2006) Integration of field measurements and reactive transport modelling to evaluate. J Cont Hydrol 88: 1-22

Bullard JW, Enjolras E, George WL, Satterfield SG, Terrill JE (2010) A parallel reaction-transport model applied to cement hydration and microstructure development. Model Simul Mater Sci Eng 18:025007

Canal J, Delgado J, Falcón I, Yang Q, Juncosa R, Barrientos V (2013) Injection of CO_2-saturated water through a siliceous sandstone plug from the Hontomin test site (Spain): experiment and modeling. Environ Sci Technol 47:159-167

Cappelli Ch, Yokoyama S, Cama J, Huertas FJ (2018) Montmorillonite dissolution kinetics: Experimental and reactive transport modelling interpretation. Geochim Chosmochim Acta 227:96-122

Caraballo MA, Macías F, Castillo J, Quispe D, Nieto JM, Ayora C (2011) Hydrochemical performance and mineralogical evolution of a dispersed alkaline substrate (DAS) remediating the highly polluted acid mine drainage in the full scale passive treatment of Mina Esperanza (SW, Spain). Am Mineral 96:1270–1277

Caraballo MA, Rötting TS, Macías F, Nieto JM, Ayora C (2009a) Field multi-step calcite and MgO passive system to treat acid mine drainage with high metal concentration. Appl Geochem 24:2301–11

Caraballo MA, Rotting TS, Nieto JM, Ayora C (2009b) Sequential extraction and DXRD applicability to poorly crystalline Fe- and Al-phase characterization from an acid mine water passive remediation system. Am Min, 94: 1029-1038

Carroll SA, Carey JW, Dzombak S, Huerta NJ, Li L, Richard T, Um W, Walsh SDC, Zhang L (2016) Review: Role of chemistry, mechanics and transport on well integrity in CO_2 storage environments. Int J Greenh Gas Cont 49:149-160

Carroll SA, Hao Y, Smith MM, Sholokhova Y (2013) Development of scaling parameters to describe CO_2-rock interactions within Weyburn-Midale flow units. Int J Greenh Gas Cont 16:S185-S195

Carroll SA, McNab WW, Torres SC (2011) Experimental study of cement-sandstone/shale-brine-CO_2 interactions. Geochem Trans 12:1-19

Chen L, Kang Q, Viswanathan HS, Tao W, (2014) Pore-scale study of dissolution-induced changes in hydrologic properties of rocks with binary minerals. Water Resour Res 50:9343-9365

Dai Z, Viswanathan H, Xiao T, Hakala A, Lopano C, Guthrie G, McPherson B (2019) Reactive transport modeling of geological carbon storage associated with CO_2 and brine leakage. *In*: Science of carbon storage in deep saline formations. Neweell P, Ilgen AG (eds) Elsevier, p 67-86

Daval D, Martinez I, Corvisier J, Findling N, Goffé B, Guyot F (2009) Carbonation of Ca-bearing silicates, the case of wollastonite: Experimental investigations and kinetic modeling. Chem Geol 265:63-78.

Dávila G, Luquot L, Soler JM, Cama J (2016a) Interaction between a fractured marl caprock and CO_2-rich sulfate solution under supercritical CO_2 conditions. Int J Greenh Gas Control 48:105-119

Dávila G, Luquot L, Cama J Soler JM (2016b) 2D reactive transport modeling of the interaction between a marl and a CO_2-rich sulfate solution under supercritical CO_2 conditions. Int J Greenh Gas Control 54:145-149

Dávila G, Cama J, Luquot L, Soler JM, and Ayora C (2017) Experimental and modeling study of the interaction between a crushed marl caprock and CO_2-rich solutions under different pressures and temperatures. Chem Geol 448:26-42

De Gaspari F, Cabeza Y, Luquot L, Rötting T, Saaltink MW, Carrera J (2014) Reactivity of Hontomín carbonate rocks to acidic solution injection: reactive "push-pull" tracer tests results. EGU General Assembly, id.16788

Deng H, Spycher N (2019) Modeling reactive transport processes in fractures. Rev Mineral Geochem 85:??-??.

Deng H, Molins S, Steefel C, DePaolo D, Voltolini M, Yang L, Ajo-Franklin J (2016) A 2.5D reactive transport model for fracture alteration simulation. Environ Sci Technol 50:7564-7571

Deng H, Molins S, Trebotich D, Steefel CI, DePaolo D (2018) Pore-scale numerical investigation of the impacts of surface roughness: Upscaling of reaction rates in rough fractures. Geochim Cosmochim Acta 239:374-389

Dilnesa BZ, Lothenbach B, Renaudin G, Wichser A, Kulik D (2014) Synthesis and characterization of hydrogarnet $Ca_3(Al_xFe_{1-x})_2(SiO_4)_y(OH)_{4(3-y)}$. Cement Concr Res 59:96-211

Dilnesa BZ, Lothenbach B, Renaudin G, Wichser A, Wieland E (2012) Stability of Monosulfate in the Presence of Iron. J Am Cer Soc 95:3305-3316

Dilnesa BZ, Lothenbach B, Le Saoût G, Renaudin G, Mesbah A, Filinchuk Y, Wichser A, Wieland E. Iron in carbonate containing AFm phases. Cement Concr Res 41:311-323

Domènech C, Ayora C, De Pablo J (2002) Oxidative dissolution of pyritic sludge from the Aznalcóllar mine (SW Spain). Chem Geol 190:339-353

Domenico PA, Schwartz FW (1990) Physical and Chemical Hydrogeology. John Wiley and Sons, New York

Duan Z, Sun R (2003) An improved model calculating CO_2 solubility in pure water and aqueous NaCl solutions from 273 to 533 K and from 0 to 2000 bar. Chem Geol 193:257-271

Elkhoury JE, Ameli P, Detwiler RL (2013) Dissolution and deformation in fractured carbonates caused by flow of CO_2-rich brine under reservoir conditions. Int J Greenh Gas Control 16: S203-S215

Fukushi K, Sato T, Yanase N (2003) Solid-solution reactions in As(V) sorption by schwertmannite Environ Sci Technol 37: 3581-3586

García-Rios M, Cama J, Luquot L, Soler JM (2014) Interaction between CO_2-rich sulfate solutions and carbonate reservoir rocks from atmospheric to supercritical CO_2 conditions: experiments and modeling. Chem Geol 383:107-122

García-Rios M, Luquot L, Soler JM, Cama J (2015) Influence of the flow rate on dissolution and precipitation features during percolation of CO2-rich sulfate solutions through fractured limestone samples. Chem Geol 414:95-108

García-Rios M, Luquot L, Soler JM, Cama J (2017) The role of mineral heterogeneity on the hydrogeochemical response of two fractured reservoir rocks in contact with dissolved CO_2. Appl Geochem 84:202-217

Gaus I, Azaroual M, Czernichowski-Lauriol I (2005) Reactive transport modelling of the impact of CO_2 injection on the clayey caprock at Sleipner (North Sea). Chem Geol 217:319-337

Gíslason SR, Sigurdardóttir H, Aradóttir ES, Oelkers EH (2018) A brief history of CarbFix: Challenges and victories of the project's pilot phase. Energy Procedia 146:103-114

Golfier F, Zarcone C, Bazin B, Lenormand R, Lasseux D, Quintard M (2002) On the ability of a Darcy-scale model to capture wormhole formation during the dissolution of a porous medium. J Fluid Mech 457:213-254.

Gouze P, Luquot L (2011) X-ray microtomography characterization of porosity, permeability and reactive surface changes during dissolution. J Contam Hydrol 120-121: 45-55

Gunter WD, Perkins E (1993) Aquifer disposal of CO_2-rich gases: reaction design for added capacity. Energy Convers Mgmt 34:941-948

Hamer M, Graham RC, Amrhein C, Bozhilov KN (2003) Dissolution of Ripidolite (Mg, Fe-Chlorite) in Organic and Inorganic Acid Solutions. Soil Sci Soc Am J 67:654-661

Hao Y, Smith MM, Sholokhova Y, Carroll SA (2013) CO_2-induced dissolution of low permeability carbonates. Part II: Numerical modeling of experiments. Adv Water Resour 62:388-408

Harrison AL, Dipple GM, Power IM, Mayer U (2015) Influence of surface passivation and water content on mineral reactions in unsaturated porous media: Implications for brucite carbonation and CO_2 sequestration. Geochim Cosmochim Acta 148:477-495

Hellmann R, Daval D, Tisserand D (2010) The dependence of albite feldspar dissolution kinetics on fluid saturation state at acid and basic pH: Progress towards a universal relation. C R Geosci 342:676-684

Hummel W, Berner U, Curti E, Pearson FJ, Thoenen T (2002) Nagra/PSI chemical thermodynamic data base 01/01. Radioch Acta 90:805-813

Iyer J, Walsh SDC, HaoY, Carroll SA (2017) Incorporating reaction-rate dependence in reaction-front models of wellbore-cement/carbonated-brine systems. Int J Greenh Gas Con 59:160-171

Kampman N, Bertier P, Busch A, Snippe J, Harrington J, PipichV, Maskell A, Bickle M (2017) Validating reactive transport models of CO2-brine-rock reactions in caprocks using observations from a natural CO_2 reservoir. Energy Procedia 114:4902-4916

Kang Q, Chen L, Valocchi AJ, Viswanathan HS (2014) Pore-scale study of dissolution induced changes in permeability and porosity of porous media. J Hydrol 517:1049-1055.

Kharaka YK, Cole DR, Thordsen JJ, Gans KD, Thomas BR (2013) Geochemical monitoring for potential environmental impacts of geologic sequestration of CO_2. Rev Min Geochem 77:399-430

Knauss KG, Johnson JW, Steefel CI (2005) Evaluation of the impact of CO_2, co-contaminant gas, aqueous fluid and reservoir rock interactions on the geologic sequestration of CO_2. Chem Geol 217:339-350

Kulik DA, Kersten M (2001) Aqueous solubility diagrams for cementitious waste stabilization systems: II, end-member stoichiometries of ideal calcium silicate hydrates solid solutions. J Am Cer Soc 84:3017-3026

Lai P, Moulton K, Krevor S (2015) Pore-scale heterogeneity in the mineral distribution and reactive surface area of porous rocks. Chem Geol 411:260-273

Loring JS, Miller QRS, Thompson CJ, Schaef HT (2019) Experimental studies of reactivity and transformations of rocks and minerals in water-bearing supercritical CO_2. *In*: Science of carbon storage in deep saline formations. Neweell P, Ilgen AG (eds) Elsevier p 47-65

Lothenbach B, Matschei T, Möschner G, Glasser FP (2008) Thermodynamic modelling of the effect of temperature on the hydration and porosity of Portland cement. Cement Concr Res 38:1-18

Lozano A, Fernández-Martínez A, Ayora C, Poulain A (2018) Local structure and ageing of basaluminite at different pH values and sulphate concentrations Chem Geol 496:25-33

Luhmann AJ, Kong, XZ, Tutolo, BM, Garapati N, Bagley BC, Saar MO, Seyfried Jr, WE (2014) Experimental dissolution of dolomite by CO_2-charged brine at 100 ºC and 150 bar: evolution of porosity, permeability, and reactive surface area. Chem Geol 380:145-160

Luhmann AJ, Tutolo, BM, Chunyang T, Moskowitz BM, Saar MO, Seyfried Jr, WE (2017) Whole rock basalt alteration from CO2-rich brine during flow-through experiments at 150 °C and 150 bar. Chem. Geol. 453:92-110

Luquot L, Andreani M, Gouze P, Camps P (2012) CO_2 percolation experiment through chlorite/zeolite-rich sandstone (Pretty Hill Formation – Otway Basin–Australia). Chem Geol 294-295:75-88

Luquot L, Gouze P (2009) Experimental determination of porosity and permeability changes induced by injection of CO_2 into carbonate rocks. Chem Geol 265:148-159

Luquot L, Gouze P, Niemi A, Bensabat J, Carrera J (2016) CO_2-rich brine percolation experiments through Heletz reservoir rock samples (Israel): Role of the flow rate and brine composition. Int J Greenh Gas Control 48:44-58

Luquot L, Rodriguez O, Gouze P (2014) Experimental Characterization of Porosity Structure Undergoing Different Dissolution Regimes. Transp Porous Media 101:507-532

Luttge A, Arvidson RS, Fischer C, Kurganskaya I (2019) Kinetic concepts for quantitative prediction of fluid-solid interactions. Chem Geol 504:216-235

Macías F, Caraballo MA, Rotting TS, Perez-Lopez R, Nieto JM, Ayora C (2012) From highly polluted Zn-rich acid mine drainage to non-metallic waters: Implementation of a multi-step alkaline passive treatment system to remediate metal pollution. Sci Total Environ 433:323-330

Malmstrom ME, Berglund S, Jarsjo J (2008) Combined effects of spatially variable flow and mineralogy on the attenuation of acid mine drainage in groundwater. Appl Geochem 23:1419-1436

Marty NCM, Cama J, Sato T, Chino D, Villiéras F, Razafitianamaharavo A, Brendlé J, Giffaut E, Soler JM, Gaucher EC, Tournassat C (2011) Dissolution kinetics of synthetic Na-smectite. An integrated experimental approach. Geochim Cosmochim Acta 75:5849-5864

Matschei T, Lothenbach B, Glasser FP (2007) Thermodynamic properties of Portland cement hydrates in the system $CaO–Al_2O_3–SiO_2–CaSO_4–CaCO_3–H_2O$. Cement Concr Res 37:1379-1410

Mayer KU, Frind EO, Blowes DW (2002) Multicomponent reactive transport modeling in variably saturated porous media using a generalized formulation for kinetically controlled reactions. Water Resour Res 38:1-21

Mayer KU, Benner SG, Blowes DW (2006) Process-based reactive transport modeling of a permeable reactive barrier for the treatment of mine drainage. J Cont Hydro 85:195-211

Mbia EN, Frykman P, Nielsen C, Fabricius I, Pickup GE, Bernstone C (2014) Caprock compressibility and permeability and the consequences for pressure development in CO_2 storage sites. Int J Greenh Gas Con 22: 139-153.

Menke HP, Andrew MG, Blunt MJ, Bijeljic B (2016) Reservoir condition imaging of reactive transport in heterogeneous carbonates using fast synchrotron tomography – Effect of initial pore structure and flow conditions. Chem Geol 428:15-26

Molins S (2015) Reactive interfaces in direct numerical simulation of pore-scale processes. Rev Min Geochem 80:461-481

Molins (2019) Multiscale reactive transport approaches. Rev Mineral Geochem 85:??- ??

Myers RJ, L'Hopital E, Provis JL, Lothenbach B (2015) Effect of temperature and aluminium on calcium (alumino)silicate hydrate chemistry under equilibrium conditions. Cem Con Res 68:83-93.

Noiriel C (2015) Resolving time-dependent evolution of pore-scale structure, permeability and reactivity using X-ray microtomography. Rev Mineral Geochem 80:247-285

Noiriel C, Gouze P, Madé B (2013) 3D analysis of geometry and flow changes in a limestone fracture during dissolution. J Hydrol 486:211-223

Noiriel C, Luquot L, Madé B, Raimbault L, Gouze P, van der Lee J (2009). Changes in reactive surface area during limestone dissolution: An experimental and modeling study. Chem Geol 265:160-170

Noiriel C, Madé B, Gouze P (2007) Impact of coating development on the hydraulic and transport properties in argillaceous limestone fracture. Water Resour Res 43, W09406

Noiriel C, Steefel C, Yang L, Bernard D (2015) Effects of pore-scale precipitation on permeability and flow. Adv Water Resour 95:125-137

Nordstrom DK, Alpers CN (1999) Geochemistry of acid mine waters. In: Plumlee, G.S., Logsdon, M.J. (Eds.), Reviews in Economic Geology, vol. 6A. The Environmental Geochemistry of Mineral Deposits. Part A. Processes, Methods and Health Issues. Soc. Econ. Geol., Littleton, CO, p. 133–160

Nordstrom DK, Alpers CN, Ptacek CJ, Blowes DW (2000) Negative pH and Extremely Acidic Mine Waters from Iron Mountain, California. Environ Sci Technol 34:254-258

Offeddu FG, Cama J, Soler JM, Dávila G, McDowell A, Craciunescu T, Tiseanu I (2015) Processes affecting the efficiency of limestone in passive treatments for AMD: Column experiments. J Environ Chem Eng 3, 304-316

Offedu FG, Cama J, Soler JM, Putnis CV (2014) Direct nanoscale observations of the coupled dissolution of calcite and dolomite and the precipitation of gypsum. Beilstein J. Nanotechnol. 5:1245-1253

Oliva J, De Pablo J, Cortina JL, Cama J, Ayora C (2010) The use of Apatite II (TM) to remove divalent metal ions zinc(II), lead(II), manganese(II) and iron(II) from water in passive treatment systems: Column experiments. J Hazar Mat 184:364-37

Orden S, Macías F, Nieto JM, Ayora C (2018) Tratamiento sostenible de drenaje ácido de mina: Tecnología DAS-calizo en Mina Esperanza (Faja Pirítica Ibérica). Macla 23, *http://www.ehu.eus/sem/revista/macla.htm*

Pabst T, Bussiere B, Aubertin M, Molson J (2018) Comparative performance of cover systems to prevent acid mine drainage from pre-oxidized tailings: A numerical hydro-geochemical assessment. J Cont Hydrol 214:39-53

Pabst T, Molson J, Aubertin M, Bussiere B (2017) Reactive transport modelling of the hydro-geochemical behaviour of partially oxidized acid-generating mine tailings with a monolayer cover. Appl Geochem 78:219-233

Palandri JL, Kharaka YK (2004) A compilation of rate parameters of water-mineral interaction kinetics for application to geochemical modeling. U.S. Geological Survey

Parkhurst DL, Appelo CAJ, (2013) Description of input and examples for PHREEQC (Version 3)-a computer program for speciation, batch-reaction, one-dimensional transport, and inverse geochemical calculations. U.S. Geological Survey Techniques and methods report. Book 6, 49

Pedretti D, Mayer KU, Beckie RD (2017) Stochastic multicomponent reactive transport analysis of low quality drainage release from waste rock piles: Controls of the spatial distribution of acid generating and neutralizing minerals. J Cont Hydrol 201:30-38

Pérez-Lopez R, Cama J, Nieto JM, Ayora C (2007) The iron-coating role on the oxidation kinetics of a pyritic sludge doped with fly ash. Geochim Cosmochim Acta 71:1921-1934

Pérez-Lopez R, Cama J, Nieto JM, Ayora C, Saaltink MW (2009) Attenuation of pyrite oxidation with a fly ash pre-barrier: Reactive transport modelling of column experiments. Appl Geochem 24:1712-1723

Pérez-López R, Macías F, Caraballo MA, Nieto JM, Román-Ross G, Tucoulou R, Ayora C (2011) Mineralogy and geochemistry of Zn-rich mine-drainage precipitates from an MgO passive treatment system by synchrotron-based X-ray analysis. Environ Sci Technol 45:7826-7833

Pokrovsky OS, Golubev SV, Schott J (2005) Dissolution kinetics of calcite, dolomite and magnesite at 25 °C and 0 to 50 atm pCO_2. Chem Geol 217:239-255

Pokrovsky OS, Golubev SV, Schott J, Castillo A (2009) Calcite, dolomite and magnesite dissolution kinetics in aqueous solutions at acid to circumneutral pH, 25 to 150 °C and 1 to 55 atm pCO_2: New constraints on CO_2 sequestration in sedimentary basins. Chem Geol 265:20-32

Revil A, Cathles III LM (1999) Permeability of shaly sands. Water Resour Res 35:651-662

Rohmer J, Pluymakers A, Renard F (2016) Mechano-chemical interactions in sedimentary rocks in the context of CO2 storage: Weak acid, weak effects? Earth Sci Rev 157:86-110

Rotting TS, Thomas RC, Ayora C, Carrera J (2008a): Passive treatment of acid mine drainage with high metal concentrations using dispersed alkaline substrate. J Envir Quality 37:1741-1751

Rötting TS, Caraballo MA, Serrano JA, Ayora C, Carrera J (2008b) Field application of calcite Dispersed Alkaline Substrate (calcite-DAS) for passive treatment of acid mine drainage with high Al and metal concentrations. Appl Geochem 23:1660-1674

Rötting TS, Ayora C, Carrera J (2008c) Improved passive treatment of high Zn and Mn concentrations using Caustic Magnesia (MgO): Particle size effects. Environ Sci Technol 24:9370-9377

Saaltink MW, Batlle F, Ayora C, Carrera J, Olivella S (2004) RETRASO, a code for modeling reactive transport in saturated and unsaturated porous media. Geol Acta 2:235–251

Salmon SU, Malmstrom ME (2004) Geochemical processes in mill tailings deposits: modelling of groundwater composition. Appl Geochem 19:1-17

Saaltink MW, Batlle F, Ayora C, Carrera J, Olivella S (2004) RETRASO, a code for modeling reactive transport in saturated and unsaturated porous media. Geol Acta 2:235-251

Samson E, Marchand J (2003) Calculation of ionic diffusion coefficients on the basis of migration test results. Mater Structu 36:156-165

Schmidt T, Lothenbach B, Romer M, Scrivener K, Rentsch D, Figi R (2008) A thermodynamic and experimental study of the conditions of thaumasite formation. Cement Concr Res 38:337-349

Sjöberg EL, Rickard DT (1984). Temperature-dependence of calcite dissolution kinetics between 1º C and 62 ºC at pH 2.7 to 8.4 in aqueous-solutions. Geochim Cosmochim Acta 48:485-493

Smith MM, Hao Y, Carroll SA (2017) Development and calibration of a reactive transport model for carbonate reservoir porosity and permeability changes based on CO_2 core-flood experiments. Int. J. Greenh. Gas Cont. 57, 73-88

Smith MM, Sholokhova Y, Hao Y, Carroll SA (2013a) CO_2-induced dissolution of low permeability carbonates. Part I: Characterization and experiments. Adv Water Resour 62:370-387

Smith MM, Wolery TJ, Carroll, SA (2013b) Kinetics of chlorite dissolution at elevated temperatures and CO_2 conditions. Chem Geol 347:1-8

Snæbjörnsdóttir SO, Oelkers EH, Mesfin K, Aradóttir ES, Dideriksen K, Gunnarsson I, Gunnlaugsson E, Matter JM, Stute M, Gislason SR (2017) The chemistry and saturation states of subsurface fluids during the in situ mineralisation of CO_2 and H_2S at the CarbFix site in SW-Iceland. Int J Greenh Gas Con 58:87-102.

Soler JM, Boi M, Mogollon J, Cama J, Ayora C, Nico P (2008) The passivation of calcite by acid mine water. Column experiments with ferric sulfate and ferric chloride solutions at pH 2. Appl Geochem 23:3579-3588

Soler JM, Mäder KU (2010) Cement-rock interaction: Infiltration of a high-pH solution into a fractured granite core. Geo Acta 3:221-233

Soler JM, Vuorio M. Hautojärvi A (2011) Reactive transport modeling of the interaction between water and a cementitious grout in a fractured rock. Application to ONKALO (Finland). Appl Geochem 26:1115-1129

Soler-Sagarra J, Luquot L, Martínez-Pérez L, Saaltink MW, De Gaspari F, Carrera J (2016) Simulation of chemical reaction localization using a multiporosity reactive transport approach. Int J Greenh Gas Control 48:59-68

Steefel CI, Appelo CAJ, Arora B, Jacques D, Kalbacher T, Kolditz O, Lagneau V, Lichtner P C, Mayer KU, Meeussen JCL, Molins S, Moulton D, Shao H, Simunek J, Spycher N, Yabusaki SB and Yeh GT (2015a) Reactive transport codes for subsurface environmental simulation. Comput Geosci 19:445-495

Steefel CI, Beckingham LE, Landrot G (2015b) Micro-Continuum Approaches for Modeling Pore-Scale Geochemical Processes. Revs Mineral Geochem 80: 217-246

Steefel CI, DePaolo DJ, Lichtner PC (2005) Reactive transport modeling: an essential tool and a new research approach for the Earth sciences. Earth Planet Sci Lett 240:539-558

Szymczak P, Ladd AJC (2009) Wormhole formation in dissolving fractures. J Geophys Res 114:B06203

Szymczak P, Ladd AJC, (2011) The initial stages of cave formation: beyond the one dimensional paradigm. Earth Planet Sci Lett 301:424-432

Thaysen EM, Soler JM, Boone M, Cnudde V, Cama J (2017) Effect of dissolved H_2SO_4 on the interaction between CO_2-rich brine solutions and limestone, sandstone and marl. Chem Geol 450:31-43

Torres E, Lozano A, Macias F, Gomez-Arias A, Castillo J, Ayora C (2018) Passive elimination of sulfate and metals from acid mine drainage using combined limestone and barium carbonate systems. J Cleaner Produc 182:114-123

Trapote-Barreira A, Cama J, Soler JM (2014) Dissolution kinetics of C–S–H gel. Flow-through experiments. Phys Chem Earth 70-71:17-31

Trapote-Barreira A, Cama J, Soler JM, Lothenbach B (2016) Degradation of mortar under advective flow: column experiments and reactive transport modeling. Cem Conc Res 81:81-93

Tutolo BM, Luhmann AJ, Kong XZ, Saar MO, Seyfried Jr WE (2015a) CO_2 sequestration in feldspar-rich sandstone: Coupled evolution of fluid chemistry,mineral reaction rates, and hydrogeochemical properties. Geochim Cosmochim Acta 160:132-154

Tutolo BM, Kong XZ, Seyfried Jr WE, Saar MO (2015b) High performance reactive transport simulations examining the effects of thermal, hydraulic, and chemical (THC) gradients on fluid injectivity at carbonate CCUS reservoir scales. Int J Greenh Gas Con 39:285-301

Vilarrasa V, Makhnenko RY Rutquist J (2019) Field and laboratory studies of geomechanical response to the injection of CO_2. *In*: Science of carbon storage in deep saline formations. Neweell P, Ilgen AG (eds) Elsevier, p 159-178

Vuorinen TL, Laurila T (2005) Interfacial reactions between lead-free solders and common base materials. Mat Sci Eng 49:1-60

Walsh SDC, Mason EH, Du France WL, Carroll SA (2014) Experimental calibration of a numerical model describing the alteration of cement/caprock interfaces by carbonated brine. Int J Greenh Gas Con 22:176-188

Welch SA, Sheets JM, Place MC, Saltzman MR, Edwards CT, Gupta N, Cole DR (2019) Assessing geochemical reactions during CO_2 injection into an oil-bearing reef in the Northern Michigan basin. Appl. Geochem. 100:380-392

Wen H, Li L (2017) An upscaled rate law for magnesite dissolution in heterogeneous porous media. Geochim Cosmochim Acta 210:289-305

Wen H, Li L (2018) An upscaled rate law for mineral dissolution in heterogeneous media: The role of time and length scales. Geochim Cosmochim Acta 235:1-20

White AF, Brantley SL (2003) The effect of time on the weathering of silicate minerals: why do weathering rates differ in the laboratory and field? Chem Geol 202:479–506

Wolery TJ et al. (1990) Current status of the EQ3/6 software package for geochemical modeling. In: Chemical Modeling of Aqueous Systems II. Melchior C, Bassett RL (ed), American Chemical Society Symposium Series, p 104-116

Wolf JL, Niemi A, Bensabat J, Rebscher D (2016) Benefits and restrictions of 2D reactive transport simulations of CO_2 and SO_2 co-injection into a saline aquifer using TOUGHREACTV3.0-OMP. Int J Greenh Gas Con 54:610-626

Wunderly MD, Blowes DW, Frind EO, Ptacek CJ (1996) Sulfide mineral oxidation and subsequent reactive transport of oxidation products in mine tailings impoundments: A numerical model. Water Resour Res 32: 3173-3187

Xiao T, McPherson B, Esser R, Jia W, Moodie N, Chu S, Lee S-Y. (2019) Forecasting commercial-scale CO_2 storage capacity in deep saline reservoirs: Case study of Buzzard's bench, Central Utah. Com Geosci, doi: https://doi.org/10.1016/ j.cageo.2018.12.006

Xu J, Fan C, Teng, HH (2012) Calcite dissolution kinetics in view of Gibbs free energy, dislocation density, and pCO_2. Chem Geol 322-323:11-18

Xu T, Apps JA, Pruess K, Yamamoto H (2007) Numerical modeling of injection and mineral trapping of CO_2 with H_2S and SO_2 in sandstone formation. Chem Geol 242:319-346

Xu TF, White SP, Pruess K, Brimhall GH (2000) Modeling of pyrite oxidation in saturated and unsaturated subsurface flow systems. Trans Porous Med 39:25-56

Zhang S, Yang L, DePalolo DJ, Steefel CI (2015) Chemical affinity and pH effects on chlorite dissolution kinetics under geological CO_2 sequestration related conditions. Chem Geol 396:208-217

Zheng L, Spycher N, Birkholzer J, Xu T, Apps J, Kharaka Y (2013) On modeling the potential impacts of CO_2 sequestration on shallow groundwater: Transport of organics and co-injected H_2S by supercritical CO_2 to shallow aquifers. Int J Greenh Gas Con 14:113-127

FIGURE CAPTIONS

Figure 1. Schemes that show the laboratory experimental set-ups, different types of experiments and field treatment system: a) parts of the experimental set-ups for column and percolation experiments: CO_2 bottle and compressor, peristaltic or dual piston pump, reacting sample holder, solution collector and backpressure (elevated pressure); b) column experiments filled with rock fragments and rock/cement fragments in alternating layers (5 cm long and 2.5 cm in diameter; at the bottom and top, 5-mm layers of silica beads were placed to homogeneously distribute the solutions at the inlet and outlet; c) percolation experiments with fractured cores of 2 cm long and 0.8 cm in diameter (rock-rock halves) and 5 cm long and 2.5 cm in diameter (cement-rock halves); d) DAS mixtures of calcite sand and wood shavings columns (15 cm diameter x 50 cm length) with connecting piezometric standpipes to measuring ports; e) passive AMD-treatment system showing mine adit, aeration cascades, decantation ponds and DAS tank (see text).

Figure 2. Photographs of the limestone-DAS remediation system to treat AMD from abandoned Mina Esperanza (Iberian Pyrite Belt (IPB), south-western Spain). Numbers show sampling points in Figure 18.

Figure 3. Illustrations showing the conceptual models ((a) 1D for columns, (b) 2D for columns and (c) 2D for percolation experiments), implemented grids, and geometry and boundary conditions of the flow domains. Left and right boundaries are no-flow boundaries. Zone 0 represents mobile zone (saturated void space or fracture) and zones 1-5 represent non-mobile zone (fragments/rock).

Figure 4. Variations in the measured (symbols) and simulated (*Sim.*; lines) pH and concentrations in the output solutions: a) pH, b) ΔCa, c) ΔS, d) ΔSi and e) ΔFe with time in a representative marl experiment at 10 bar of pCO_2 and 25 ºC and 60 ºC. [Used by permission of Elsevier, from Dávila et al. (2017), *Chemical Geology*, Vol. 448:26-42].

Figure 5. SEM images of unreacted and reacted limestone (a and c, respectively) and dolostone samples (b and d, respectively). The unreacted limestone fragments show a rough surface in contrast to a flat and terraced surface of the unreacted dolostone fragments. Gypsum precipitated in the form of needles (see dimensions). [Used by permission of Elsevier, from García-Rios et al. (2014), *Chemical Geology*, Vol. 383:107-122].

Figure 6. Variation of increase in porosity, $\Delta\Phi\%$, along the normalized column length: a) limestone (pCO_2 = 10 bar; T = 25, 40 and 60 ºC); b) marl (pCO_2 = 10 bar; T = 25 and 60 ºC); c) limestone (atmospheric pressure and pCO_2 of 10 and 34 bar of pCO_2; T = 60 ºC). [Used by permission of Elsevier, from García-Rios et al. (2014), *Chemical Geology*, Vol. 383:107-122].

Figure 7. SEM images of (a) the rock layer 1 and (b) cement layer 2 displaying gypsum needles formed on calcite (limestone) surfaces and an aragonite rim coating a cement-fragment surface; rim thickness is about 100 μm.

Figure 8. Variation in (a) porosity and (b) calcite volumetric fraction with respect to normalized distance in the three rocks at the end of experiments. The flux flow is from mobile zone (acidic brine; grey band) to non-mobile zone (rock/cement fragments); see Fig. 3b).

Figure 9. (a) mCT images showing ramified wormhole through fracture and inlet to outlet cross-sections (limestone); (b-e) SEM images of altered fracture regions: (b) gypsum precipitates on dissolving calcite surface (limestone); (c) yellow circle shows a site of grain detachment along the fracture (sandstone); (d-e) altered porous zone along the fracture at 8 mm from the inlet (marl). In (b and c) *y* values indicate distance from the fracture inlet along the flow direction (*y*).

[Adapted from García-Rios M, Luquot L, Soler JM, Cama J (2017) The role of mineral heterogeneity on the hydrogeochemical response of two fractured reservoir rocks in contact with dissolved CO_2. *Applied Geochemistry*, Vol 84, 202-217, Fig. 4, with permission].

Figure 10. Variation of porosity along the distance to the fracture under 10 bar of pCO_2 in (a) limestone and (b) sandstone. *y* indicates distance from inlet (0 mm) to outlet (20 mm). [Adapted from García-Rios M, Luquot L, Soler JM, Cama J (2017) The role of mineral heterogeneity on the hydrogeochemical response of two fractured reservoir rocks in contact with dissolved CO_2. *Applied Geochemistry*, Vol 84, 202-217, Fig. 5, with permission].

Figure 11. Experimental and modeling results of the sandstone-cement column under atmospheric pressure: (a-f) pH and output concentrations vs. time; (g and h) variation in volumetric fraction of secondary minerals and porosity along the columns distance at the conclusion of the experiments.

Figure 12. (Top left) Photograph of a thin section along the Z axis of core sample (2.5 cm in diameter). AMD contact indicates AMD-upper-core contact. The brownish strip at the top formed during concrete degradation. Concrete clasts are calcite, dolomite and quartz. (Bottom) SEM images of thin section along the Z axis of core sample: left: degraded strip at the core-AMD contact suggests alteration of concrete; right: close-up and EDS analysis of the strip-concrete interface related to the presence of Fe-rich phases (schwertmannite), carbonate minerals (C, Ca, Mg), quartz (Si) and ettringite or gypsum (Al, Ca, S).

Figure 13. Calculated variation in (a) mineral volume fraction and (b) porosity along depth in a concrete core exposed to AMD. Alteration is calculated to take place at the top across the first 1.5 mm. AMD is represented in blue.

Figure 14. Four mCT images of the same section of a column during the experiment: d0, before reaction; d4, d8 and d12, after 4, 8 and 12 days (passivation at ≈ 300 h). Since the grains were not cemented, relative positions changed slightly in the four images. [Reprinted from Offeddu FG, Cama J, Soler JM, Dávila G, McDowell A, Craciunescu T, Tiseanu I (2015) Processes affecting the efficiency of limestone in passive treatments for AMD: Column experiments. *Journal of Environmental Chemical Engineering* , Vol 3, 304-316, Figs. 6, 7, with permission].

Figure 15. Experimental and modeling results (output concentrations vs. time) from representative column. [Reprinted from Offeddu FG, Cama J, Soler JM, Dávila G, McDowell A, Craciunescu T, Tiseanu I (2015) Processes affecting the efficiency of limestone in passive treatments for AMD: Column experiments. *Journal of Environmental Chemical Engineering* , Vol 3, 304-316, Fig. 13, with permission].

Figure 16. (a-d) Pore water composition of a limestone-DAS column treating an AMD sample (concentration in mM; symbols and lines represent experimental and modeling data, respectively; (e) calculated volumes of the main precipitates after 42 d (m^3_{min} m^{-3}_{column}); (f) photograph of the column after 24 d (sch = schwertmannite; bas = basaluminite and gypsum; cc = limestone).

Figure 17. Distribution of pH and porosity within a DAS-calcite system after 2 yr of treating 1 L s^{-1} of AMD (see text for composition). Results from two limestone-wood shavings ratios (2:1 and 1:1) in reactive filling.

Figure18. Evolution of the main chemical parameters of AMD through the remediation system of Mina Esperanza II after 32 months of treatment (Orden et al., 2018). Location of sampling points is shown in Figure 2.

Figure 19. Water chemistry evolution at the outlet of Mina Esperanza I treatment. Symbols represent experimental values, and solid and dotted lines are model predictions under less and more acidic inflow waters. [Reprinted from Ayora C, Caraballo MA, Macías F, Rötting T, Carrera J, Nieto JM (2013) Acid mine drainage in the Iberian Pyrite Belt: 2. Lessons learned from recent passive remediation experiences. *Environmental Science Pollution Research*, Vol 20, 7837-7853, Fig. 8, with permission].

Figure 20. Comparison between the experimental (a) and calculated (b) distribution of solid phases after 18 month of functioning of the Mina Esperanza treatment. Experimental values (Caraballo et al., 2011) consist of cumulative graphs for the concentration of the main constituents (Fe, Al, Ca, and S) obtained after each step of a sequential extraction. Step 1 = water soluble fraction, Step 2 = exchangeable fraction, Step 3 = poorly ordered oxy-hydroxides, Step 4 = ordered hydroxides and oxides. [Reprinted from Ayora C, Caraballo MA, Macías F, Rötting T, Carrera J, Nieto JM (2013) Acid mine drainage in the Iberian Pyrite Belt: 2. Lessons learned from recent passive remediation experiences. *Environmental Science Pollution Research*, Vol 20, 7837-7853, Fig. 9, with permission].

FIG. 1

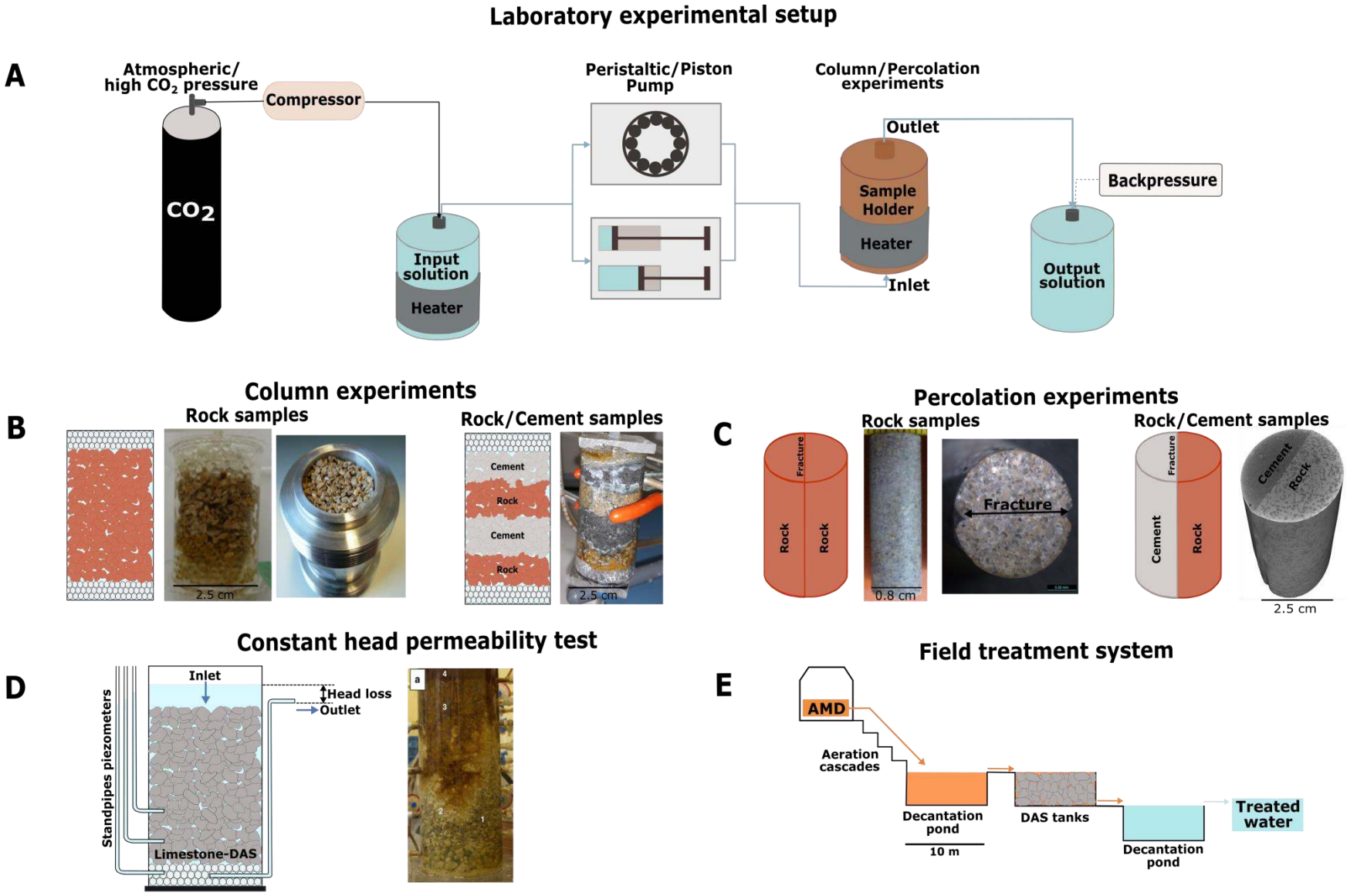
Laboratory experimental setup
A
Atmospheric/ high CO_2 pressure
Compressor
CO_2
Input solution
Heater
Peristaltic/Piston Pump
Column/Percolation experiments
Outlet
Sample Holder
Heater
Inlet
Backpressure
Output solution
B
Column experiments
Rock samples
2.5 cm
Rock/Cement samples
Cement
Rock
Cement
Rock
2.5 cm
C
Percolation experiments
Rock samples
Fracture
Rock
Rock
0.8 cm
Fracture
Rock/Cement samples
Fracture
Cement
Rock
Cement
Rock
2.5 cm
D
Constant head permeability test
Inlet
Head loss
Outlet
Standpipes piezometers
Limestone-DAS
a
4
3
2
1
E
Field treatment system
AMD
Aeration cascades
Decantation pond
10 m
DAS tanks
Decantation pond
Treated water

FIG. 2

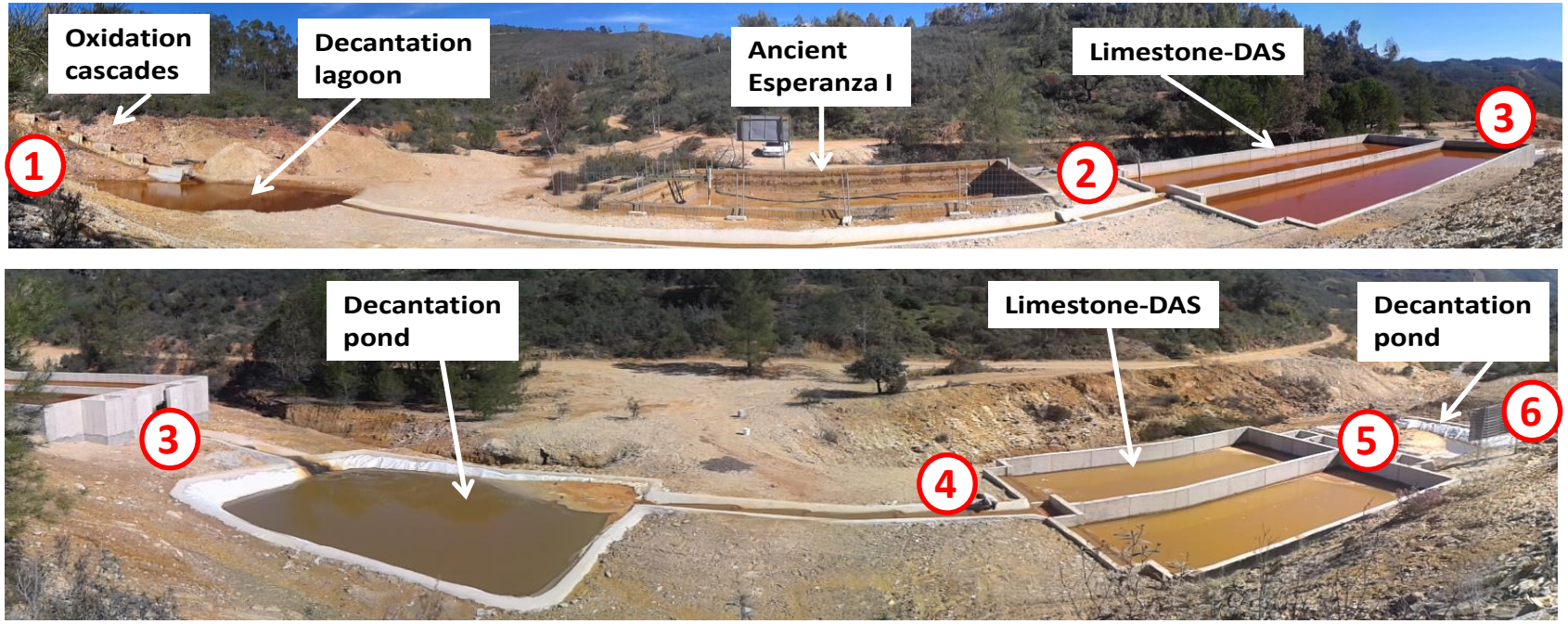
Oxidation cascades
Decantation lagoon
Ancient Esperanza I
Limestone-DAS
1
2
3
Decantation pond
Limestone-DAS
Decantation pond
3
4
5
6
10 m

FIG. 3

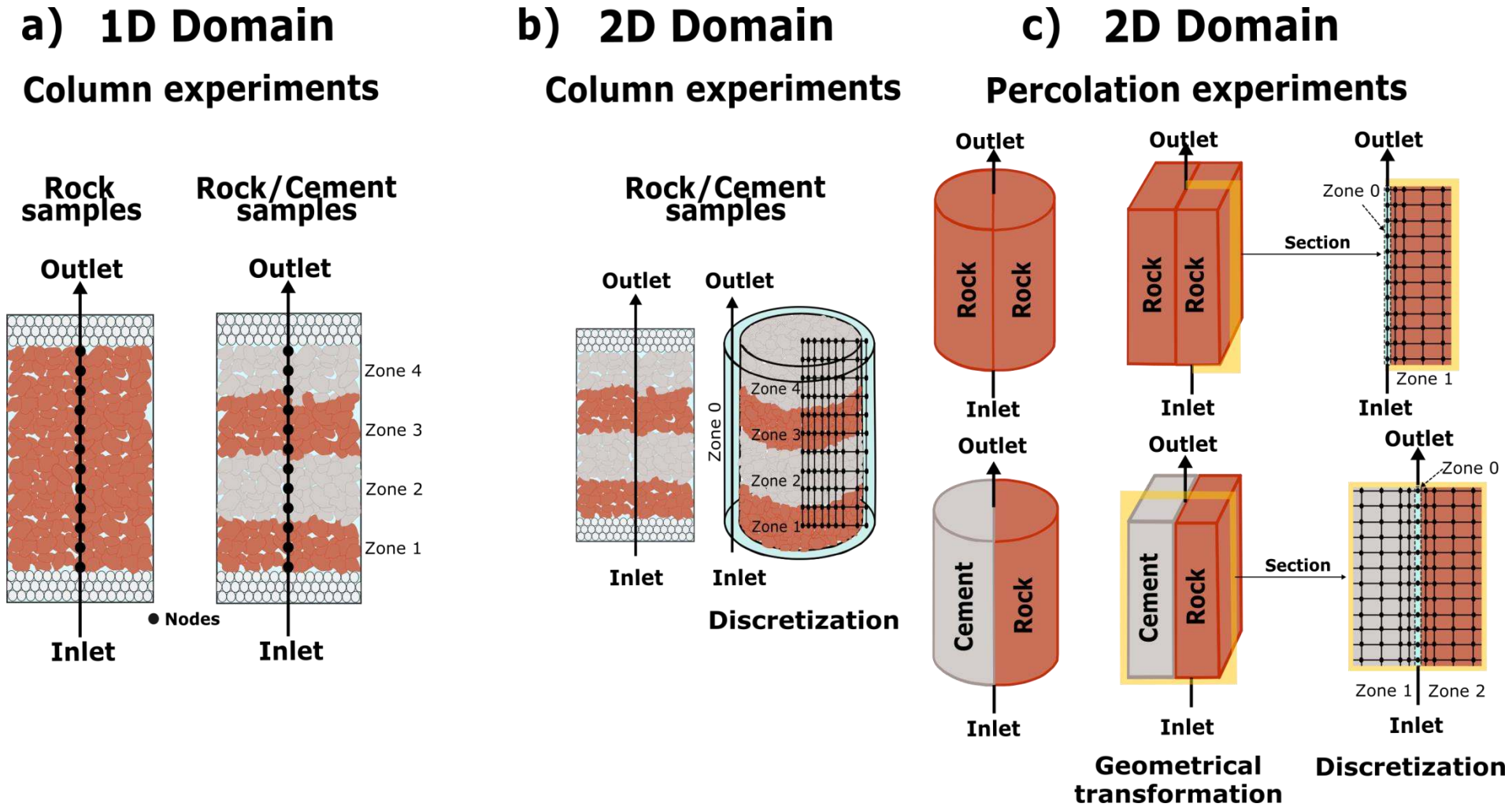
a) 1D Domain
Column experiments
Rock samples
Rock/Cement samples
Outlet
Outlet
Zone 4
Zone 3
Zone 2
Zone 1
Nodes
Inlet
Inlet
b) 2D Domain
Column experiments
Rock/Cement samples
Outlet
Outlet
Zone 0
Zone 4
Zone 3
Zone 2
Zone 1
Inlet
Inlet
Discretization
c) 2D Domain
Percolation experiments
Outlet
Rock
Rock
Inlet
Outlet
Rock
Rock
Inlet
Section
Outlet
Zone 0
Zone 1
Inlet
Outlet
Cement
Rock
Inlet
Outlet
Cement
Rock
Inlet
Geometrical transformation
Section
Outlet
Zone 0
Zone 1
Zone 2
Inlet
Discretization

FIG. 4

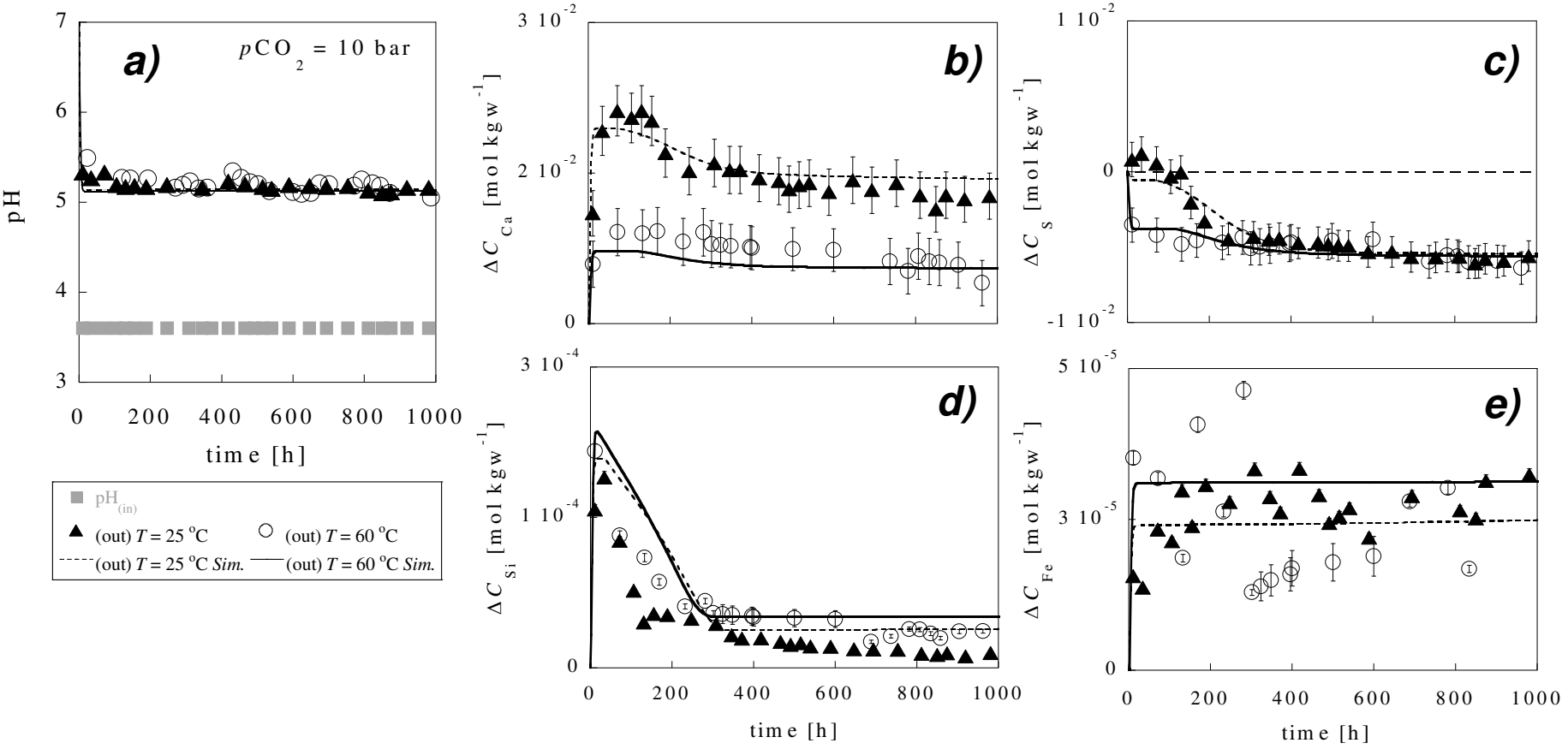
a)
pCO_2 = 10 bar
pH
time [h]
$pH_{(in)}$
(out) T = 25 °C
(out) T = 60 °C
(out) T = 25 °C Sim.
(out) T = 60 °C Sim.
b)
ΔC_{Ca} [mol kgw^{-1}]
c)
ΔC_S [mol kgw^{-1}]
d)
ΔC_{Si} [mol kgw^{-1}]
e)
ΔC_{Fe} [mol kgw^{-1}]

FIG. 5

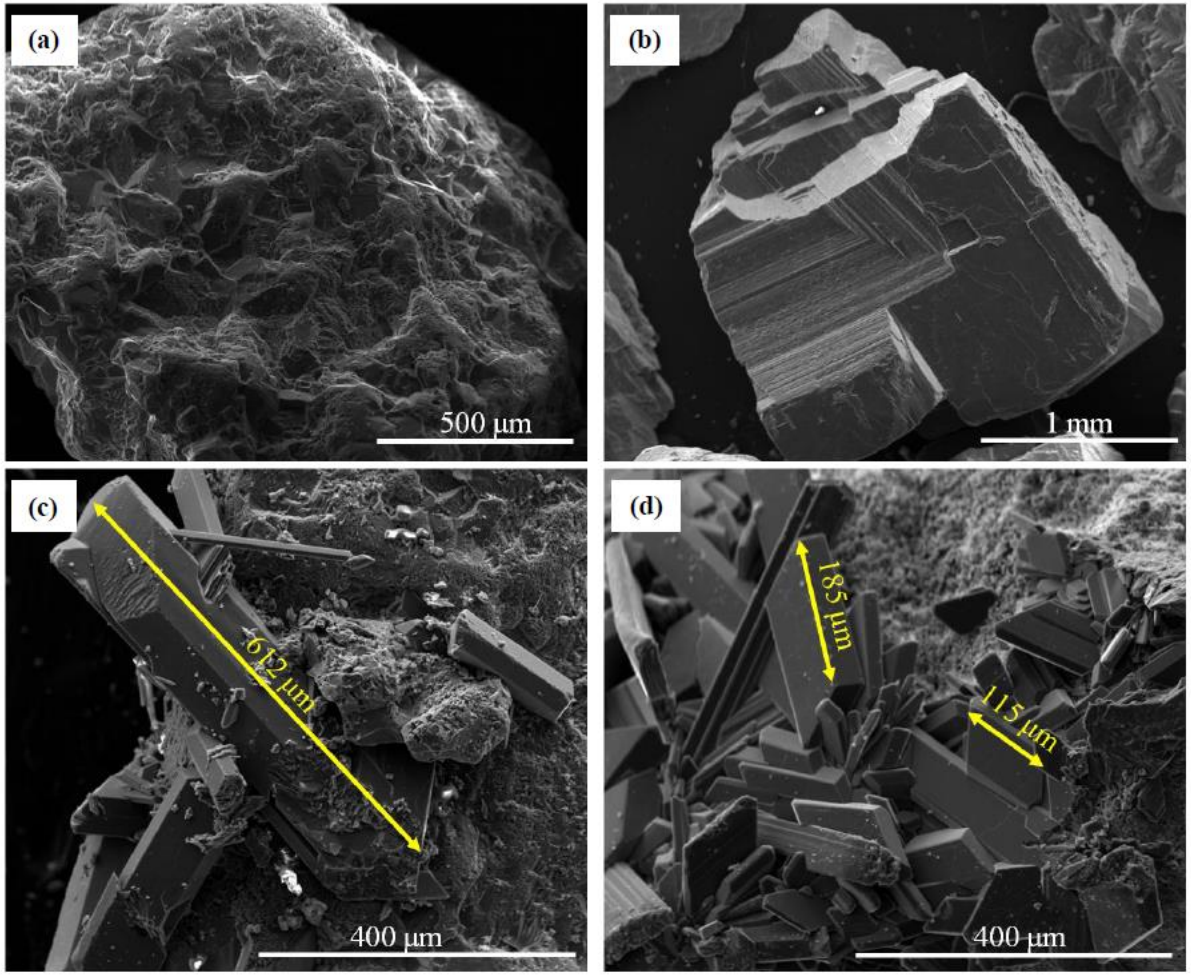

FIG. 6

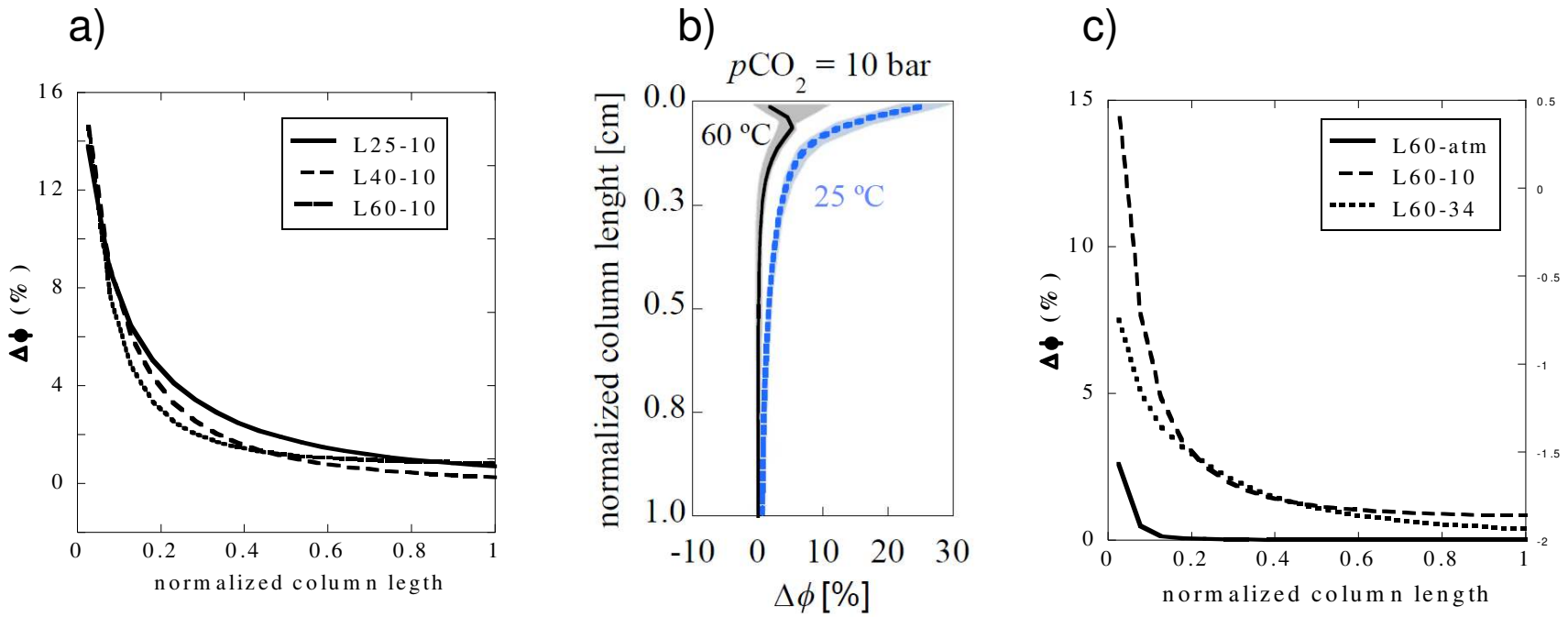
a)
16
12
8
4
0
Δϕ (%)
0
0.2
0.4
0.6
0.8
1
normalized column legth
L25-10
L40-10
L60-10
b)
pCO2 = 10 bar
0.0
0.3
0.5
0.8
1.0
normalized column lenght [cm]
60 °C
25 °C
-10
0
10
20
30
Δϕ [%]
c)
15
10
5
0
Δϕ (%)
0.5
0
-0.5
-1
-1.5
-2
0
0.2
0.4
0.6
0.8
1
normalized column length
L60-atm
L60-10
L60-34

FIG. 7

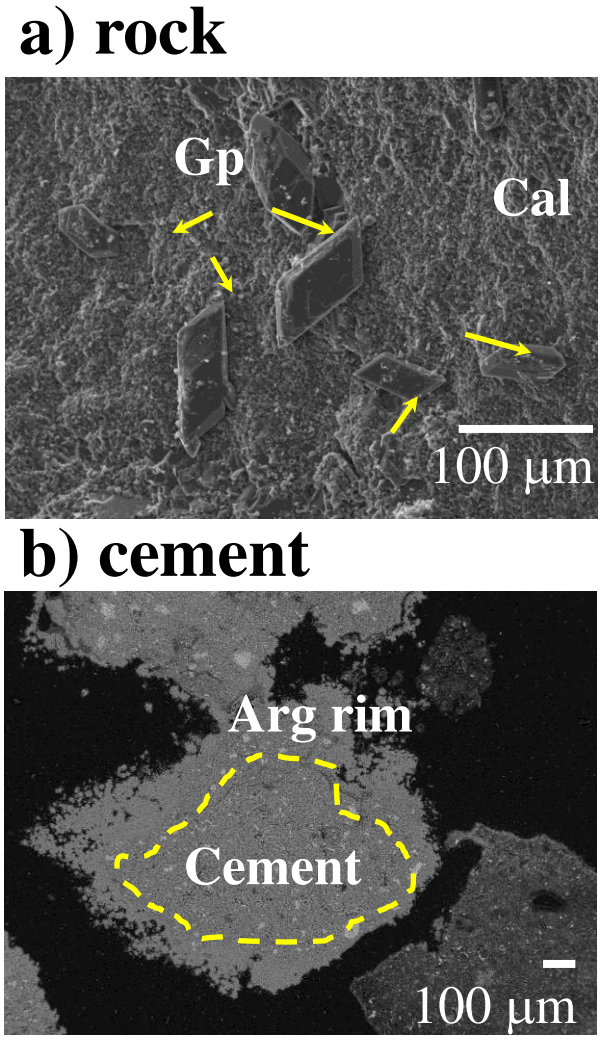

FIG. 8

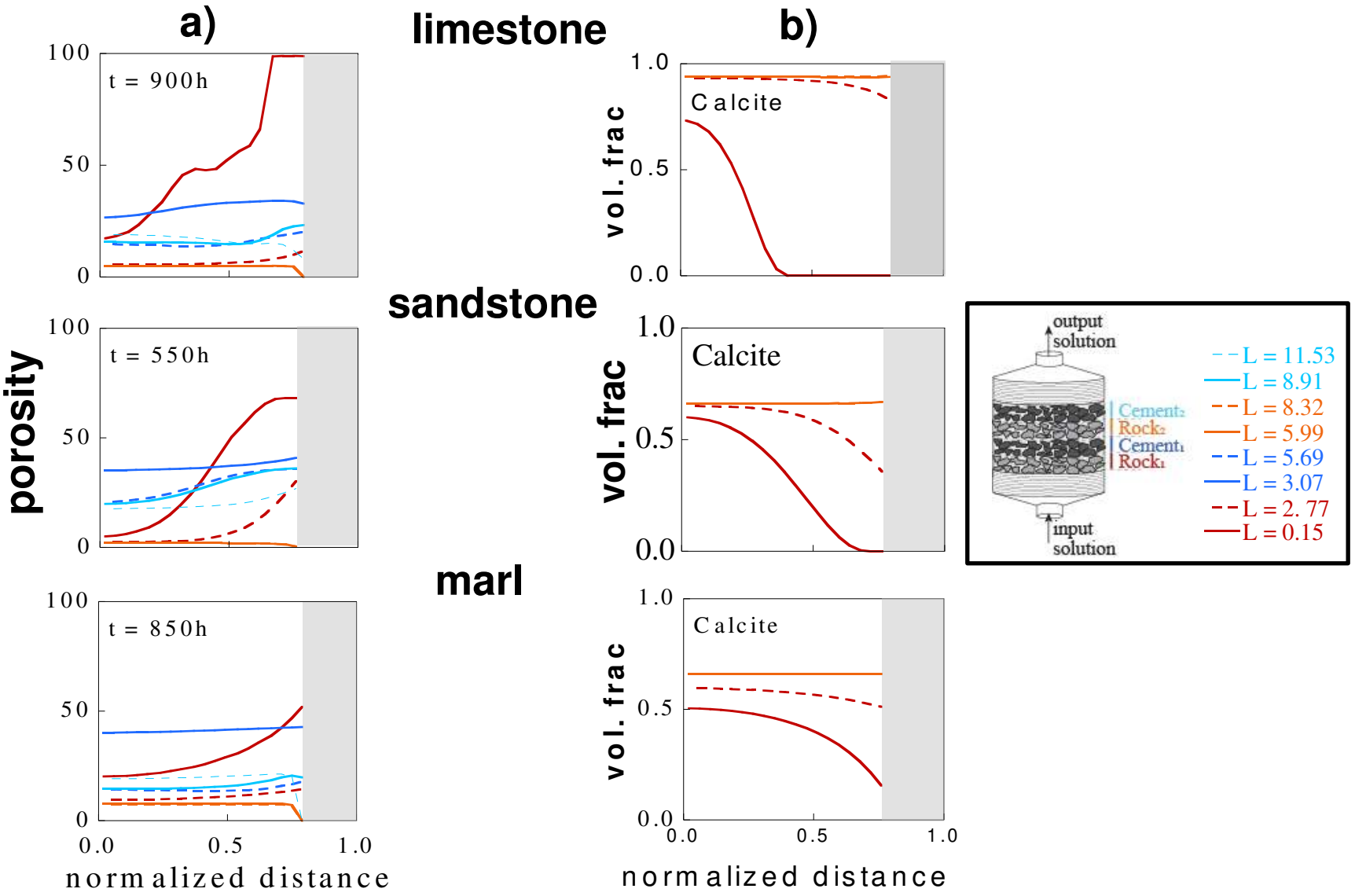
a)
limestone
b)
sandstone
marl
porosity
t = 900h
t = 550h
t = 850h
100
50
0
0.0
0.5
1.0
normalized distance
vol. frac
Calcite
1.0
0.5
0.0
output solution
input solution
Cement2
Rock2
Cement1
Rock1
L = 11.53
L = 8.91
L = 8.32
L = 5.99
L = 5.69
L = 3.07
L = 2. 77
L = 0.15

FIG. 9

limestone

sandstone

a)

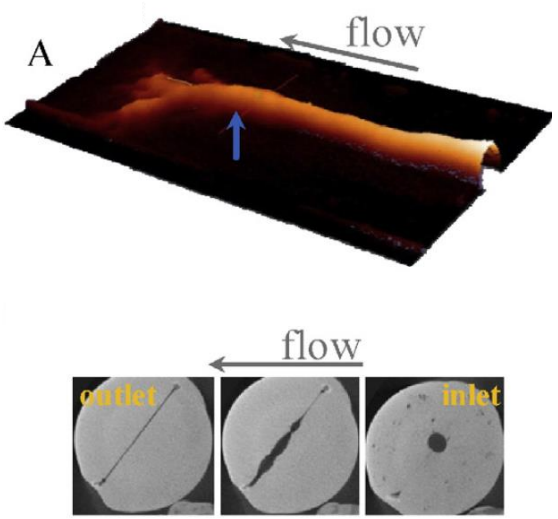

b)

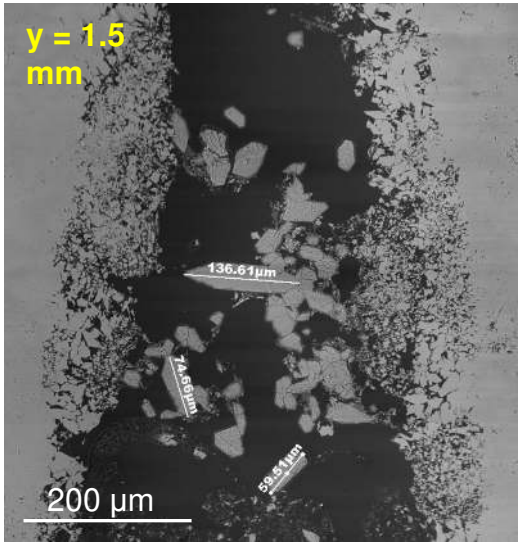

c)

marl

d) S-rich 1 mL h^{-1}

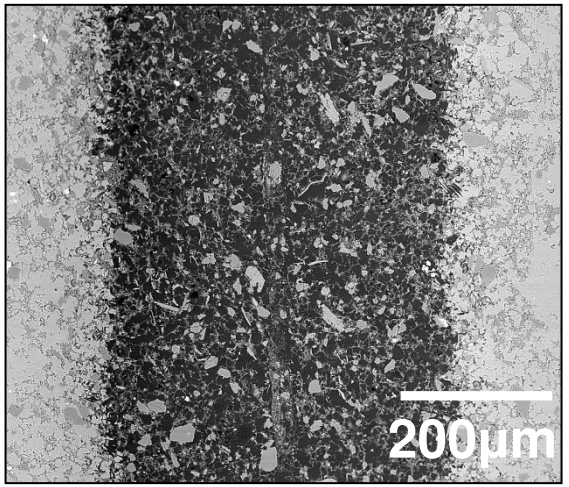

e) S-free 60 mL h^{-1}

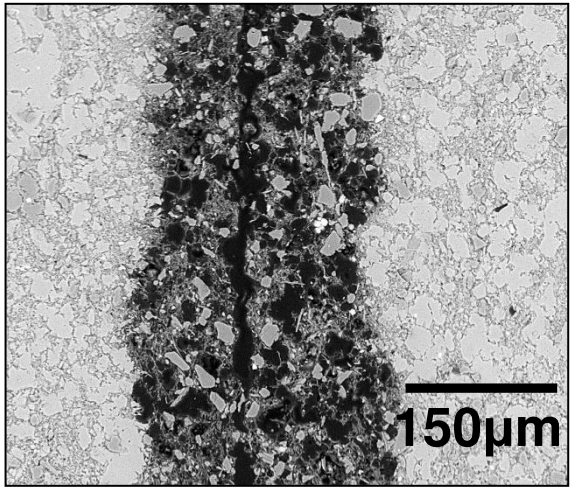

FIG. 10

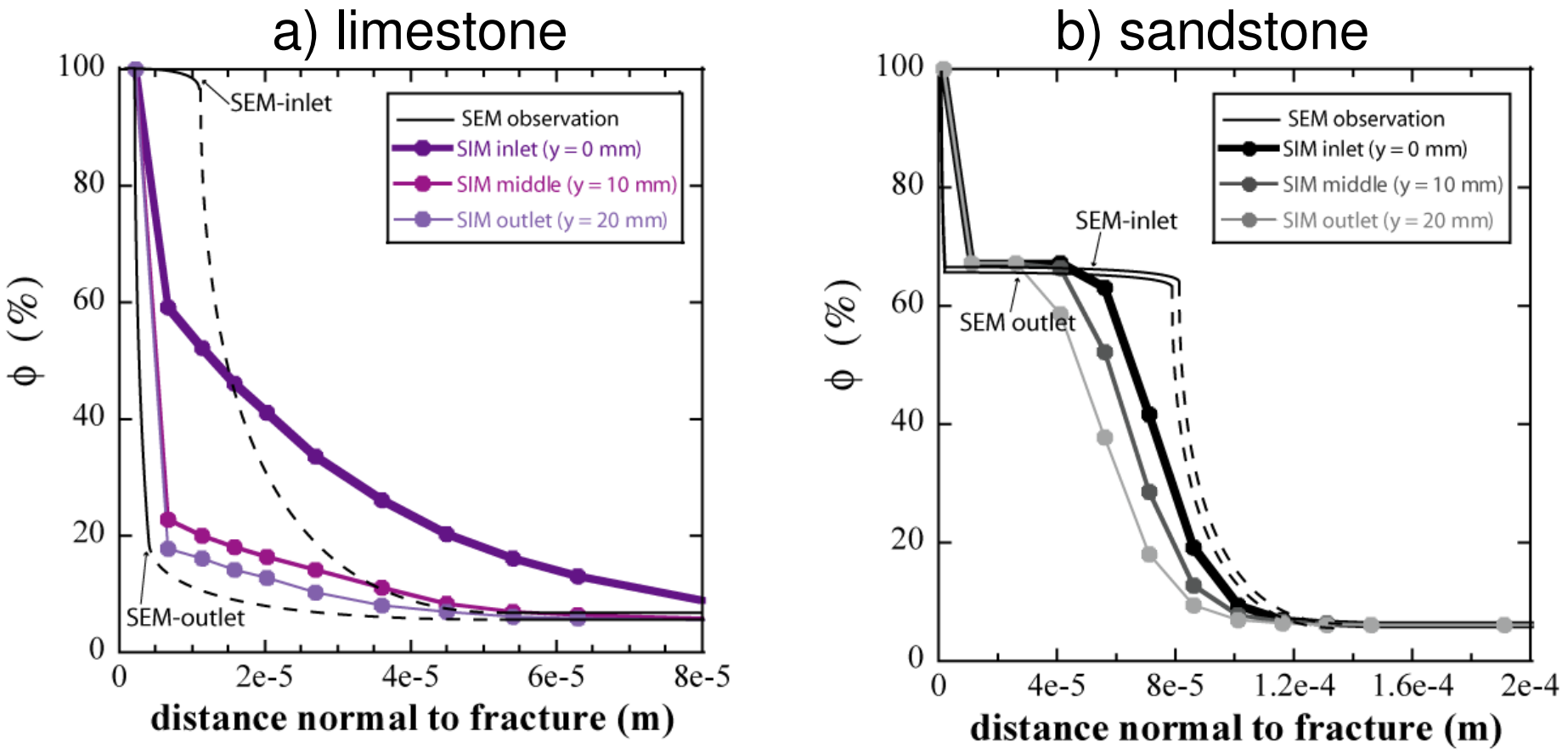
a) limestone
b) sandstone
SEM observation
SIM inlet (y = 0 mm)
SIM middle (y = 10 mm)
SIM outlet (y = 20 mm)
SEM-inlet
SEM-outlet
SEM outlet
ϕ (%)
distance normal to fracture (m)
0
20
40
60
80
100
0
2e-5
4e-5
6e-5
8e-5
4e-5
8e-5
1.2e-4
1.6e-4
2e-4

FIG. 11

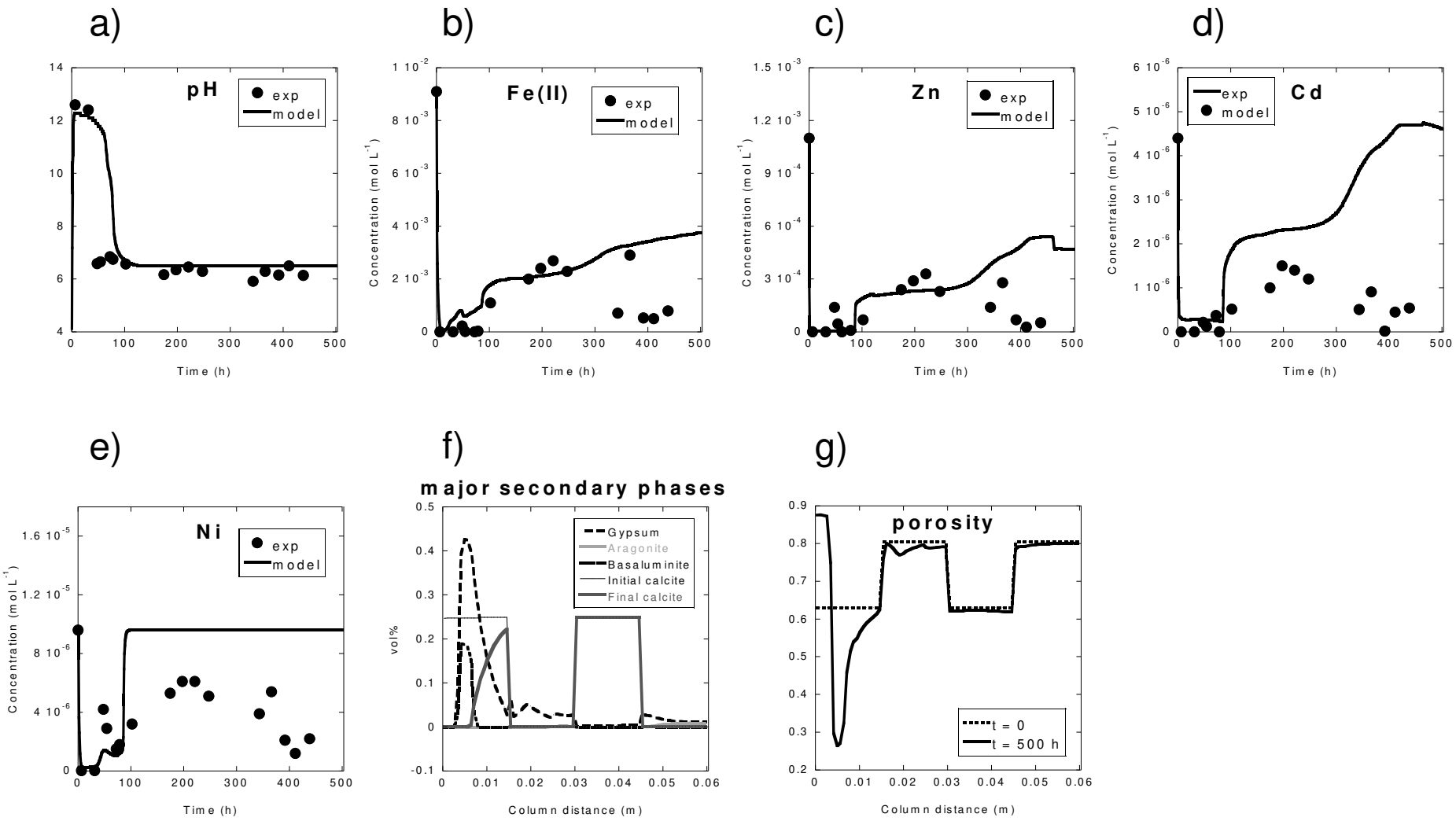
a)
pH
exp
model
Time (h)
b)
Fe(II)
exp
model
Concentration (mol L-1)
Time (h)
c)
Zn
exp
model
Concentration (mol L-1)
Time (h)
d)
Cd
exp
model
Concentration (mol L-1)
Time (h)
e)
Ni
exp
model
Concentration (mol L-1)
Time (h)
f)
major secondary phases
Gypsum
Aragonite
Basaluminite
Initial calcite
Final calcite
vol%
Column distance (m)
g)
porosity
t = 0
t = 500 h
Column distance (m)

FIG. 12

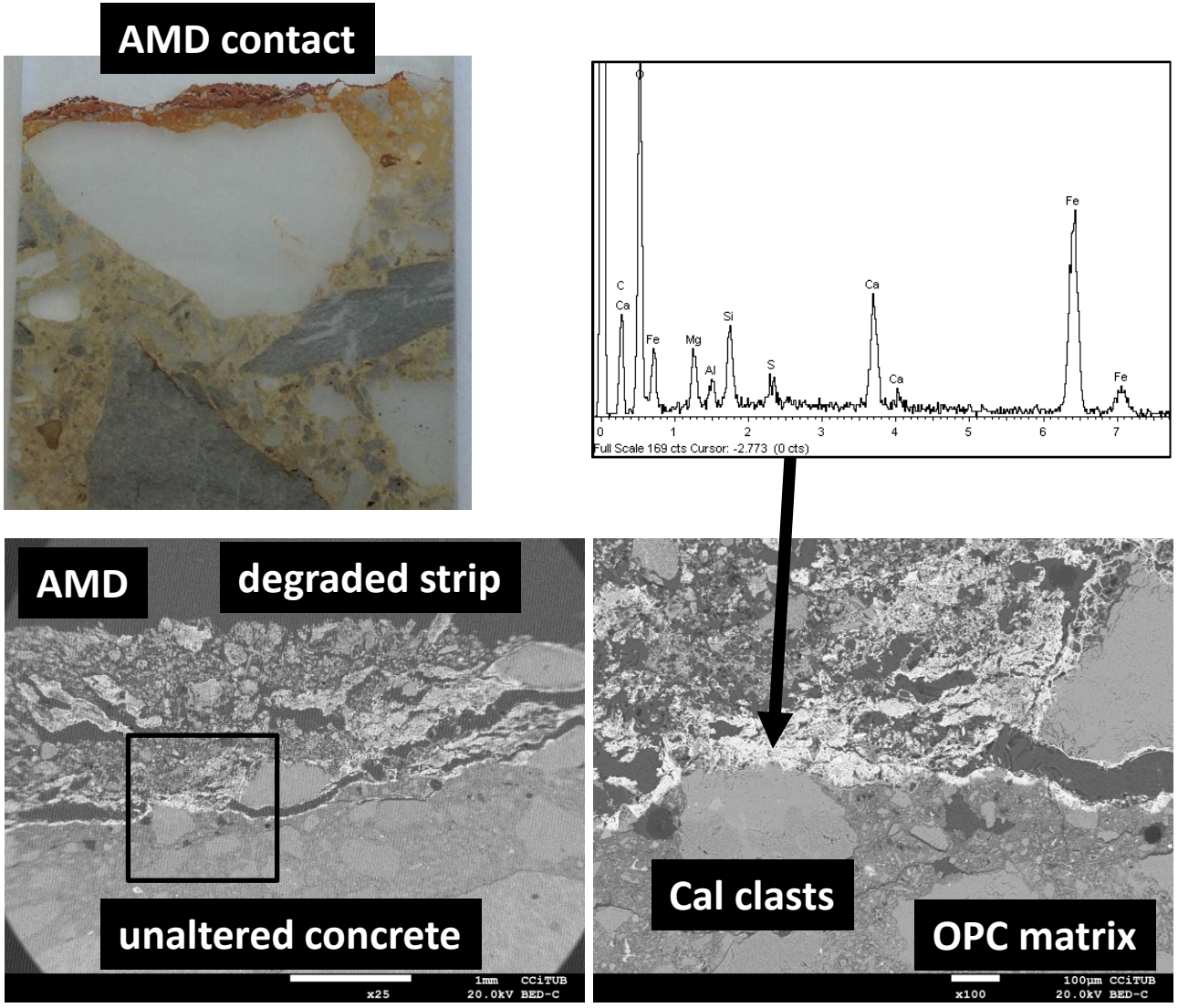
AMD contact
C
Ca
O
Fe
Mg
Al
Si
S
Ca
Ca
Fe
Fe
0
1
2
3
4
5
6
7
Full Scale 169 cts Cursor: -2.773 (0 cts)
AMD
degraded strip
unaltered concrete
1mm CCiTUB
x25 20.0kV BED-C
Cal clasts
OPC matrix
100µm CCiTUB
x100 20.0kV BED-C

FIG. 13

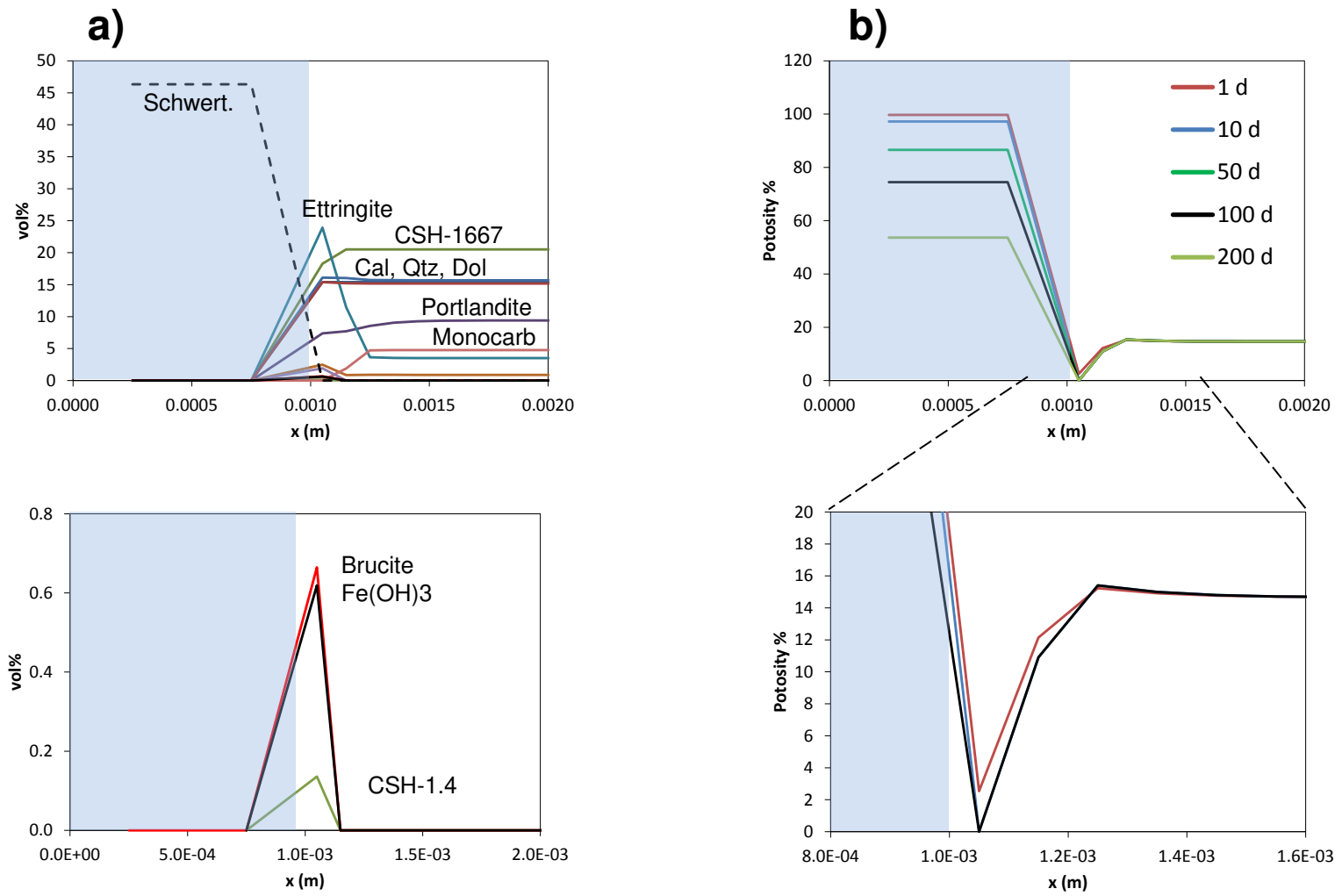
a)
Schwert.
Ettringite
CSH-1667
Cal, Qtz, Dol
Portlandite
Monocarb
vol%
x (m)
Brucite
Fe(OH)3
CSH-1.4
b)
1 d
10 d
50 d
100 d
200 d
Potosity %
x (m)

FIG. 14

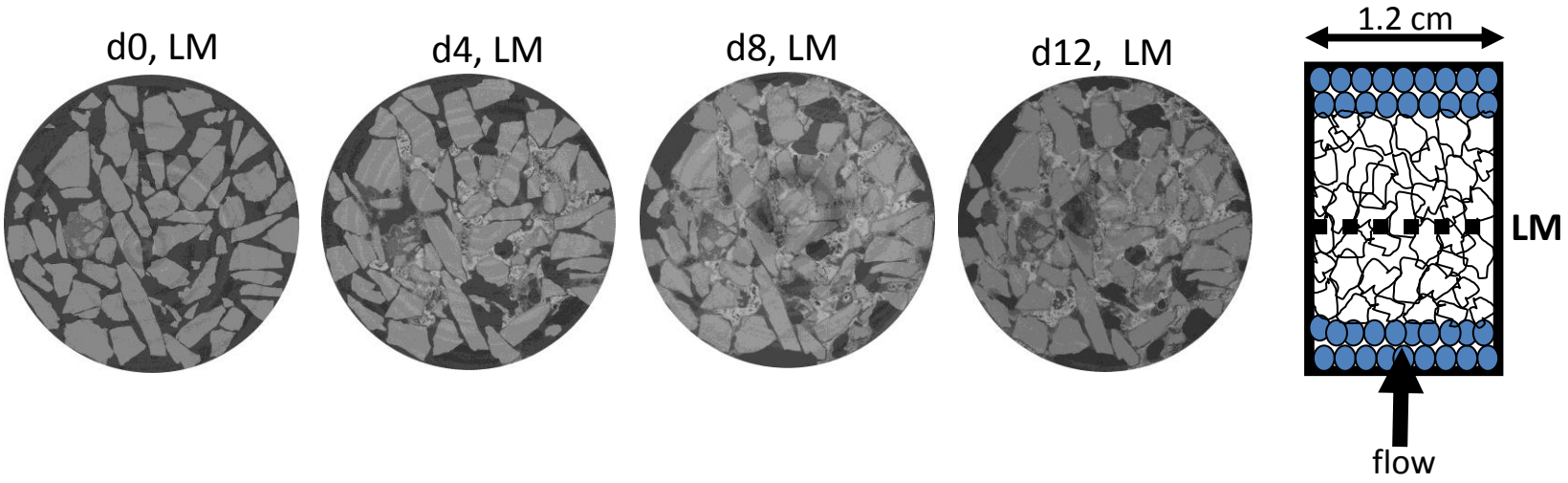

FIG. 15

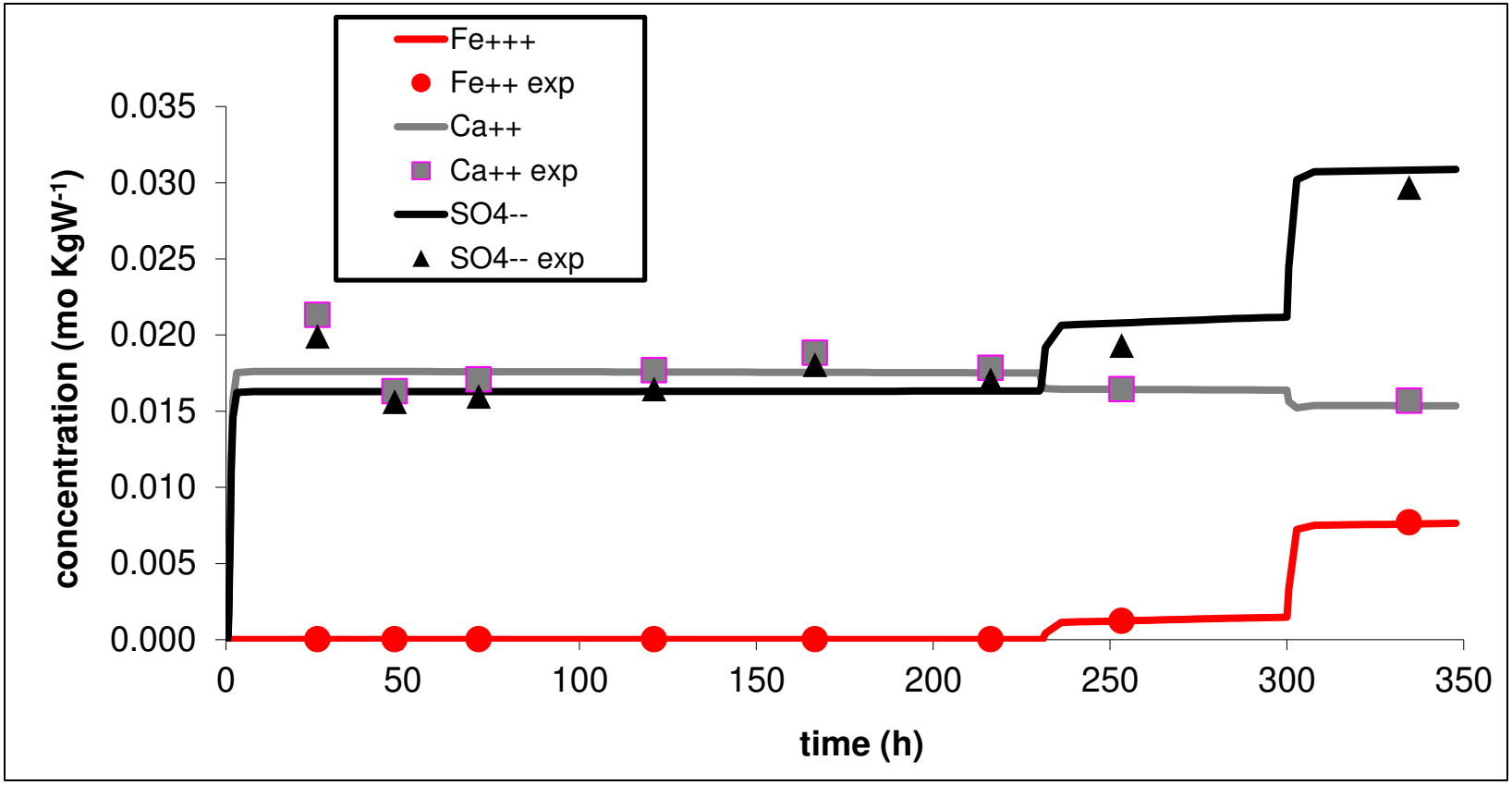
Fe+++
Fe++ exp
Ca++
Ca++ exp
SO4--
SO4-- exp
concentration (mo KgW-1)
0.035
0.030
0.025
0.020
0.015
0.010
0.005
0.000
0
50
100
150
200
250
300
350
time (h)

FIG. 16

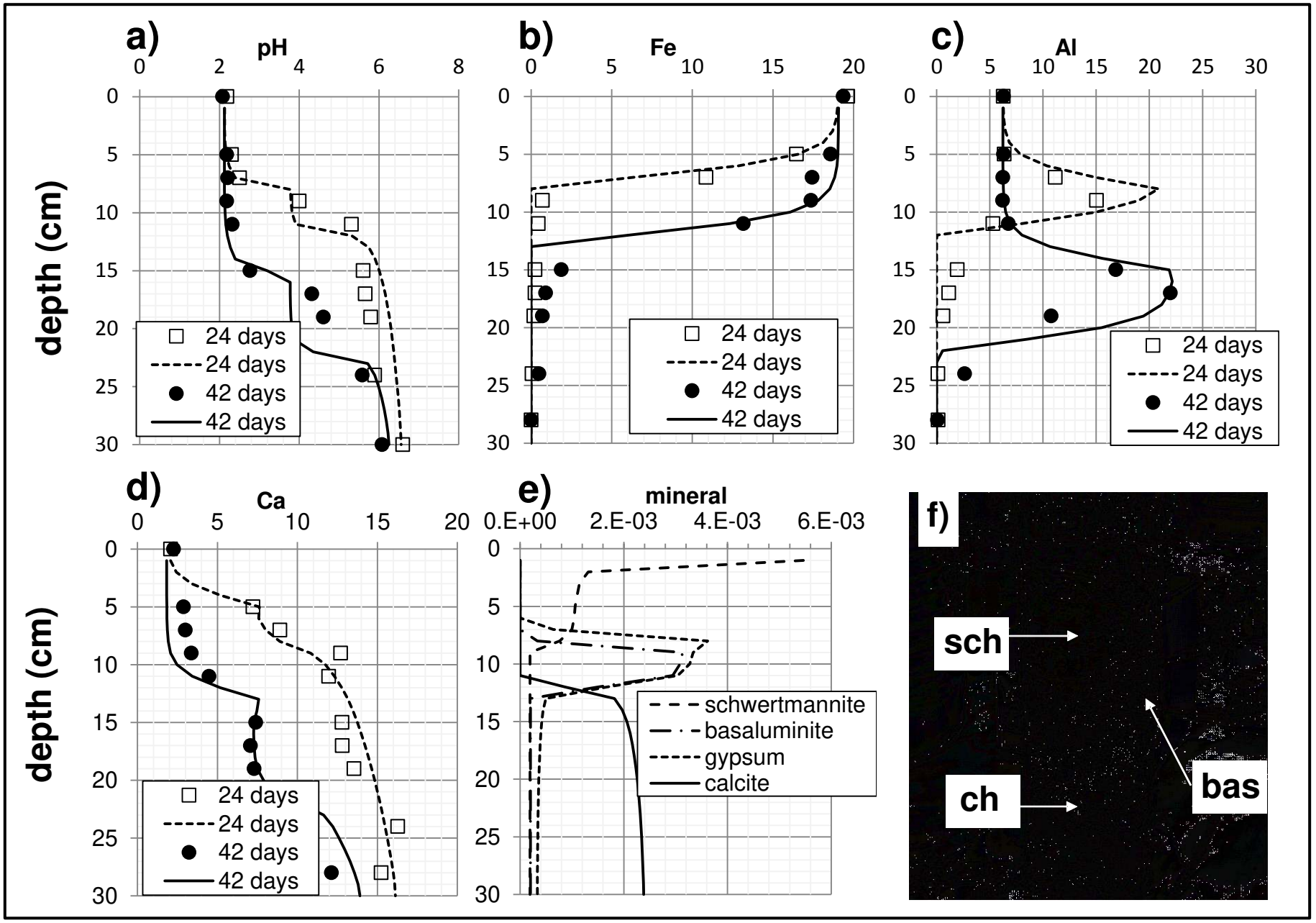
a)
pH
0
2
4
6
8
depth (cm)
0
5
10
15
20
25
30
24 days
24 days
42 days
42 days
b)
Fe
0
5
10
15
20
24 days
24 days
42 days
42 days
c)
Al
0
5
10
15
20
25
30
24 days
24 days
42 days
42 days
d)
Ca
0
5
10
15
20
depth (cm)
24 days
24 days
42 days
42 days
e)
mineral
0.E+00
2.E-03
4.E-03
6.E-03
schwertmannite
basaluminite
gypsum
calcite
f)
sch
ch
bas

FIG. 17

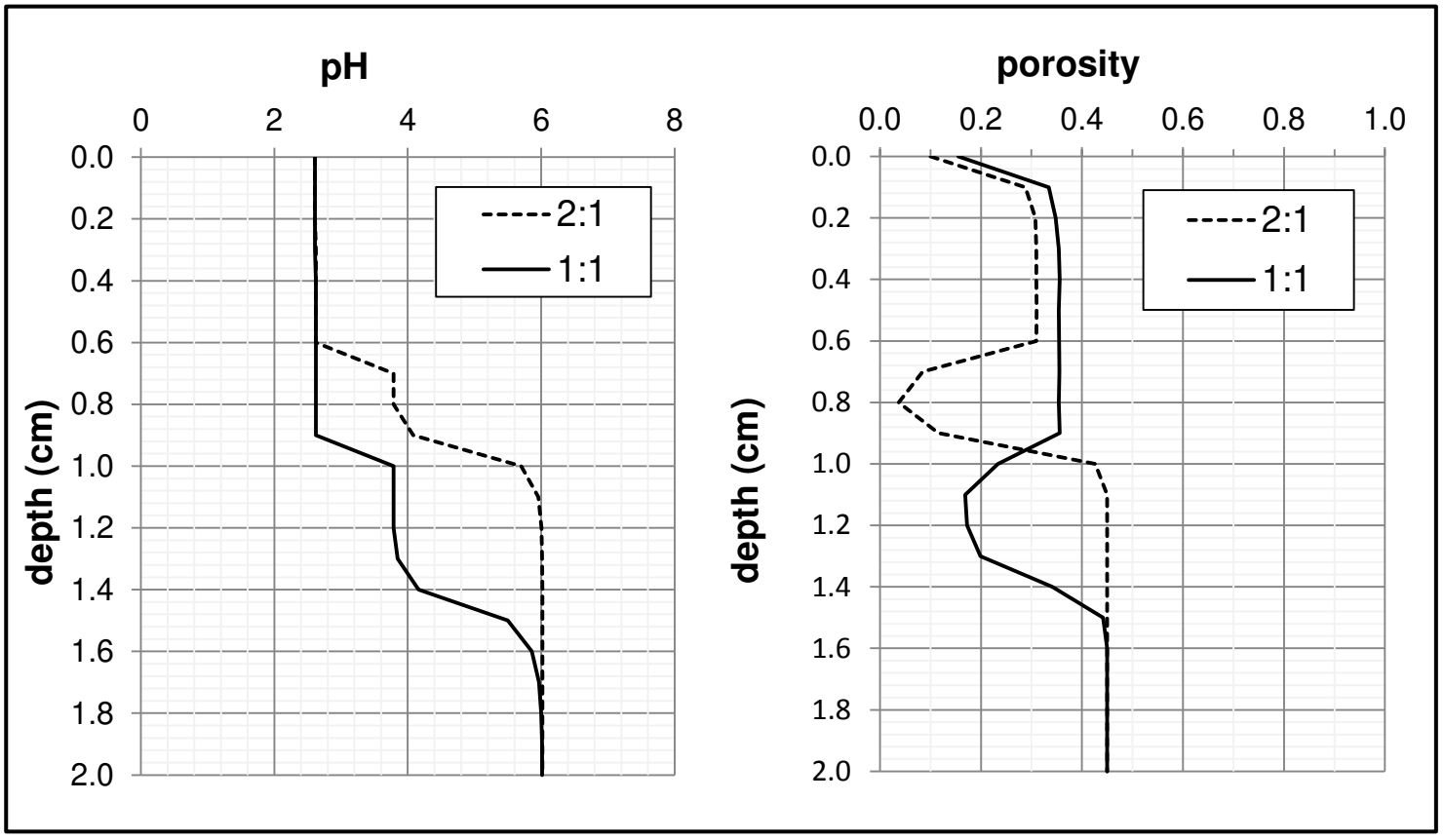
pH
0
2
4
6
8
0.0
0.2
0.4
0.6
0.8
1.0
1.2
1.4
1.6
1.8
2.0
depth (cm)
2:1
1:1
porosity
0.0
0.2
0.4
0.6
0.8
1.0
depth (cm)
2:1
1:1

FIG. 18

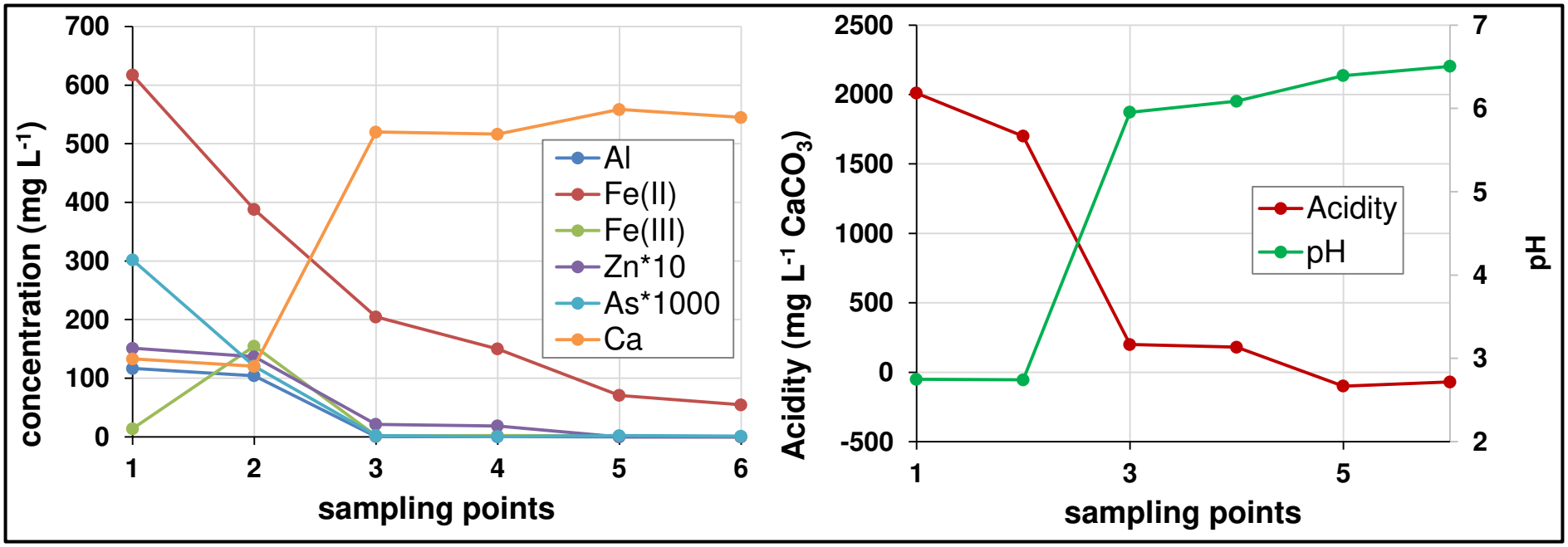
700
600
500
400
300
200
100
0
concentration (mg L-1)
1
2
3
4
5
6
sampling points
Al
Fe(II)
Fe(III)
Zn*10
As*1000
Ca
2500
2000
1500
1000
500
0
-500
Acidity (mg L-1 CaCO3)
7
6
5
4
3
2
pH
1
3
5
sampling points
Acidity
pH

FIG. 19

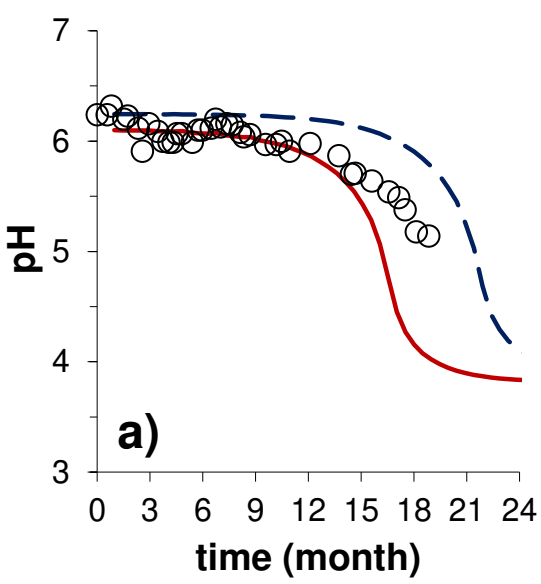
pH
7
6
5
4
3
0 3 6 9 12 15 18 21 24
time (month)
a)

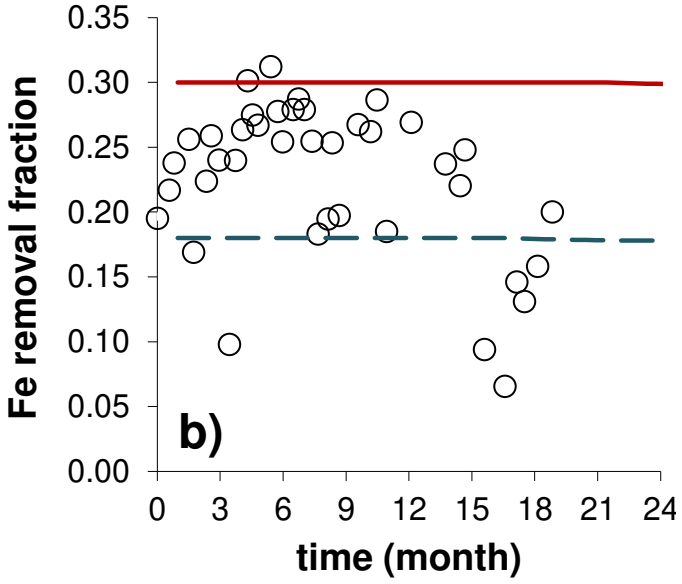
Fe removal fraction
0.35
0.30
0.25
0.20
0.15
0.10
0.05
0.00
0 3 6 9 12 15 18 21 24
time (month)
b)

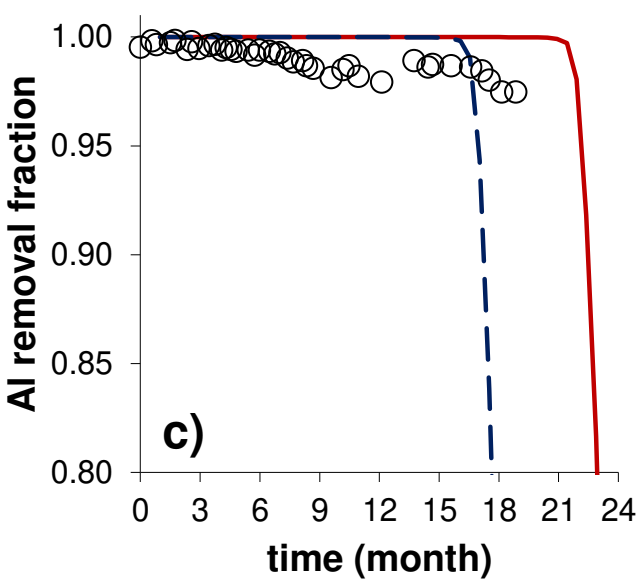
Al removal fraction
1.00
0.95
0.90
0.85
0.80
0 3 6 9 12 15 18 21 24
time (month)
c)

FIG. 20

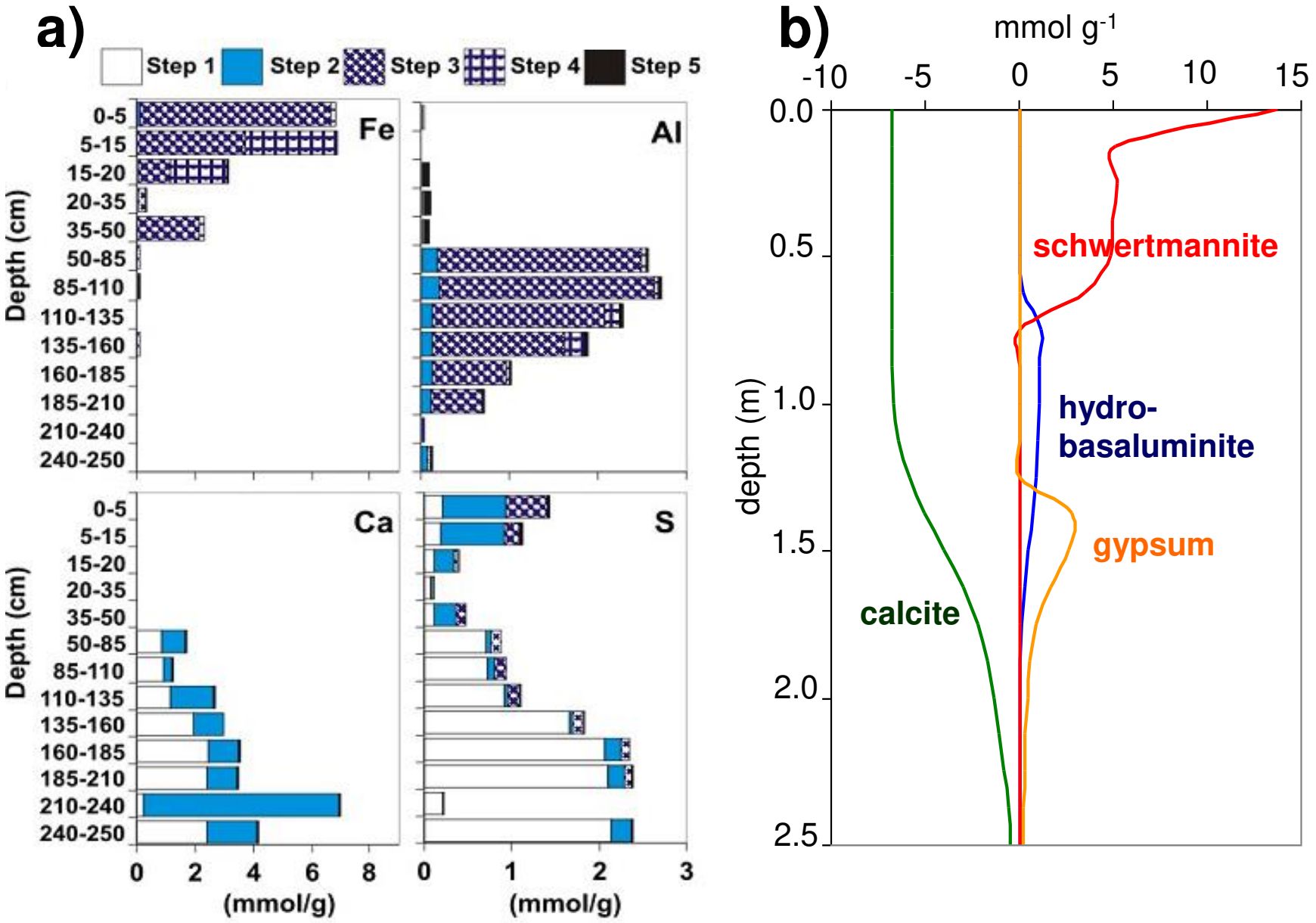
a)
Step 1
Step 2
Step 3
Step 4
Step 5
Fe
Al
Ca
S
Depth (cm)
0-5
5-15
15-20
20-35
35-50
50-85
85-110
110-135
135-160
160-185
185-210
210-240
240-250
0
2
4
6
8
0
1
2
3
(mmol/g)
(mmol/g)
b)
mmol g-1
-10
-5
0
5
10
15
depth (m)
0.0
0.5
1.0
1.5
2.0
2.5
schwertmannite
hydro-
basaluminite
gypsum
calcite

Table 1. Mineral content (wt%).

phase	chemical formula	limestone	dolostone	sandstone	argillaceous marl	hydrated Portland cement
calcite	$CaCO_3$	99		68	71.2-86	4
dolomite			100			
ankerite	$Ca(Fe^{++},Mg)(CO_3)_2$	1		1		
quartz	SiO_2			24	4-9.7	
microcline	$KAlSi_3O_8$			4		
Illite	$K_{0.6}Mg_{0.25}Al_{2.3}Si_{3.5}O_{10}(OH)_2$			2	7.1-15.9	
albite	$NaAlSi_3O_8$				0.9-6.5	
clinochlore	$Mg_3Fe_2Si_3Al_2O_{10}(OH)_8$				0.0-3.1	
pyrite	FeS_2				0.2-2	
gypsum	$CaSO_4 \cdot 2H_2O$				1.0-2.0	
anhydrite	$CaSO_4$				0.0-0.5	
C-S-H						47
portlandite	$Ca(OH)_2$)					25
ettringite	$(Ca_6Al_2(SO_4)_3(OH)_{12} \cdot 26H_2O)$					13
Si-hydrogarnet	$C_3(A,F)S_{0.84}H_{4.32}(Ca_3Al_2Fe_2(SiO_4)_{0.84}(OH)_{8.64})$					8
hydrotalcite	$Mg_6Al_2CO_3(OH)_{16} \cdot 4H_2O$					3

Table 2. Average concentrations and pH of injected solutions.

	CO_2-experiments		*AMD-experiments*	
injected solution	***only CO_2***	***CO_2+H_2SO_4***	***AMD-limestone***	***AMD-layers***
		(mol/kgw)		
Ca^{2+}	4.91E-02	5.40E-02		4.00E-03
SO_4^{2-}	2.68E-02	3.00E-02	1.00E-2-6.00E-2	3.20E-02
Mg^{2+}	3.24E-02	3.30E-02		5.30E-03
K^+	1.13E-02	1.20E-02		
Na^+	3.89E-01	3.93E-01		
Cl^-	4.98E-01	5.10E-01		
Br^-	1.14E-02	1.00E-02		
CO_2	6.16E-01	6.16E-01		
Fe^{2+}			3.50E-3-2.60E-2	9.06E-03
Al^{3+}			3.60E-3-3.60E-2	2.90E-03
Cd^{2+}				4.40E-06
AsO_4^{3-}				1.20E-05
Cu^{2+}				2.70E-04
Zn^{2+}				1.00E-03
Ni^{2+}				1.25E-05
pH	3.3	2.3	2.0 & 3.0	2.0

Table 3. Equilibrium reactions and log K at 25 and 60 °C.

Phases	Reaction	Environment	log K_{eq} (25°C)	log K_{eq} (60°C)	References
Rock					
Calcite	$CaCO_3 + H^+ \leftrightarrow Ca^{2+} + HCO3^-$	GCS, AMD	1.85	1.33	Wolery et al. (1990)
Quartz	$SiO_2 \leftrightarrow SiO_2(aq)$	GCS	-4.00	-3.47	Wolery et al. (1990)
Illite	$K_{0.6}Mg_{0.25}Al_{2.3}Si_{3.5}O_{10}(OH)_2 + 8H^+ \leftrightarrow 0.6K^+ + 0.25Mg^{2+} + 2.3Al^{3+} + 3.5SiO_2(aq) + 5H_2O$	GCS	9.03	5.56	Wolery et al. (1990)
Albite	$NaAlSi_3O_8 + 4H^+ \leftrightarrow Na^+ + Al^{3+} + 3SiO_2(aq) + 2H_2O$	GCS	2.76	1.57	Wolery et al. (1990)
Gypsum	$CaSO_4 \cdot 2H_2O \leftrightarrow Ca^{2+} + SO_4^{2-} + 2H_2O$	GCS, AMD	-4.60	-4.74	Garcia-Rios et al. (2014)
Clinochlore	$Mg_{2.9}Fe_{2.1}Si_3Al_2O_{10}(OH)_8 + 16H^+ \leftrightarrow 2.9Mg^{2+} + 2.1Fe^{2+} + 3SiO_2(aq) + 2Al^{3+} + 12H_2O$	GCS	60.96	50.21	Wolery et al. (1990)
Anhydrite	$CaSO_4 \leftrightarrow Ca^{2+} + SO_4^{2-}$	GCS	-4.31	-4.74	Wolery et al. (1990)
Pyrite	$FeS_2 + H_2O \leftrightarrow Fe^{2+} + 0.25SO_4^{2-} + 1.75HS^-$	GCS, AMD	-24.65	-22.75	Wolery et al. (1990)
Microcline	$KAlSi_3O_8 + 4H^+ \leftrightarrow K^+ + Al^{3+} + 3SiO_2(aq) + 2H_2O$	GCS	-0.28	-0.96	Wolery et al. (1990)
Kaolinite	$Al_2Si_2O_5(OH)_4 + 6H^+ \leftrightarrow 2Al^{3+} + 2SiO_{2(aq)} + 5H_2O$	GCS	6.81	3.85	Wolery et al. (1990)
SiO_2(am)	$SiO_{2(am)} \leftrightarrow SiO_{2(aq)}$	GCS	-2.72	-2.40	Wolery et al. (1990)
Dolomite	$(CaMg)(CO_3)_2 + 2H^+ \leftrightarrow Ca^{2+} + Mg^{2+} + 2HCO_3^-$	GCS	4.06	2.65	Wolery et al. (1990)
Mesolite	$Ca_{0.657}Na_{0.676}Al_{1.99}Si_{3.01}O_{10} \cdot 2.647H_2O + 7.96H^+ \leftrightarrow 0.657Ca^{2+} + 0.676Na^+ + 1.99Al^{3+} + 3.01SiO_{2(aq)} + 6.627H_2O$	GCS	13.62	10.07	Wolery et al. (1990)
Stilbite	$Ca_{1.019}Na_{0.136}K_{0.006}Al_{2.18}Si_{6.82}O_{18} \cdot 7.33H_2O + 8.72H^+ \leftrightarrow 1.019Ca^{2+} + 0.136Na^+ + 0.006K^+ + 2.18Al^{3+} + 6.82SiO_{2(aq)} + 11.69H_2O$	GCS	1.06	-1.01	Wolery et al. (1990)
Scolecite	$CaAl_2Si_3O_{10} \cdot 3H_2O + 8H^+ \leftrightarrow Ca^{2+} + 2Al^{3+} + 3SiO_{2(aq)} + 7H_2O$	GCS	15.88	11.86	Wolery et al. (1990)
Gismondine	$Ca_2Al_4Si_4O_{16} \cdot 9H_2O + 16H^+ \leftrightarrow 2Ca^{2+} + 4Al^{3+} + 4SiO_{2(aq)} + 17H_2O$	GCS	41.72	41.72	Wolery et al. (1990)
Smectite	$Na_{0.33}Mg_{0.33}Al_{1.67}Si_4O_{10}(OH)_2 + 6H^+ \leftrightarrow 0.33Na^+ + 0.33Mg^{2+} + 1.67Al^{3+} + 4SiO_{2(aq)} + 4H_2O$	GCS	2.48	0.43	Wolery et al. (1990)
Boehmite	γ-$AlO(OH) + 3H^+ \leftrightarrow Al^{3+} + 2H_2O$	GCS, AMD	7.56	5.47	Wolery et al. (1990)
Gibbsite	$Al(OH)_3 + 3H^+ \leftrightarrow Al^{3+} + 3H_2O$	GCS, AMD	7.76	5.83	Wolery et al. (1990)
Diaspore	α-$AlO(OH) + 3H^+ \leftrightarrow Al^{3+} + 2H_2O$	GCS, AMD	7.16	5.12	Wolery et al. (1990)
Alunite	$KAl_3(SO_4)_2(OH)_6 + 6H^+ \leftrightarrow K^+ + 2SO_4^{2-} + 3Al^{3+} + 6H_2O$	GCS	-0.35	-4.85	Wolery et al. (1990)
Muscovite	$KAl_2(AlSi_3O_{10})(OH)_2 + 10H^+ \leftrightarrow K^+ + 3Al^{3+} + 3SiO_{2(aq)} + 6H_2O$	GCS	13.59	8.84	Wolery et al. (1990)
Goethite	α-$FeO(OH) + 3H^+ \leftrightarrow Fe^{3+} + 2H_2O$	GCS, AMD	0.53	-0.60	Wolery et al. (1990)
Brucite	$Mg(OH)_2 + 2H^+ \leftrightarrow Mg^{2+} + 2H_2O$	GCS, AMD	16.30	14.27	Wolery et al. (1990)
Aragonite	$CaCO_3 + H^+ \leftrightarrow Ca^{2+} + HCO_3^-$	GCS	1.99	1.48	Wolery et al. (1990)
Cement					
CSH-1667	$1.67Ca(OH)_2 \cdot SiO_2 \cdot H_2O + 3.34H^+ \leftrightarrow 1.67Ca^{2+} + SiO_2(aq) + 4.34H_2O$	GCS, AMD	29.13	26.03	Kulik and Kersten (2001)
CSH-00	$SiO_2 \leftrightarrow SiO_2(aq)$	GCS, AMD	-1.20	-1.07	Kulik and Kersten (2001)
CSH-02	$0.23Ca(OH)_2 \cdot 1.16SiO_2 \cdot 0.23H_2O + 0.46H^+ \leftrightarrow 0.23Ca^{2+} + 1.16SiO_2(aq) + 0.69H_2O$	GCS, AMD	1.96	1.77	Kulik and Kersten (2001)
CSH-04	$0.56Ca(OH)_2 \cdot 1.39SiO_2 \cdot 0.56H_2O + 1.12H^+ \leftrightarrow 0.56Ca^{2+} + 1.39SiO_2(aq) + 1.68H_2O$	GCS, AMD	6.48	5.83	Kulik and Kersten (2001)
CSH-06	$1.03Ca(OH)_2 \cdot 1.72SiO_2 \cdot 1.03H_2O + 2.06H^+ \leftrightarrow 1.03Ca^{2+} + 1.72SiO_2(aq) + 3.09H_2O$	GCS, AMD	13.27	11.96	Kulik and Kersten (2001)

CSH-08	$1.82Ca(OH)_2 \cdot 2.27SiO_2 \cdot 1.82H_2O + 3.64H^+ \leftrightarrow 1.82Ca^{2+} + 2.27SiO_2(aq) + 5.46H_2O$	GCS, AMD	24.63	22.22	Kulik and Kersten (2001)
CSH-10	$Ca(OH)_2 \cdot SiO_2 \cdot 0.86H_2O + 2H^+ \leftrightarrow Ca^{2+} + SiO_2(aq) + 2.86H_2O$	GCS, AMD	14.58	13.09	Kulik and Kersten (2001)
CSH-12	$1.20Ca(OH)_2 \cdot SiO_2 \cdot 0.91H_2O + 2.40H^+ \leftrightarrow 1.20Ca^{2+} + SiO_2(aq) + 3.31H_2O$	GCS, AMD	18.80	16.82	Kulik and Kersten (2001)
CSH-14	$1.40Ca(OH)_2 \cdot SiO_2 \cdot 0.95H_2O + 2.80H^+ \leftrightarrow 1.40Ca^{2+} + SiO_2(aq) + 3.75H_2O$	GCS, AMD	23.12	20.66	Kulik and Kersten (2001)
CASH-005	$1.05CaO \cdot 0.025Al_2O_3 \cdot SiO_2 \cdot 1.2H_2O \leftrightarrow 1.05Ca^{2+} + H_2SiO_4^{2-} + 0.05AlO_2^- + 0.05OH^- + 0.175H_2O$	GCS, AMD	-8.83	-8.82	Myers et al. (2015)
CASH-010	$1.10CaO \cdot 0.05Al_2O_3 \cdot SiO_2 \cdot 1.2H_2O \leftrightarrow 1.10Ca^{2+} + H_2SiO_4^{2-} + 0.1AlO_2^- + 0.1OH^- + 0.15H_2O$	GCS, AMD	-8.68	-8.64	Myers et al. (2015)
CASH-015	$1.15CaO \cdot 0.075Al_2O_3 \cdot SiO_2 \cdot 1.2H_2O \leftrightarrow 1.15Ca^{2+} + H_2SiO_4^{2-} + 0.15AlO_2^- + 0.15OH^- + 0.125H_2O$	GCS, AMD	-8.52	-8.73	Myers et al. (2015)
Portlandite	$Ca(OH)_2 + 2H^+ \leftrightarrow Ca^{2+} + 2H_2O$	GCS, AMD	22.56	20.20	Hummel et al. (2002)
Ettringite	$Ca_6Al_2(SO_4)_3(OH)_{12} \cdot 26H_2O \leftrightarrow 6Ca^{2+} + 2Al(OH)_4^- + 3SO_4^{2-} + 4OH^- + 26H_2O$	GCS, AMD	-44.84	-41.64	Matschei et al. (2007), Lothenbach et al. (2008), Schmidt et al. (2008)
Hydrogarnet	$Ca_3(Al_{0.5}Fe_{0.5})_2(SiO_4)_{0.84}(OH)_{8.64} + 2.52H_2O \leftrightarrow 3Ca^{2+} + Al(OH)_4^- + Fe(OH)_4^- + 0.84\ SiO(OH)_3^- + 3.16OH^-$	GCS, AMD	-29.90	-30.53	Dilnesa et al. (2011, 2012, 2014)
Hydrotalcite	$Mg_4Al_2(OH)_{12} \cdot 3H_2O \leftrightarrow 4Mg^{2+} + 2AlO_2^- + 6OH^- + 5H_2O$	GCS, AMD	-51.14	-50.33	Matschei et al. (2007), Lothenbach et al. (2008), Schmidt et al. (2008)

Table 4. Parameters for the mineral reaction rate laws.

Phases	Acid			Neutral		Basic			m^1	m^2	References
	$k_{m,25}$-rate-H [mol m^{-2} s^{-1}]	Ea-H [kcal mol^{-1}]	a_{H+}^{nH+}-H	$k_{m,25}$-rate-n [mol m^{-2} s^{-1}]	Ea-n [kcal mol^{-1}]	$k_{m,25}$-rate-OH [mol m^{-2} s^{-1}]	Ea-OH [kcal mol^{-1}]	a_{H+}^{nH+}-OH			
Rock											
Calcite	5.01×10^{-1}	3.44	1.000	6.46×10^{5}	5.62	-	-	-	3.0	1.0	Xu et al. (2012), Arvidson et al. (2013)
Quartz	-	-	-	1.02×10^{-14}	20.95	-	-	-	1	1	Palandri and Kharaka (2004), Bandstra et al. (2008)
Illite	2.20×10^{-4}	11.00	0.600	2.50×10^{-13}	13.00	1.26×10^{-57}	15.30	-0.6	1	1	Köhler et al. (2003)
Albite	1.35×10^{-10}	15.52	0.457	9.12×10^{-13}	16.67	1.05×10^{-17}	16.98	-0.572	15	0.3	Palandri and Kharaka (2004)
Gypsum	-	-	-	1.62×10^{-3}	15.00	-	-	-	1	1	Palandri and Kharaka (2004)
Clinochlore	3.21×10^{-10}	16.00	-0.450	-	-	-	-	-	1.5	0.06	Hamer et al. (2003), Zhang et al. (2015)
Anhydrite	-	-	-	6.45×10^{-4}	3.42	-	-	-	1	1	Palandri and Kharaka (2004)
Pyrite*	3.02×10^{-8}	13.61	-0.500	2.82×10^{-5}	13.61	-	-	-	1	1	Palandri and Kharaka (2004), Domènech et al. (2002)
Microcline	8.70×10^{-11}	12.40	0.500	3.89×10^{-13}	9.08	-	-	-	14	0.4	Bandstra et al. (2008)
Kaolinite	4.90×10^{-12}	15.76	0.777	6.61×10^{-14}	5.31	8.91×10^{-18}	4.28	-0.472	1	1	Palandri and Kharaka (2004)
SiO_2(am)	-	-	-	1.00×10^{-9}	0.00	-	-	-	1	1	**
Dolomite	6.45×10^{-4}	8.63	0.500	2.95×10^{-8}	12.48	-	-	-	1	1	Palandri and Kharaka (2004)
Mesolite	-	-	-	1.00×10^{-9}	0	-	-	-	1	1	**
Stilbite	-	-	-	1.00×10^{-9}	0	-	-	-	1	1	**
Scolecite	-	-	-	1.00×10^{-9}	0	-	-	-	1	1	**
Gismondine	-	-	-	1.00×10^{-9}	0	-	-	-	1	1	**
Smectite	-	-	-	1.00×10^{-12}	0	-	-	-	1	1	**Cama et al. (2000)
Boehmite	2.24×10^{-8}	11.35	0.992	4.68×10^{-14}	11.35	2.51×10^{-24}	11.35	-1.503	1	1	k_{acid} same as gibbsite; $k_{neutral}$ and k_{basic} same as diaspore; Palandri and Kharaka (2004)
Gibbsite	2.24×10^{-8}	11.35	0.992	4.68×10^{-14}	11.35	2.51×10^{-24}	11.35	-1.503	1	1	$k_{neutral}$ and k_{basic} same as diaspore; Palandri and Kharaka (2004)
Diaspore	2.24×10^{-8}	11.35	0.992	4.68×10^{-14}	11.35	2.51×10^{-24}	11.35	-1.503	1	1	k_{acid} same as gibbsite; Palandri and Kharaka (2004)
Alunite	-	-	-	3.98×10^{-5}	7.65	-	-	-	1	1	Acero et al. (2015)
Muscovite	1.41×10^{-12}	5.26	0.370	2.82×10^{-14}	5.26	2.82×10^{-15}	5.26	-0.22	1	1	Palandri and Kharaka (2004)
Goethite	-	-	-	1.00×10^{-10}	0.00	-	-	-	1	1	**

Brucite	1.86×10^{-5}	14.10	0.500	5.75×10^{-9}	10.04	-	-	-	1	1	Palandri and Kharaka (2004)
Aragonite	-	-	-	7.94×10^{-9}	0.00	-	-	-	1	1	Cubillas et al. (2005)
Cement											
CSH-1667	-	-	-	5.01×10^{-11}	0	-	-	-	1	1	**Trapote-Barreira et al. (2014)
CSH-00	-	-	-	5.01×10^{-11}	0	-	-	-	1	1	**Trapote-Barreira et al. (2014)
CSH-02	-	-	-	5.01×10^{-11}	0	-	-	-	1	1	**Trapote-Barreira et al. (2014)
CSH-04	-	-	-	5.01×10^{-11}	0	-	-	-	1	1	**Trapote-Barreira et al. (2014)
CSH-06	-	-	-	5.01×10^{-11}	0	-	-	-	1	1	**Trapote-Barreira et al. (2014)
CSH-08	-	-	-	5.01×10^{-11}	0	-	-	-	1	1	**Trapote-Barreira et al. (2014)
CSH-10	-	-	-	5.01×10^{-11}	0	-	-	-	1	1	**Trapote-Barreira et al. (2014)
CSH-12	-	-	-	5.01×10^{-11}	0	-	-	-	1	1	**Trapote-Barreira et al. (2014)
CSH-14	-	-	-	5.01×10^{-11}	0	-	-	-	1	1	**Trapote-Barreira et al. (2014)
CASH-005	-	-	-	1.00×10^{-5}	0	-	-	-	1	1	**
CASH-010	-	-	-	1.00×10^{-5}	0	-	-	-	1	1	**
CASH-015	-	-	-	1.00×10^{-5}	0	-	-	-	1	1	**
Portlandite	-	-	-	3.98×10^{-6}	0	-	-	-	1	1	Bullard et al. (2010)
Ettringite	-	-	-	1.00×10^{-6}	0	-	-	-	1	1	**
Hydrogarnet	-	-	-	1.00×10^{-6}	0	-	-	-	1	1	**
Hydrotalcite	-	-	-	1.00×10^{-6}	0	-	-	-	1	1	**

*pyrite rate law depends on oxygen concetration (n_{O2}= 0.5)

**Large value of $A \cdot k_m$ to allow local equilibrium conditions

Table 5. Values of mineral reactive surface areas used in the simulations.

mineral	$A_{mineral}$ $m^2_{mineral}\ m^{-3}_{bulk\ rock}$	rock	P conditions	injected solution	reference
dissolution					
calcite					
	130 ± 50	L	atm, SubC & SupC	CO_2	1, 3
	250 → 32	L	SubC	CO_2+H_2SO_4	3
	3-30	M	atm	CO_2	2
	130 ± 50	M	SubC & SupC	CO_2	2
	200-500	M	SubC	CO_2	3
	90-500	M	SubC	CO_2+H_2SO_4	3
	250-5000	S	SubC	CO_2	3
	15 → 7	S	SubC	CO_2+H_2SO_4	3
	600	L	SupC	CO_2	4
	300000	S	SupC	CO_2	4
	20000-250000	M	SupC	CO_2	5
	20 → 0.1	L	atm	AMD	6
	180	L	atm	AMD	7
dolomite	5-10	D	atm, SubC & SupC	CO_2	1, 3
quartz	1-36	M, S	atm, SubC & SupC	CO_2, CO_2+H_2SO_4	2, 3
	3605	S	SupC	CO_2	4
	1000000	M	SupC	CO_2	5
aluminosilicates	40 - $2x10^8$	M	atm, SubC & SupC	CO_2	2
illite	8000	M	SubC	CO_2, CO_2+H_2SO_4	3
clinochlore	500-9000	M	SubC	CO_2, CO_2+H_2SO_4	3
	$3.9x10^9$	M	SupC	CO_2	5
albite (99.6 %)	41	M	SubC	CO_2+H_2SO_4	3
albite (0.4 %)	5 - $55x10^6$	M	SubC	CO_2+H_2SO_4	3
	$3.5x10^8$	M	SupC	CO_2	5
microcline (99.85 %)	40000	S	SubC	CO_2+H_2SO_4	3
microcline (» 0.1 %)	2-$7x10^6$	S	SubC	CO_2+H_2SO_4	3
	2180	S	SupC	CO_2	4
pyrite	5	M	atm, SubC & SupC	CO_2	2
precipitation					
gypsum	0.01 - 10	L	atm, SubC & SupC	CO_2	1
	0.3	D	atm, SubC & SupC	CO_2	1
	90	M	atm	CO_2	2
	0.02 - 0.09	M	SubC & SupC	CO_2	2
	0-0.01 → 0.3-500	M	SubC	CO_2+H_2SO_4	3
	0-0.005 → 0.04-5000	S	SubC	CO_2+H_2SO_4	3
	100	L	SupC	CO_2	4
	10	M	SupC	CO_2	5
	10	L	atm	AMD	6
secondary phases-M	10000	M	atm, SubC & SupC	CO_2	2, 3,5
secondary phases-S	100000	S	SubC	CO_2, CO_2+H_2SO_4	3
goethite	100000	M, S	SubC	CO_2+H_2SO_4	3
	0.1	L	atm	AMD	

L = limestone; M = marl; S = sandstone

atm = atmospheric pressure; SubC = P_{TOT} = pCO_2 = 10 bar; SupC = P_{TOT} = 150 bar & pCO_2 = 34-37 bar

$A_{geometric}$ = 900 to 8000 $m^2_{min}\ m^{-3}_{bulk}$; fragment diameter: 0.25-5 mm; ref. (1-3)

$A_{geometric}$ = 1000000 $m^2_{min}\ m^{-3}_{bulk}$ in limestone; $A_{geometric}$ = 750000 $m^2_{min}\ m^{-3}_{bulk}$ in sandstone; fragment diameter: 2.5 μm; ref. (4)

$A_{geometric}$ = 200000 $m^2_{min}\ m^{-3}_{bulk}$; fragment diameter: 10 μm; ref. (5)

$A_{geometric}$ = 2000 $m^2_{min}\ m^{-3}_{bulk}$; A_{BET} = 600000 $m^2_{min}\ m^{-3}_{bulk}$; fragment diameter:1-2 mm; ref. (6)

$A_{geometric}$ = 4000 $m^2_{min}\ m^{-3}_{bulk}$; fragment diameter: 1-2 mm; ref. (7)

1: García-Rios et al. (2014); 2: Dávila et al. (2017); 3: Thaysen et al. (2017)

4: García-Rios et al. (2017); 5: Dávila et al. (2016); 6: Offeddu et al. (2016); 7: Ayora et al. (2013)

aluminosilicates (marl): illite, albite, clinochlore

secondary phases-M (marl): kaolinite, mesolite, stilbite, scolecite, boehmite, gibbsite, diaspore and alunite

secondary phases-S (sandstone): boehmite, gibbsite, diaspore and alunite

CO_2+H_2SO_4 = CO_2 with H_2SO_4 addition